Inducing spin dynamics in antiferromagnetic NiO

Kools, T.J.

Award date:
2020

EINDHOVEN UNIVERSITY OF TECHNOLOGY

Department of Applied Physics
Physics of Nanostructures Research Group

Inducing spin dynamics in antiferromagnetic NiO

Master Thesis

Thomas J. Kools

Supervisors:
Ir. Casper F. Schippers (Daily Supervisor)
Ir. Tom Lichtenberg (Daily Supervisor)
Prof. dr. Bert Koopmans (Responsible Lecturer)

Eindhoven, February 2020

Abstract

Antiferromagnets (AFMs) have for the past 60 years played a passive role in spintronic applications for their ability to "pin" the orientation of an adjacent ferromagnet (FM). Fascinating intrinsic properties of AFMs such as spin dynamics at the THz timescale and insensitivity to perturbation by external magnetic fields have driven the research field of antiferromagnetic spintronics in recent years, pushing for the use of active AFM elements in applications like faster and denser magnetic memory, and THz radiation emitters. Furthermore, antiferromagnetic insulators (AFMIs) have potential for energy efficient magnonic spin transport; contrary to spin currents carried by itinerant electrons where Joule heating causes significant losses.

In this thesis, sputter deposited ultrathin films of the AFMI NiO implemented in magnetic multilayer stacks are investigated. The purpose was to facilitate two optical experiments: investigation of the dynamic response of thin films of NiO to optical spin currents caused by demagnetization of a nearby FM layer, as well as testing the use of NiO films as a spin current transmitter. Said goals were approached from both a numerical point of view, and an experimental point of view. These experiments pave the way for combining the favourable properties of AFMs with the flexibility and tunability of magnetic thin films.

By combining a diffusive spin transport model and a description of the spin dynamics of the AFM NiO, the response of the AFM to a short (ps) spin current pulse was studied. It was found that for realistic material parameters, the induced magnetization from the spin current pulse is about 1% of the antiparallel sublattice magnetization, which corresponds to a Faraday rotation of 1-0.1 µrad. This value depends (among other things) on interface quality and the damping in the AFM, however the found value suggests that this transient magnetization can be measured using optical techniques.

Two stacks combining ultrathin films of AFM(I)s, FMs and non-magnetic metals (NMs) have been designed and characterized for the optical spin current experiments: an FM/NM/AFMI stack was used to investigate the presence of a transient spin-current-induced magnetization in NiO. In the other experiment an FM/AFMI/FM multilayer was intended to perform the magnonic spin transport experiments. Several experimental techniques have been employed to characterize these complex stacks, confirming the required magnetic and structural properties of the deposited films.

Pump-probe experiments were used to investigate the response of the two stacks to laser-induced ultrafast demagnetization of the FM layer. No transient magnetization was detected at the NiO, even though demagnetization of the FM was measured. It is hypothesised that the estimation of the spin current induced magnetization from the (ideal) model is too optimistic and that e.g. pinning at domain walls in the AFM leads to additional attenuation of the induced magnetization, potentially bringing the associated signal below the noise floor of our setup. Finally, transmission measurements were performed on stacks where the required anisotropy did not manifest in the FM multilayer and which should thus not show any temporal response related to demagnetization. A clear transient signal of non-magnetic origin was still observed, which was hypothesised to be a transient reflectance effect.

Despite the fact that plenty of challenges remain with regards to improvement of the model, the stack growth, and understanding of the optical experiments; this thesis still provides a firm jumping board towards the implementation of sputtered films of NiO (and potentially other AFMIs) in magnetic multilayer stacks by providing a model description, and by acquiring important information regarding characterization and growth of these materials.

List of Abbreviations

AFM	Antiferromagnet
AFMI	Antiferromagnetic Insulator
CWP	Clockwise Polarization
CCWP	Counterclockwise polarisation
DOS	Density Of States
FM	Ferromagnet
GK	Goodenough-Kanamori
IP	In Plane
ISHE	Inverse Spin Hall Effect
LEED	Low-Energy Electron Diffraction
MOKE	Magneto-Optical Kerr effect
NM	Non-magnetic Metal
OOP	Out Of Plane
RT	Room Temperature
SQUID	Superconducting Quantum Interference Device
TRFE	Time-Resolved Faraday Effect
UHV	Ultra High Vacuum
VSM	Vibrating Sample Magnetometry
XPS	X-ray Photoelectron Spectroscopy
XRD	X-ray Diffraction
YIG	Yttrium Iron Garnet

Contents

Chapter 1

Introduction

Back in 1970, French physicist Louis Néel was co-awarded the Nobel prize in physics by the Royal Swedish Academy of Science [1]. In his Nobel lecture, the laureate posed the oft-quoted remark: "They [antiferromagnets] are extremely interesting from the theoretical viewpoint, but do not seem to have any applications [2]." Back in the day, this statement would raise few eyebrows. Most of the experimental work on these type of magnetic materials was comprised of characterization studies [3–9] and focused little on the potential applications. With the advent of magnetic memory storage, this status of "interesting, but useless" started to change; to this date antiferromagnetic materials play a pivotal, but essentially passive role in these sort of devices, where the state of ferromagnetic materials is used to record information [10].

1.1 Why bother with antiferromagnets?

However in the re-emergence of the research field of antiferromagnetic spintronics over the last 5-10 years [12–15], distinct efforts have been made to use antiferromagnets (AFMs) – materials where the magnetic moments in the material are aligned in antiparallel fashion and therefore show neither stray fields nor a net magnetization – as active elements in devices. Therefore, the first question should be why AFMs are subject to intensive research in the first place. It is convenient to introduce the favourable properties of AFMs based on a real application prospect: antiferromagnetic data storage.

Similar to ferromagnets (FMs), AFMs can also be used to encode information. Figure 1.1a and 1.1b show the way magnetic bits can be used to encode information for FMs and AFMs respectively. As shown in figure 1.1a, the logical "1" and "0" in FMs are defined by the magnetization direction denoted by the single arrow. This same magnetization however also poses a challenge to FM memory devices in the form of their stray fields, as shown by the dotted lines in the same figure. When the bit size and spacing become too small, inter-bit interference due to these stray fields will lead to a decrease in stability of the memory, putting an inherent limit on the bit packing density.

This immediately shows one advantage of AFM-based memory like the one presented in figure 1.1b. Due to their antiparallel magnetic ordering and associated lack of stray fields, inter-bit interference does not limit the packing density and hence denser memories can potentially be created. Also, the lack of a net magnetization implies an insensitivity to perturbation by external magnetic fields, adding to the stability of the stored information. Finally, the antiferromagnetic coupling between the spins in AFMs leads to spin dynamics in the THz

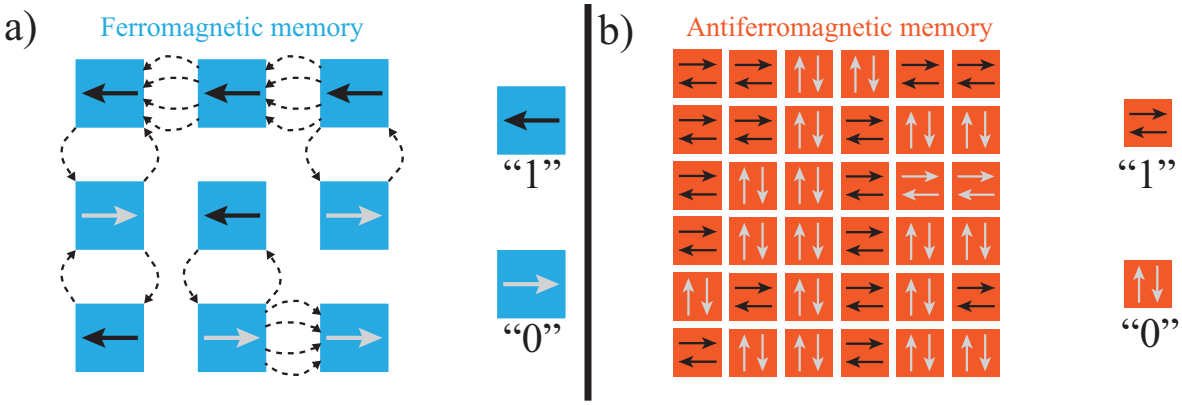

Figure 1.1: Schematic representation of a): ferromagnetic memory, where some of the field lines of the magnetic bits are shown to illustrate inter-bit cross-talking. b): antiferromagnetic memory, where the lack of stray fields allows closer packing while still maintaining stable memory storage. Image based on figure 1 from [11].

regime, compared to anisotropy driven GHz dynamics observed in FMs [16–18]. This also leads to potentially faster switching of the magnetic state [19, 20].

These appealing intrinsic properties of AFMs are an important part of the motivation for contemporary research into this class of materials. Another important argument for investigating AFMs here is the flexibility in material choice, as antiferromagnetism is a much more common type of magnetic ordering than ferromagnetism [14].

Although this all sounds highly interesting – near insensitivity to applied fields, THz-frequency dynamics, no bit cross-talking, – the same antiparallel alignment in AFMs is also the reason that the applicability of AFMs in technology has been limited thus far. The insensitivity to external fields makes control of the magnetic state in these materials difficult. Furthermore, typical detection methods used within the field of spintronics to characterize the magnetic state of an FM, such as the magneto-optical Kerr effect (MOKE), rely (naively put) on parallel alignment of spins in the material. Other, more elaborate methods are therefore required (e.g. Second harmonic generation [21], X-ray magnetic linear dichroism [22]), which slow down integration of active antiferromagnetic elements in applications; hence visualization of antiferromagnetic order is a lively field of research in order to overcome this challenge [12, 15].

1.2 Magnonic spin currents

Despite the fact that many challenges still remain, serious progress has also already been made. One of these areas of progress relates to the spin transport in these materials. Typically, spin currents are carried by spin polarized electrons. If spin currents can be transferred without the need for an electrical current however, this can significantly reduce loss from Joule heating associated with electrons moving through a material. Collective excitations of the antiferromagnetic spins in antiferromagnetic insulators (AFMIs), known as spin waves or magnons, can do exactly that. Spin information can be transported with these spin waves without the need for moving electrons; furthermore, when good control over these spin waves can be achieved, logic operations can be performed by making use of the wave character of

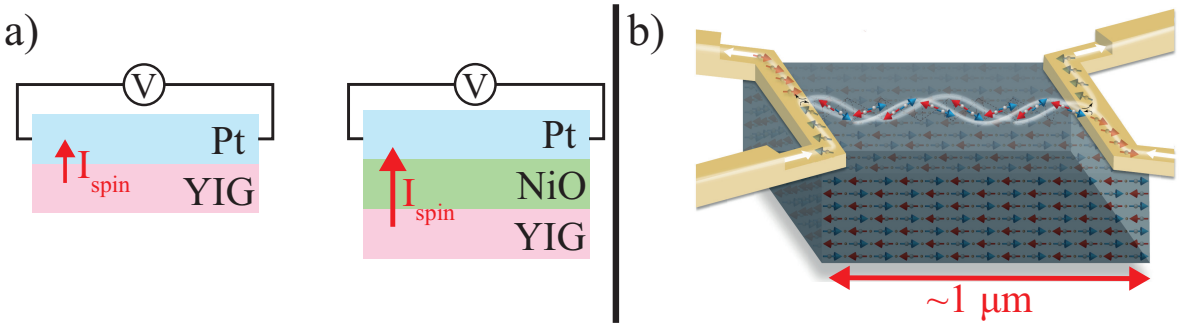

Figure 1.2: a): Schematic representation of the experiment performed by Wang et al. [24]. A spin current I_{spin} is excited in the YIG layer which is detected in the Pt layer. The measured spin current is compared for stacks with and without a 1 nm NiO buffer layer. Suprisingly, in the latter case I_{spin} injected into the Pt has increased. b): Schematic representation of spin current experiments performed by Lebrun et al. [25]. A spin current is injected into the AFM (grey) from Pt lead on the left (yellow), the spin current that reaches the other side is detected by the Pt lead on the right (yellow). Image adapted from [25].

these excitations [23].

Recent interest in spin transport through AFMIs originates from work by Wang et al. [24], the main component of which is summarized in figure 1.2a. In this work, stacks of Yttrium iron garnet (YIG)/ NiO/Pt were investigated, where NiO is a prototypical antiferromagnetic insulator (AFMI). A spin current was injected from the YIG into the NiO layer. The transmitted spin current was detected in the Pt layer. A striking result that was observed, was a significant increase of about 60% of the detected spin current in YIG/NiO/Pt, when compared to YIG/Pt. This enhancement was not observed for the insertion of a non-magnetic insulator like $SrTiO_3$. This result points to very efficient spin conversion at the NiO/YIG and NiO/Pt interfaces. The spin transport through NiO, was postulated to be carried by antiferromagnetic magnons and had a typical diffusion length of about 10 nm. It is important to note that despite the multi-staged spin conversion in these YIG/NiO/Pt multilayers, they can still be favourable in terms of the amount of transmitted spin current due the high spin conductance of the AFMI layer interfaces.

Spin transport through AFMIs has since then been studied in more detail, both experimentally [25–29] and theoretically [30–32]. Recently Li et al. presented evidence pointing at the possibility to transmit an GHz AC spin current across the AFMI CoO [29]. This is surprising since most AFMs do not sustain GHz magnons in favour of THz magnons due to the strong exchange field. Optical measurements showed that no GHz modes were present in the AFMI CoO during the spin transport, suggesting that the spin current is transmitted by antiferromagnetic (THz) magnons. It was concluded however that the exact mechanism how this magnon transport works is still unclear, and much still needs to be understood concerning the frequency mismatch; especially for the goal of long-range transport [29].

Finally, an important recent development in this field is the work presented by Lebrun et al. [25]. They observed long range (~1 µm) spin transport in α-Fe_2O_3 single crystals (another AFMI). The experiment that was performed in their work is illustrated in figure 1.2b. In a Fe_2O_3 (grey) with two Pt contacts (yellow) on top, a spin current was generated in one of the Pt contacts, transmitted through the AFMI Fe_2O_3 and detected at the other Pt contact.

The efficiency of the spin transport was found to be strongly linked to the orientation of the spins in the AFMI, with such long-range spin transport only taking place in the direction parallel to the antiferromagnetic spins. The possibility to facilitate spin transport on the micron lengthscale further broadens the potential of AFMIs in spintronic devices.

To summarize, spin transport in the absence of charge transport has been observed in several AFMIs. They can both transport spin over long distances, as well as sustain AC spin currents with GHz frequencies in spite of the antiferromagnetic dynamics which are typically in the THz range, making them promising as spin transport layers in spintronic applications. This also makes them well suited to work in conjunction with FMs, whose typical dynamical frequencies are in the GHz range.

1.3 Exciting spin dynamics

Another important appeal of AFMs is their spin dynamics at THz timescales, garnering interest as a potential source/detector of THz radiation due to their intrinsic spin dynamics at that timescale [13, 33]. However exciting spin dynamics is challenging as magnetic fields generally do not affect them. Important work in this regard was performed in this regard by Kampfrath et al. [33]. Their experiment is shown schematically in figure 1.3a. The sample, a 45 µm thick free standing NiO crystal, is irradiated with a broadband THz radiation pulse (red). The magnetic field component of this electromagnetic pulse can then couple to the antiferromagnetic spins in the NiO crystal. If the characteristic osciallation frequency of the AFM is present in the broadband spectrum, resonant excitation of spin dynamics is possible. These are then measured with a second pulse, the probe pulse (blue). The change in polarization of this probe pulse can then be used to track the spin dynamics.

The most important results of these experiments are summarized in figure 1.3b. The inset shows the magnitude of the broadband THz pulse profile in red and the absorption by the NiO layer with the blue outline. The antiferromagnetic spins couple resonantly to the magnetic field component of the THz pulse at the characteristic frequency of 1 THz of NiO, denoted by the absorption peak. The corresponding spin dynamics are shown in blue below the inset. The presented work shows that with THz pulses the antiferromagnetic order can be controlled at a fs timescale (the time scale of the THz pulse).

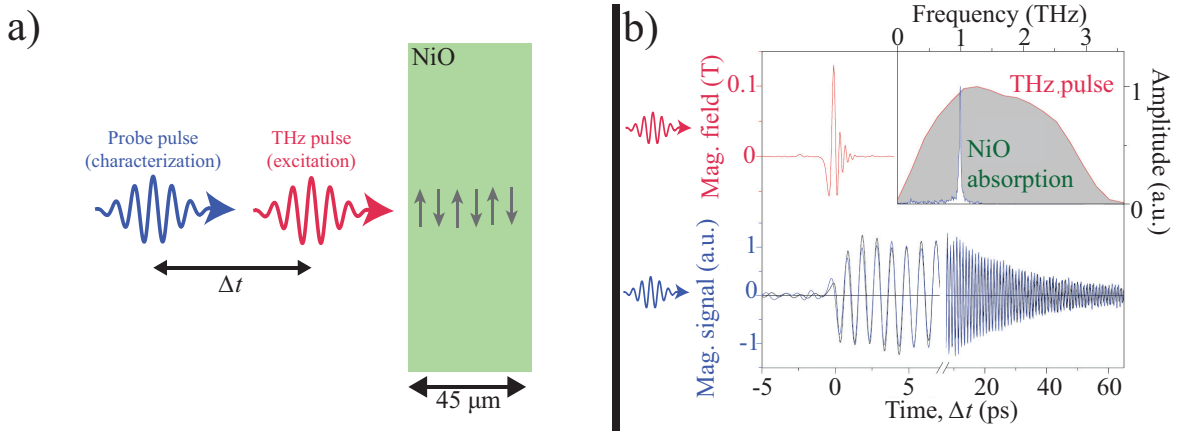

Figure 1.3: a): Illustration of the basic concept of the experiment performed by Kampfrath et al. [33]. A THz optical pulse is used to excite spin dynamics in a thick (45 μm) antiferromagnetic NiO layer. b): Main result from the work by Kampfrath. In the inset, absorption of the THz by the NiO layer is shown. Red and blue time traces show the transient magnetic field from the THz pulse, and the spin dynamics induced in the AFM respectively. Image (b) adapted from [33].

1.4 Noncollinear magnetic multilayers

So where does this thesis come into the story? Looking back at the experiments described in this chapter, there are two particular issues that limit the application of these materials in technological application. Firstly, antiferromagnetic spin dynamics are typically excited in thick free-standing crystals, which limit the flexibility of different material geometries and growth schemes that can be used, as well as the scalability. Furthermore, the THz radiation used to excite spin dynamics is not easily generated and sources such as e.g. a free electron laser used by Kampfrath et al. [33] cannot reasonably be introduced in any sort of portable application as it is already challenging to implement one in a lab setting.

A novel way to investigate the dynamic response of AFMs would be to engineer them into thin film magnetic multilayer stacks and use these to excite antiferromagnetic spin dynamics. These are nanostructures where deposition and patterning of complex multilayered ultrathin (sometimes $<$ 1 nm) films allows for investigation of various magnetic and non-magnetic physical phenomena. One of the prototypical systems to investigate the dynamic response of FMs to spin currents is the noncollinear bilayer system. Such a system is shown in figure 1.4a. It consists of two ferromagnetic layers with OOP (FM1) and in-plane (IP)(FM2) magnetzation respectively, and a non-magnetic metal (NM) spacer layer. Using fs-timescale laser pulses, ps-timescale spin current pulses with the polarization of the affected ferromagnetic layer FM1 (FM2) can be generated, as has been discussed throughout the past decade [34, 35].

When this spin current pulse then travels to FM2 (FM1), their perpendicular angular momentum is absorbed and the orientation of the magnetization in this layer is changed. The relaxation back to the initial state before the spin current pulse arrived then provides information about properties like damping, spin current absorption efficiency and characteristic timescales of the dynamics of the FM under investigation [34, 36]. One advantage of these systems is that the generation of ps-timescale spin current pulse that can manipulate the magnetic order, and the detection of the transient response of the magnetic layers to

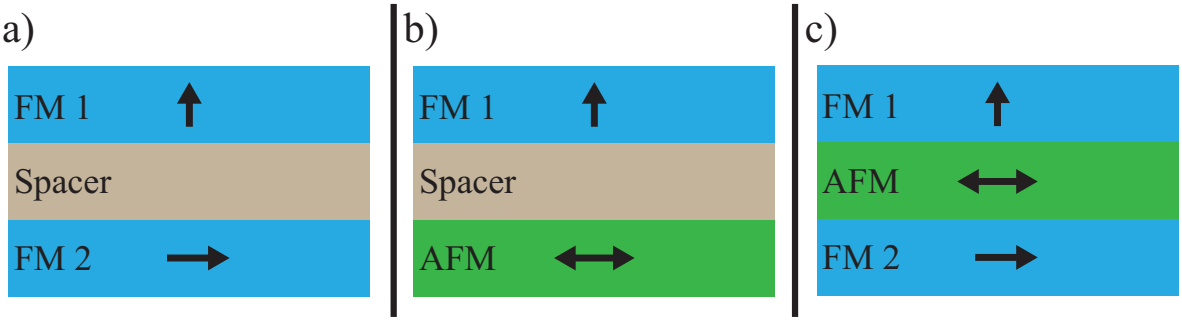

Figure 1.4: a): Schematic illustration of the basic noncollinear magnetic trilayer system, consisting of two ferromagnetic layers FM1 and FM2 (blue) with IP and OOP magnetization direction and a non-magnetic metallic spacer layer. Arrows indicate the magnetization direction. b,c): Schematic illustration of the trilayer systems intended for investigating: transient magnetization dynamics in NiO (b), and magnonic spin transport in NiO (c).

the same spin current pulse, can be combined in one sample. This could potentially bypass the need for a THz radiation source to excite dynamical behaviour in the context of AFMs; instead using the laser-induced ps-timescale spin current pulse from FM1.

There are two ways in which we can employ the noncollinear system in the context of AFMIs, as illustrated by figures 1.4b and 1.4c. First, by replacing FM2 by NiO as shown in figure 1.4b, the noncollinear system can provide a convenient platform to all-optically excite and study spin dynamics in thin film AFMIs. Another interesting option would be to replace the spacer layer by NiO (figure 1.4c), given the efficiency enhancement of spin current transfer in the work by Wang et al. By investigating the dynamic response of FM2 to a spin current pulse from FM1 and comparing this for different spacer layers, the magnonic transport efficiency in NiO can be charted out.

1.5 This thesis

Inspired by the research on AFMs and their favourable properties discussed above, the main goal of the work described in this thesis was thus to investigate the use of NiO in magnetic multilayer stacks, particularly in the noncollinear geometry described in the previous section. Two primary kinds of experiments based upon the geometries presented in figure 1.4b and 1.4c were envisioned on the outset of this thesis, whose research questions can be formulated as follows:

- Can we all-optically excite and measure spin-dynamics in sputtered antiferromagnetic NiO using ps-time scale spin current pulses originating from a nearby (< 20 nm) ferromagnetic layer?
- Can sputtered thin (< 4 nm) NiO films be used as a spin transport layer for ps-time scale optically generated spin current pulses originating from a nearby (< 20 nm) ferromagnetic layer?

Chapter 2 will first introduce the reader to the physics required to understand this thesis. This includes a more in depth treatment of antiferromagnetism in general and the way it manifests in NiO. Furthermore laser-induced ultrafast demagnetization, and the way this leads to

so called optical spin currents will be introduced. Next, the experimental and computational part of this thesis is broken up into three seperate chapters. In chapter 3, a theoretical framework will be presented which describes the optical spin currents, and the way they influence the dynamics of the antiferromagnetic order parameter upon absorption. The computed behaviour was compared to experiments performed on magnetic multilayer stacks, whose design and characterization is reported in chapter 4. Based on the investigated stack geometry time-resolved faraday effect measurements were performed. The attained results are discussed in chapter 5 and compared to the numerical results from chapter 3. Finally, in chapter 6, the reader will be provided with the overall conclusion of the thesis, and an outlook on future research after the work presented in the text below.

Chapter 2

Theoretical background

The essential physical background for understanding this thesis will be presented in this chapter. The overarching theme will be the understanding of the magnetic properties of the specific material of interest for this thesis, the AFMI NiO. However, the starting point will be a basic introduction to nanomagnetism which, for their simplicity, will be based on FMs. Next, the premise of antiferromagnetism will be discussed in section 2.2. Here, the microscopic origin of the antiferromangetic coupling and the magnetic structure of NiO will be discussed. Other important properties of this material, like the domain structure and its relation to strian, as well as the origin of the observed magnonic spin transport will be reported in section 2.3. The final two sections 2.4 and 2.5 will cover the magneto-optical effects used to characterize ferromagnetic layers, and spin current generation by ultrafast demagnetization respectively, required to understand the optical experiments described in chapter 5.

2.1 Nanomagnetism: anisotropy and hysteresis

Before diving into the description of the magnetic material class known as AFMs, it is imperative to understand the different basic magnetic processes that play a role on the sub-micron length scale. This section will introduce the relevant interactions for this thesis for the simplest form of long-range magnetic ordering: ferromagnetism. In FMs, the magnetic moments associated with the localized d- (Co, Fe, Ni) or f-electrons (e.g. Gd) have an energetic preference to align in the same direction.

2.1.1 Direct exchange

The alignment is driven by one of the primary interactions leading to magnetic ordering at the atomic length scale: direct exchange interaction. This interaction arises from an interplay of the coulomb repulsion between nearby electrons and the Pauli exclusion principle, which prohibits two electrons from occupying the same quantum state. For simplicity's sake, a two-electron spin system defined by the atomic spins $\boldsymbol{s}_1$ and $\boldsymbol{s}_2$ can be considered. The exchange energy E_{ex} is then given by [37, 38]:

$$E_{\text{ex}} = \frac{-2\mathcal{J}}{h^2}\boldsymbol{s}_1 \cdot \boldsymbol{s}_2, \tag{2.1}$$

where $\mathcal{J}$ and h represent the exchange integral and Planck's constant respectively. When $\mathcal{J}$ is positive, E_{ex} is minimized when the spins align in parallel fashion. Though direct exchange

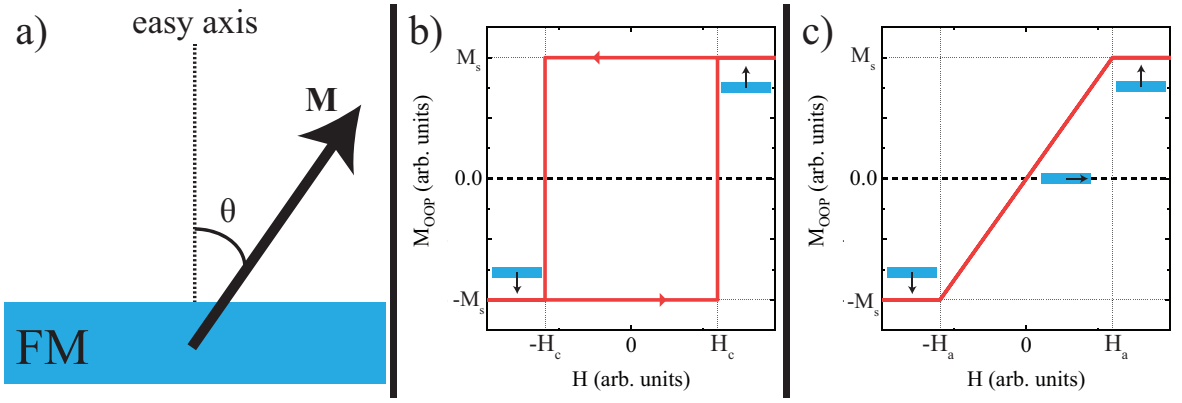

Figure 2.1: a): Illustration of the relevant angle θ in equation (2.4) in case the FM has an OOP anisotropy. b,c): M-H hysteresis calculated from equation (2.4) for FMs with an OOP (b) and IP (c) anisotropy and an applied magnetic field in the OOP direction.

explains the onset of ferromagnetism, it is an isotropic interaction. In nanomagnetic systems the magnetic moments generally have a preferential direction of alignment, caused by magnetic anisotropy.

2.1.2 Magnetic anisotropy

The preferential direction of the magnetic moments can be influenced by the shape of the magnet, the crystal structure as well as symmetry breaking at interfaces with other materials. The simplest form of anisotropy that can be described is when the FM has one preferential axis along which it is energetically favourable to align: the easy axis. In an energetic description, the uniaxial anisotropy E_a can be described as follows:

$$E_\mathrm{a} = K_\mathrm{a} \sin^2(\theta), \tag{2.2}$$

where K_a is the (positive) anisotropy constant and θ is the angle between the magnetic moments and the easy axis as illustrated in figure 2.1a. Besides the anisotropy, another factor that can influence the orientation of a magnetic material is the application of an external magnetic field.

2.1.3 Zeeman-interaction

When a magnetic moment is placed in an external field, there is a preference for alignment with the applied field known as the Zeeman effect. This behaviour is captured at a macroscopic scale by the Zeeman energy E_z:

$$E_\mathrm{z} = -\mu_0 \boldsymbol{M} \cdot \boldsymbol{H}, \tag{2.3}$$

where $\boldsymbol{M}$ is the magnetization, the volume average of all magnetic moments in the FM, $\boldsymbol{H}$ is the applied field, and μ_0 is the vacuum permeability. Based on these simple descriptions for E_z and E_a, it is already possible to gain an understanding of the response of ferromagnetic materials to applied fields. Something that will be applied further in chapter 4 during the characterization of deposited ferromagnetic films.

2.1.4 Magnetic hysteresis

Suppose such a simple FM thin film with uniaxial anisotropy in the presence of a constant applied field $\boldsymbol{H}$. The total magnetic energy E_m can then in the simplest picture be defined as:

$$E_\mathrm{m} = E_\mathrm{a} + E_\mathrm{z} = K_\mathrm{a} \sin^2(\theta) - \mu_0 \boldsymbol{M} \cdot \boldsymbol{H}. \tag{2.4}$$

This description is known as the Stoner-Wolfarth model [39]. It is a macrospin model, meaning that all internal structure of the magnet is ignored and treated as one uniform spin represented by $\boldsymbol{M}$. When equation (2.4) is minimized with respect to the angle θ, it is possible to predict the equilibrium orientation of $\boldsymbol{M}$ as a function of $\boldsymbol{H}$. Two situations are considered: A FM with an OOP easy axis, and a FM with an IP easy axis (with respect to the film). In both cases it is assumed that the applied field points in the OOP direction.

M-H for OOP anisotropy

Firstly, the case with an OOP $\boldsymbol{H}$ and an OOP easy axis of the FM is considered. The response of the OOP component of the magnetization M_OOP to the applied field $\boldsymbol{H}$, defined by equation (2.4), is plotted in figure 2.1. What is seen is a typical easy-axis hysteresis loop. At $\boldsymbol{H} \to \pm\infty$ the Zeeman energy will dominate. All magnetic moments in the material are aligned with the external magnetic field. The magnetization has for that reason a constant value known as the saturation magnetization $\boldsymbol{M}_\mathrm{s}$.

Suppose that the starting situation for the system is fully saturated in the negative direction due to a negative applied field. When the field becomes positive, there will be a competition between the Zeeman energy, which would align the magnetic moments along the positive field direction, and the anisotropy, which promotes keeping the original orientation of the magnetization along the negative direction. When the positive field becomes high enough to overcome the anisotropy barrier, the magnetization will realign along the positive field direction. The field at which this happens is called the coercive field $\boldsymbol{H}_\mathrm{c}$. The magnetization is again saturated, but now along the positive direction. The switch between two distinct magnetization states forms the basis for conventional magnetic memories, where e.g. the positive and negative configurations define logical 0's and 1's.

M-H for IP anisotropy

When the field again points OOP, but the easy axis lies IP, the response of the FM is fundamentally different. The calculated M-H loop for this case is shown in figure 2.1c. Again for fields $\boldsymbol{H} \to \pm\infty$ the magnetization is saturated along the field direction. However, at field strengths smaller than $\boldsymbol{H}_\mathrm{a}$, the anisotropy field, the magnetic system can lower its energy by canting towards the field direction. Coherent rotation of the magnetization towards the field direction upon application of a stronger field is then observed, rather than the abrupt switch when the applied field and easy axis are parallel.

With that, the relevant basic concepts of nanomagnetism for this thesis have been covered. The three contributions to the magnetic energy (exchange, anisotropy and Zeeman energy) will be extensively used in the description of the spin dynamics in AFMs presented in chapter 3. Though the examples shown in this chapter pertain to FMs, it will be shown that the same macrospin formalism can also be applied to other magnetic ordering phenomena, such

as AFMs. The next step in terms of theoretical background will be to actually zoom in on this magnetic material class of interest.

2.2 Antiferromagnetism

Therefore, in this section, an introduction to antiferromagnetism will be provided. Initially, the general concept will be introduced in section 2.2.1 based on the Heisenberg exchange Hamiltonian. To create phenomenological understanding of why antiferromagnetic coupling occurs in insulating materials, a toy-model Hubbard H_2 system will be analysed in section 2.2.2. Finally, a more detailed account of superexchange, the mechanism behind the antiferromagnetism in the AFMI NiO, will be provided in section 2.2.3.

2.2.1 Basics of antiferromagnetism

The difference between FMs and AFMs becomes apparent when again considering the Heisenberg exchange energy: $E_{\text{ex}} = \frac{-2\mathcal{J}}{h^2}\boldsymbol{s}_1 \cdot \boldsymbol{s}_2$. The sign of $\mathcal{J}$ determines the preferential alignment of the two electron spins in the system under consideration. The case of positive and negative $\mathcal{J}$ are shown schematically in figure 2.2a and 2.2b respectively.

FMs have a positive $\mathcal{J}$, leading to a preference for spins to align in a parallel fashion. Negative $\mathcal{J}$, on the other hand, leads in the simplest image to antiparallel alignment of spins. One important feature of the latter case is that it does not exhibit any net magnetization $\boldsymbol{M}$; vectorially adding the magnetic moments in such a system yields zero. AFMs in general, are materials where the inter-atomic interactions promote a magnetic structure with no net magnetization, like that shown in figure 2.2. This magnetic order only pertains below a certain material-specific critical temperature: the Neél temperature ($\boldsymbol{T_N}$), which is the antiferrromgnetic equivalent for the Curie temperature in FMs.

Since AFMs have no net $\boldsymbol{M}$, a different magnetic quantity needs to be used to describe its magnetic state. Consider the two-dimensional AFM shown in figure 2.2c. On this square lattice, it is possible to distinguish between two intertwining FM lattices with opposite polarities denoted by "A" and "B." Since the unit cell of this lattice contains both an up-spin and a down-spin, it is convenient to define the magnetic state as the difference between the sublattice magnetizations $\boldsymbol{M_A} = -\boldsymbol{M_B}$. This Neél parameter $\boldsymbol{L}$ is thus defined as:

$$\boldsymbol{L} = \boldsymbol{M_A} - \boldsymbol{M_B}, \tag{2.5}$$

for such a bipartite (two-sublattice) AFMs. It should be noted that not every AFM can be divided into two FM subslattices. AFMs with a more complex spin structure such as $IrMn_3$ (3-sublattice [40]) and $TbMnO_3$ (spin cycloid [41]) require a more sophisticated way to define their antiferromagnetic state. It should also be noted that, to fully explain all features measured in Raman and Brioullin scattering experiments in seemingly bipartite AFMs like NiO, an 8-sublattice description of the magnetic structure is required [42–44]. For the purposes of this report and for clarity of the following analysis, we will however refer to NiO as a bipartite AFM. This description explains the essential physics for this thesis well and is custom to use in analysis of these transition metal compound AFMs [9, 45]. In this thesis we will therefore be referring to $\boldsymbol{L}$ as the relevant order parameter.

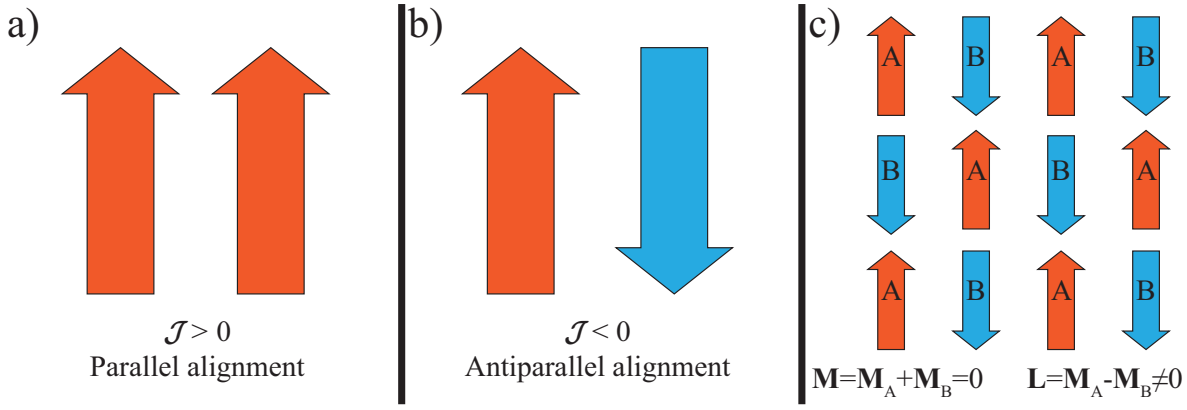

Figure 2.2: a,b): Preferred alignment of spins due to exchange energy for $\mathcal{J} > 0$ (a) and $\mathcal{J} < 0$ (b). c): Simple two-dimensional spin lattice with antiferromagnetic coupling between neighbouring spins. Two spin sublattices can be distinguished denoted by "A" and "B."

2.2.2 Direct exchange interaction; the role of hopping

In order to understand the mechanism that leads to antiferromagnetism in transition metal-oxides like NiO, it is important to understand hopping-mediated exchange. A phenomenological image of this hopping mechanism will be provided based on a Hubbard-type description of the H_2 molecule. For the interested reader a more quantitative and rigorous description of this model will be provided in appendix A.

A schematic representation of the H_2 system is shown in figure 2.3. The model system consists of two hydrogen atoms. Each atom has one associated orbital each of which is orthogonal to the other. These orbitals have associated eigenenergies ϵ_1 and ϵ_2 which will be assumed equal. The first state that will be considered here is one where one electron is introduced to the system which will occupy an orbital associated to either of the two hydrogen atoms. Since the potential barrier between the two hydrogen atoms and their orbitals is not infinitely high, there is a finite probability t that the electron will be transferred from one nucleus to the other. The consequence is that the eigenstate of the electron will be a superposition of the two orbital states.

When however a second electron is introduced in the system, the physics involved become a bit more interesting. Two critical phenomena that need to be accounted for in the analysis are the Coulomb repulsion between the two like-charged electrons, and the Pauli exclusion principle which imposes that the two electron wavefunctions should be antisymmetric with respect to interchange of the two fermions. Note that this wavefunction consists of both the orbital wavefunction as the spin state of the two electrons.

Taking the latter condition into account we can distinguish between two different states. The first state is an ionic state, where the two electrons occupy the same spatial orbital. On the other hand, there is a neutral state, where the two electrons occupy different spatial orbitals. It can be intuitively understood that the ionic state is energetically unfavourable due to the increased Coulomb repulsion between the two electrons occupying the same spatial orbital. Suppose that the energy difference between the ionic and neutral state is given by the parameter U.

An important observation that should be made is that the Coulomb energy penalty U and the transfer probability t are in competition. As t increases, which depends among other

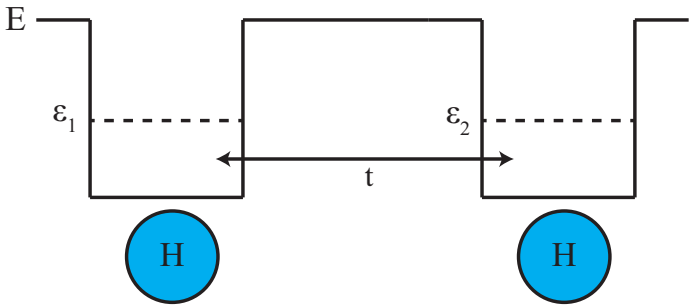

Figure 2.3: Simple sketch of the model H_2 system described in this chapter. It shows the energy landscape of the molecule as two square wells associated with the coulomb interaction between the electron and nucleus. Two spatially separated orthogonal orbitals with associated energy levels ϵ_1 and ϵ_2 are considered. There is a finite probability t of the electrons being transferred between the nuclei.

things on the wavefunction overlap between the two orbitals involved in the hopping process, the probability of the system occupying a state with both electrons on the same atom becomes increasingly likely; leading to metal-like behaviour. Contrarily if U is larger compared to t, the system describes the behaviour of well localized electrons; a situation which is more akin to insulating or molecular systems. In these systems band description of the electronic system is no longer appropriate due to the strong correlation between electrons.

In transition metal oxides like NiO, CoO and MnO, the parameter U is large compared to t, leading to hopping-like transport between neighbouring orbitals. Figure 2.4 illustrates graphically why then this tendency for hopping transport opposed to band-like transport favours an antiparallel alignment. In figure 2.4a it can be seen that the transfer of an electron from the right orbital to the left is allowed and mediated by the hopping parameter t. In a quantum mechanical description this increased possibility for electrons to hop between orbitals can be interpreted as an expansion of the wave function of the electrons towards to other spatial orbital. In this case this orbital is the s-orbital of the other H atom.

On the other hand, in figure 2.4b transfer between the two orbitals for the like spins is prohibited by the Pauli exclusion principle. Thus, the fact that the hopping process in figure 2.4b is not allowed, is the reason why antiferromagnetic coupling is preferred in systems with strong electron-electron correlation. Although this phenomenological explanation and the treatment in appendix A cannot be used to make quantitative estimates, it will now be shown that it can be used to explain the superexchange-mediated antiferromagnetism in NiO.

2.2.3 Superexchange in NiO

NiO crystallizes in a rock salt crystal structure. This crystal and magnetic structure is illustrated in figure 2.5; every metallic cation has six anionic nearest neighbours. In this image white circles represent the negative oxide ions, while the blue and orange circles represent the positive Ni ions. Hence, x, y and z-axes indicated thus correspond to the [0 0 1], [0 1 0] and [0 0 1] axes respectively. When considering the magnetic structure, one can distinguish between two sublattices denoted in blue and orange. These sublattices are characterized by FM planes stacked along one of the four equivalent $\langle 1\,1\,1 \rangle$ directions. Each consecutive plane has a preferred magnetization direction antiparallel to its nearest neighbouring planes.

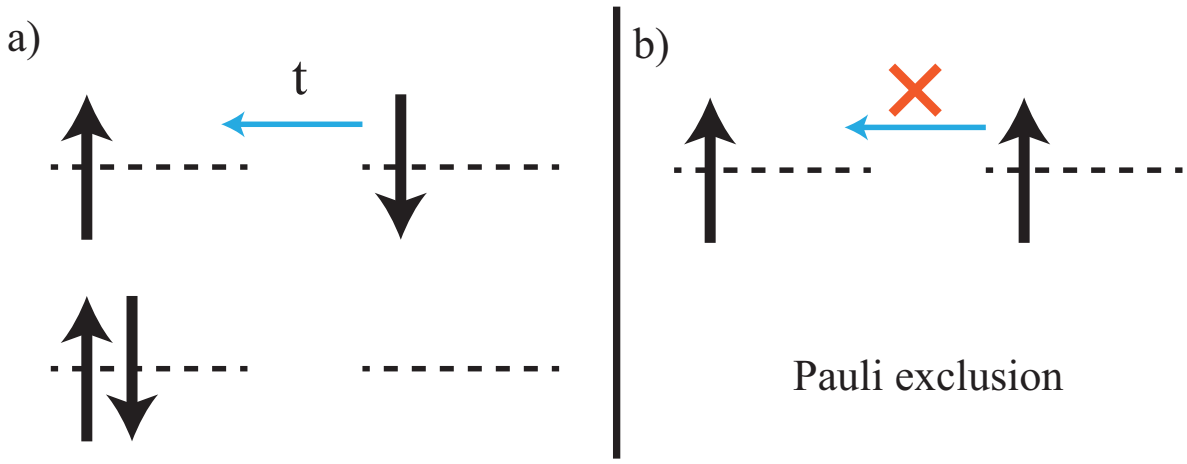

Figure 2.4: Simplified illustration of the direct exchange interaction in the H_2 model system. Antiparallel alignment (a) is energetically more favourable than parallel alignment (b), as in the latter case the exclusion principle prohibits hopping of electrons of like spin to the same spatial orbital.

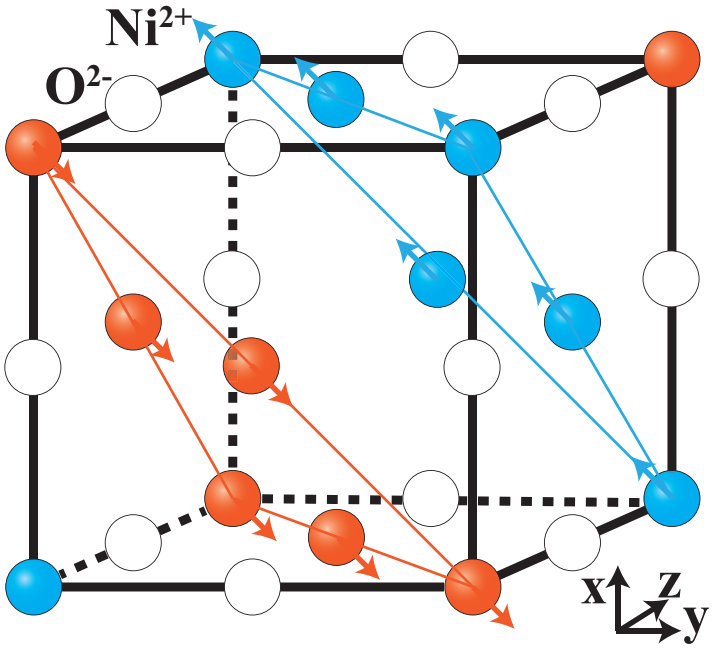

Figure 2.5: Crystal and magnetic structure of NiO. White circles represent the oxide ions, while the coloured atoms denote Ni ions. In the simplest view, we can distinguish two FM sublattices with opposite polarities shown in blue and orange. Note that for image clarity, the oxygen atom at the center of the cubic cell was omitted.

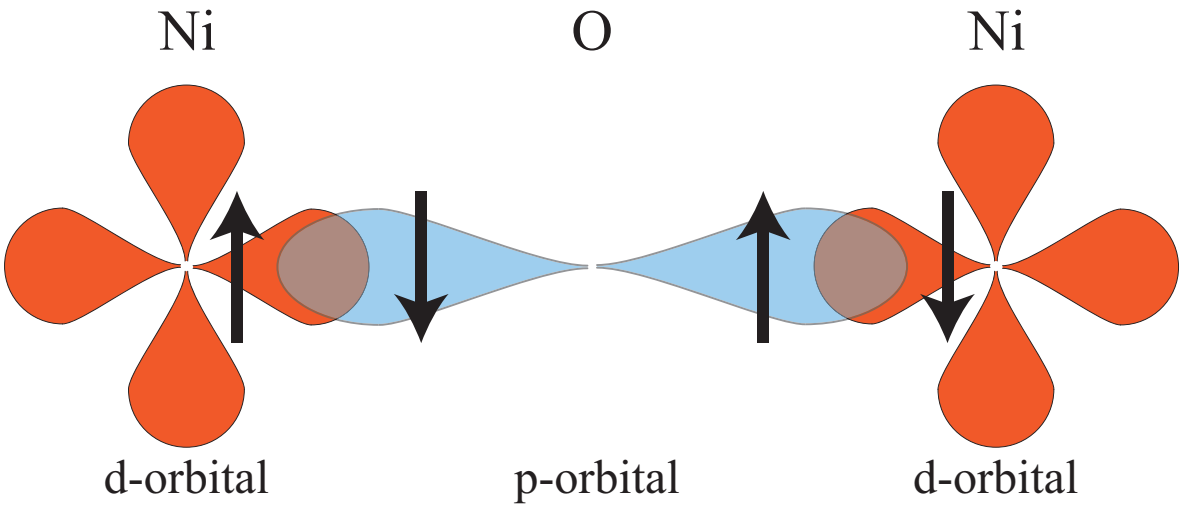

Figure 2.6: Schematic representation of the overlap between p- and d-orbitals of the O and Ni atoms respectively. The combination of the hopping-mediated antiferromagnetic coupling and the singlet state of the O atom due to the full occupation of the orbital leads to the long range antiferromagnetic ordering in NiO.

In order to understand the precise magnetic coupling and interactions as a consequence of the crystal structure, the precise oribtal overlap between two nearest neighbour Ni atoms and their O ligand needs to be considered. Figure 2.6 shows schematically the overlap between the filled p-orbital of the O ligand (blue) and the d-orbitals (orange) from the Ni. As illustrated, the localized nature of the d-orbital wavefunction, yields almost no direct exchange between nearest neighbour Ni atoms. Furthermore, since the 2p orbital in O is fully occupied, the ground state for this orbital has opposite spins for the two electrons occupying this orbital. In the state as depicted, electron transfer from the p-orbital to the d-orbital obeys the Pauli principle. Following the reasoning from section 2.2.2, antiferromagnetic coupling between the d- and p-electrons is energetically favourable as this allows hopping. Due to the singlet state of the O ligand, the 3d electrons of the two Ni atoms will have opposite spins. This kind of exchange via a non-magnetic ligand is known as superexchange.

Superexchange in transition metal oxides was first reported in 1934 by Kramers in MnO [46]. It describes the indirect exchange between unpaired d- or f-electrons on a transition metal cation like Ni^{2+}, Co^{2+} or Mn^{2+} and a non-magnetic intermediate ligand. Quantitatively, it is relatively complex form of exchange, depending among other things on the relative symmetry of the orbitals with respect to rotation around the axis connecting the two atoms [47, 48]. This relative symmetry of the orbitals can break the orthogonality and according to the Pauli principle will lead to the wave function expansion discussed earlier in section 2.2.2. Based on the work by these researchers, the so-called Goodenough-Kanamori (GK) rules were formulated. These rules correctly predict the sign of superexchange for a variety of materials and are given below [37]:

1. "When two cations have lobes of singly occupied 3d-oribtals which point towards each other given large overlap and hopping integrals, the exchange is strong and antiferromagnetic ($\mathcal{J} < 0$). This is the case for 120°/180° M-O-M bonds."

2. "When two cations have an overlap integral between singly occupied 3d-orbitals which is zero by symmetry, the exchange is ferromagnetic and relatively weak. This is the case for ~90° M-O-M bonds."

3. "When two cations have an overlap between singly occupied 3d orbitals and empty or doubly occupied orbitals of the same type, the exchange is also ferromagnetic and relatively weak."

The GK rules above thus predict antiferromagnetic interactions for 180° bonds seen in rock salts, which, as shown, is also what is observed in NiO (e.g. [45, 49]). The magnetic structure in NiO is thus characterised by the 180° superexchange between nearest neighbour Ni ions, which was found by Hutchings et al. to be almost two orders of magnitude stronger than the superexchange with 90° nearest neighbours [9]. Note that this treatment of antiferromagnetism and superexchange is by no means extensive and the interested reader can find a good starting point for further reading to be the three original papers by Kramers, Kanamori and Goodenough [46, 47, 50].

At the same time, the treatment above should be sufficient to understand antiferromagnetism to an extent that allows understanding of the following sections and chapter. It was discussed that AFMs are characterized by the absence of a net magnetization while still maintaining long-range magnetic structure. Also, a proper look at the concepts of superexchange and hopping-mediated exchange as the origin of the antiferromagnetic properties of the material of interest for this thesis, NiO, has been supplied.

2.3 Further properties of nickel oxide

Though magnetism in NiO is already an interesting topic, there are a few other important material properties of this material that need to be discussed. Therefore, in section 2.3.1 the magnetoelastic properties and domain structure of NiO will be elucidated. Particularly, the relation between antiferromagnetic domains and crystal quality will be stressed. Finally, in section 2.3.2 the antiferromagnetic resonance (AFMR) modes and their non-degeneracy will be introduced to explain why magnonic spin transport is even expected in materials like NiO, as this possibility is explored in experiments described in chapter 5 and since it is not a trivial result.

2.3.1 Crystal and magnetic structure of NiO

In research into antiferromgnetic materials NiO has played a central role for its simple crystal structure and well understood spin structure. It therefore is a prototypical AFM that has been used in experimental work on a variety of different topics like exchange bias [51–53], excitation of THz dynamics [17, 18, 33] and magnonic spin transport [54].

As was shown in figure 2.5, spins in NiO align in ferromagnetic planes stacked along one of the four equivalent $\langle 1\,1\,1 \rangle$ directions. Magnetostriction due to the FM ordering in the planes leads to a small contraction along the axis perpendicular to the FM planes [55, 56]. Furthermore, magnetic anisotropy within the AFM leads to the preference for the Neél parameter $\boldsymbol{L}$ to align along one of the three $\langle 1\,1\,2 \rangle$ axes, caused by dipolar interactions between the different sublattices [44]. This ordering within the FM plane leads to another contraction

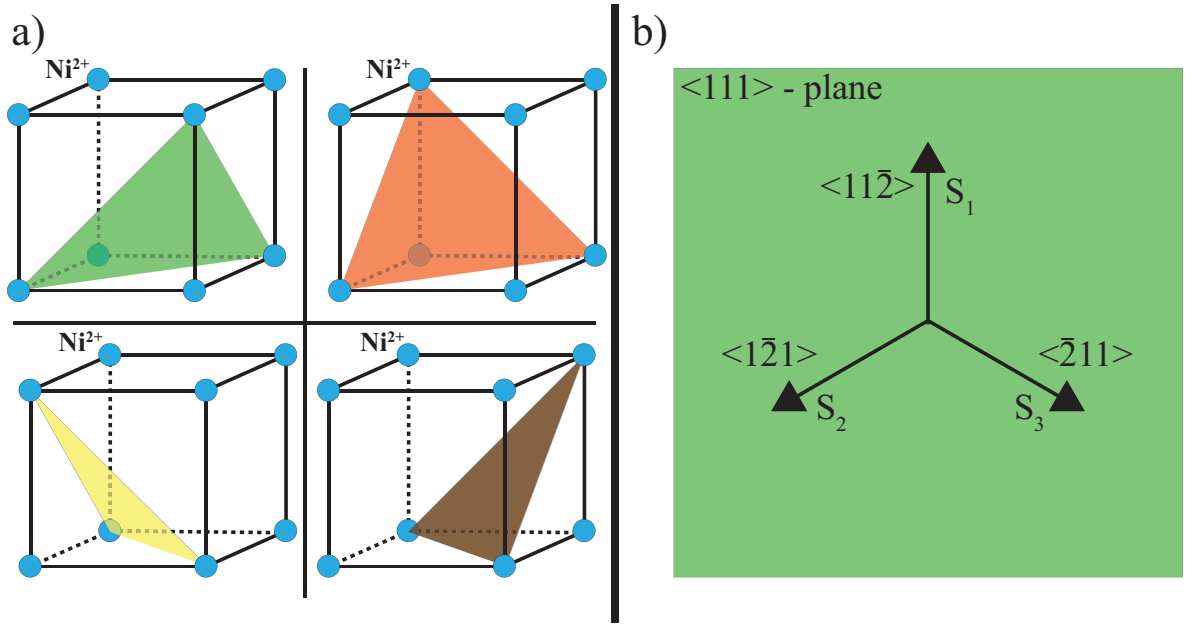

Figure 2.7: a): Schematic representation of the four different ferromagnetic plane orientations in NiO, which define the T-domains. O and face Ni atoms are omitted for image clarity b): Illustration of the three possible stable IP spin axes denoted by S_1, S_2 and S_3.

along the spin axis [56]. The antiferromagnetic order and hence the lattice distortions set in at T_N = 525K (i.e. well above room temperature).

The four FM plane orientations (T-domains) and three spin axes (S-domains) are illustrated in figure 2.7a, and 2.7b respectively, and give rise to 12 different possible domains. These domains are regions in which the Neél parameter points in one uniform direction. The presence of these different domains complicates magnetic measurements in this material, as well as the interpretation [56, 57]. These domains cannot be imaged through the magnetization-sensitive methods for domain visualization in FMs, like MOKE or the Faraday effect (FE). Methods that have been shown effective in distinguishing these domains include inelastic neutron scattering [8, 56], second harmonic generation [21] and birefringent effects [58].

Since the magnetic structure couples to the lattice through magnetostriction, it is possible to influence the magnetic and domain structure through the application of small strains along one of the $\langle 1\,1\,1 \rangle$ directions, especially at high temperature when the domain walls are mobile [8]. Furthermore it has been shown that the number of T-domains can be reduced significantly by performing a field anneal step in the fabrication process of NiO [59]. On the other hand, the sensitivity of the magnetic structure to strain effects, implies that stacking faults, edge dislocations and defects can significantly influence the magnetic structure of the AFMI [45].

Control over and information about the twinning structure, and the spin domains are important for experiments involving spin conversion at an interface between a metal and a magnetic insulator, where the relative orientation of the magnetization/Neél components determine the efficiency of angular momentum conversion [60, 61]. This conversion is crucial when attempting to inject spin currents into AFMs, as the spin-polarized itinerant electrons

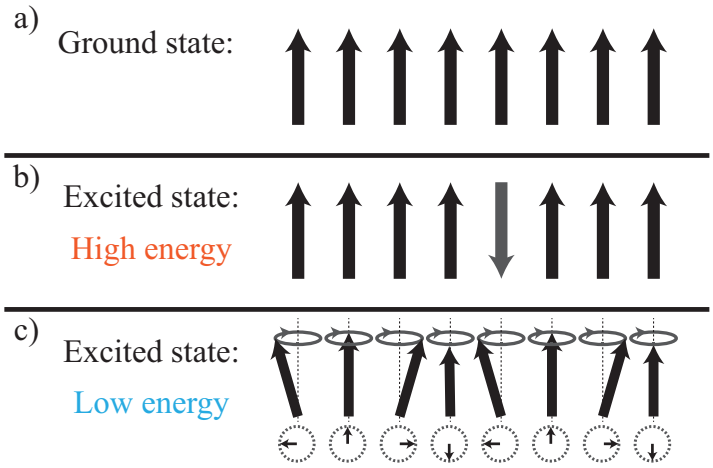

Figure 2.8: Introduction to magnons. Three states of a simple FM are shown: the ground state (a), and two excited states (b,c), where the angular momentum loss is represented by one spin flip (b) and a coherent excitation (c) of the magnetic moments. In (c), also a top view of the magnetic moments is shown.

cannot propagate in AFMIs. Any spin current in these AFMIs is hence carried by low energy magnetic excitations known as magnons.

2.3.2 Magnonic spin transport in AFMs

For an introduction to the concept of the magnon, it is more instructive to first discuss magnons in FMs due to their inherently simpler magnetic structure; before moving on to antiferromagnetic magnons. Consider the simple FM shown in figure 2.8a, where all spins are parallel and anisotropy makes them point up. In a naive picture the excited magnetic state would be represented by figure 2.8b, where one spin is pointing in the opposite direction. However, due to direct exchange the antiparallel alignment between the flipped spin and its neighbours is highly energetically unfavourable. Therefore, lowest energy excitations are not characterized by spin flips, but by small collective deviations of neighbouring spins from their preferential orientation, as shown in figure 2.8c.

When the spins are deviated from these preferential orientation, they will start precessional motion known as Larmor precession. The most important consequence of this precession is that, if there is a phase difference between the precession of neighbouring spins, these collective exciations can behave like a traveling wave. These collective excitations are known as magnons and are quasiparticles with an associated amount of energy and (crystal) momentum. Recalling that these magnons are a way for the FM to lower its total magnetic moment, conservation of magnetic moment suggests that these magnons carry a net amount of magnetic moment. By merit of their crystal momentum, these magnons can hence carry a spin current through the material.

Spin transport in AFMIs works on the basis of the same principles. Though itinerant electrons cannot propagate through these insulators, the spin current can still be carried by magnons. To illustrate in more depth what antiferromagnetic magnons look like, and why they can transport net angular momentum in NiO but not in many other AFMs, the antiferromangetic resonance (AFMR) magnon mode will be considered. This is an excitation

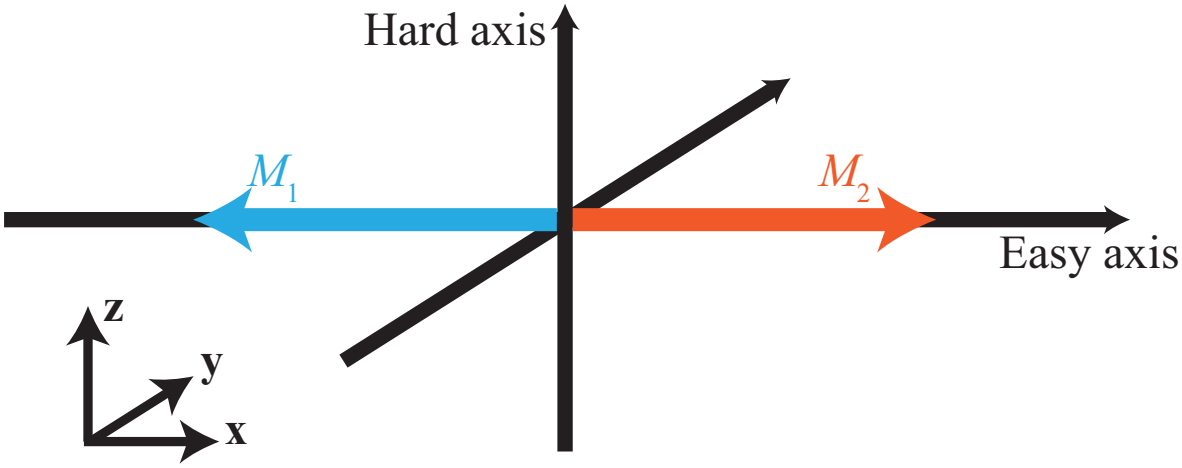

Figure 2.9: Schematic of the model system described in this section in its equilibrium orientation. The x-axis is the easy IP axis, while the z-axis is the OOP hard axis for the sublattice magnetizations. The magnetic sublattices are shown in blue and orange.

similar to the one shown in figure 2.8c, but without the phase difference between neighbouring spins and including spin excitations of both lattices. The starting point to the introduction of these antiferromagnetic precession modes will be the system free energy density:

$$E = \frac{H_E}{M}\boldsymbol{M}_1 \cdot \boldsymbol{M}_2 - \frac{H_\parallel}{2M}\{M_{x1}^2 + M_{x2}^2\} + \frac{H_\perp}{2M}\{M_{z1}^2 + M_{z2}^2\}, \tag{2.6}$$

where $\boldsymbol{M}_1$ and $\boldsymbol{M}_2$ represent the sublattice magnetizations of sublattices 1 and 2 respectively, M is the magnitude of the sublattice magnetization, and $H_\parallel$, $H_\perp$, H_E are the IP easy-axis anisotropy field, the OOP hard axis anisotropy field and the exchange field respectively. For NiO $H_\parallel$, $H_\perp$, H_E are 0.64, 0.011 and 964 T respectively [62]. In this description the Cartesian coordinate system shown in figure 3.4 was assumed, where the xy-plane is the easy FM plane for the sublattice magnetization and the z-direction is the hard-axis (OOP) direction. From simple energy minimization it can be shown that the ground state is defined by antiparallel alignment of sublattices along the x-direction.

Using equation (2.6) the magnetization dynamics can be derived using the Landau-Lifschitz equation [63]. For the antiferromagnetic system this equation is given by:

$$\frac{d\boldsymbol{M}_{1,2}}{dt} = -\gamma \boldsymbol{M}_{1,2} \times \nabla_{\boldsymbol{M}_{1,2}}(E(\boldsymbol{M}_{1,2})), \tag{2.7}$$

where γ is the gyromagnetic ratio, and the rightmost term, $\nabla_{\boldsymbol{M}_{1,2}}(E(\boldsymbol{M}_{1,2}))$, represents the effective field derived from the free energy given in equation (2.6). By considering a harmonic perturbation from the ground state two different antiferromagnetic resonance (AFMR) modes with angular precession frequencies ω_α and ω_β can be derived [32]:

$$\omega_\alpha^2 = \gamma^2 2 H_E H_\parallel, \tag{2.8}$$

$$\omega_\beta^2 = \gamma^2 2 H_E (H_\parallel + H_\perp). \tag{2.9}$$

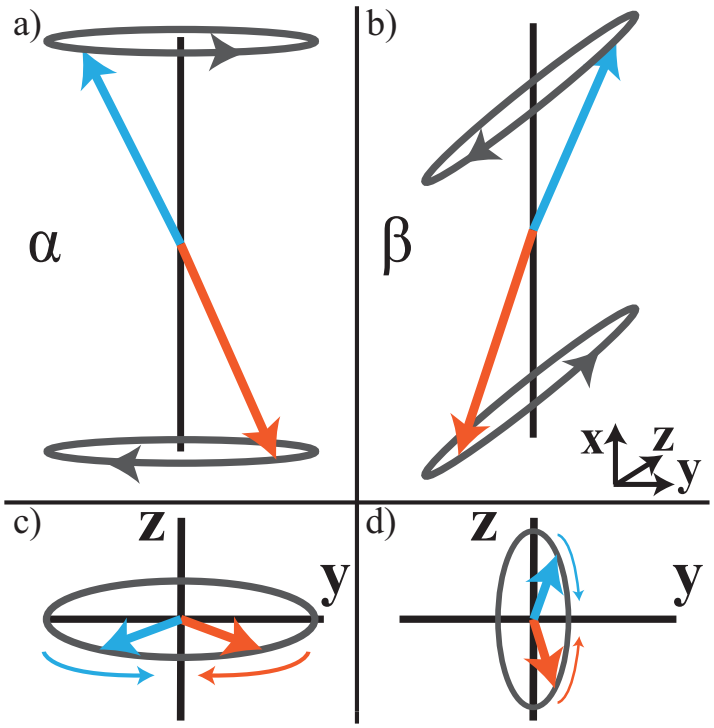

Figure 2.10: Schematic depiction of the two AFMR modes in NiO. a,c): Side (a) and top (c) view of the α AFMR-mode in NiO showing elliptical precession with the major axis along the IP y-axis. b,d): Side (b) and top (d) view of the β AFMR-mode in NiO showing elliptical precession with the major axis along the OOP z-axis. Image based on figure 5 a and b from reference [32].

A derivation of this result is supplied in appendix B. What is important to note from equation (2.8) and (2.9) is that the two principal modes are non-degenerate due to the hard-axis anisotropy $H_\perp$. These two modes are illustrated in figure 2.10.

Figure 2.10a and 2.10c show a side and top view of the α-mode respectively. The sublattice magnetizations precess along an elliptical trajectory in the yz-plane, with the ellipses major axis along the IP y-direction. Note that the sublattices precess in opposite direction. This mode has an oscillating magnetic moment component along the z-axis and an oscillating component of the Neél parameter along the y-axis.

The β-mode shown in figure 2.10b (side) and 2.10d (top) on the other hand follows an elliptical trajectory in the yz-plane with the major axis along the hard z-direction. Consequently, it has an oscillating magnetization component along the y-axis and an oscillating component of the Neél parameter along the z-axis. Due to the hard axis magnetic structure of the material these two magnon modes have different energies. They do however carry the same amount of angular momentum. Furthermore, due to the different precession direction of the magnetization component the group velocity of the two excited magnons is opposite [64]. If the two modes were degenerate, both modes would be excited equally efficient, leading to no net spin current. However due to the hard-axis anisotropy like in NiO the population of the two magnon modes will be different such that a net spin current can be transported through the AFM without any charge displacement. This property of these hard-axis AFMs has been an important impetus for research into these kind of magnetic materials, as no external applied field is needed to lift the degeneracy [32].

Subsequent spin transport by an accumulation of magnons with a certain amount of angular momentum can then be described in terms of diffusive motion of the magnon population [24,32,64]. It has been shown in recent years that particularly the domain size is critical for the distance over which magnon-carried spin currents can be transported; ranging from a few nms in thin films of NiO [24,65] up to several microns in high quality Fe_2O_3 crystals with large single domains [25]. This suggests that magnon-domain wall scattering is a limiting factor for this kind of spin transport and good control over the magnetic structure is required for efficient spin transport.

The relevant aspects of antiferromagnetism for this thesis have now been discussed. An introduction to the very basics of antiferromagnetism through direct exchange between neighbouring spins was used as a starting point for the explanation of superexchange. This magnetic interaction between metallic ions via a ligand atom was shown to be the cause of antiferromagnetism in the compound NiO, the AFM of interest in this work. From this, it was shown that due to the specific magnetic structure of this material there is a degeneracy of the collective excitations of the spin system known as magnons. This allows it to carry spin currents without artificially lifting the magnon mode degeneracy by applying an external magnetic field [32].

2.4 Magneto-optic effects

The AFMs that are used in optical measurements in chapter 5 are implemented in magnetic multilayers, where different layers of magnetic and non-magnetic materials are stacked on top of each other (further discussion in chapter 4). To characterize ferromagnetic films, a central role in this thesis was played by so called magneto-optic effects, which probe the magnetization of a material. This is a broad term for effects that change the polarization

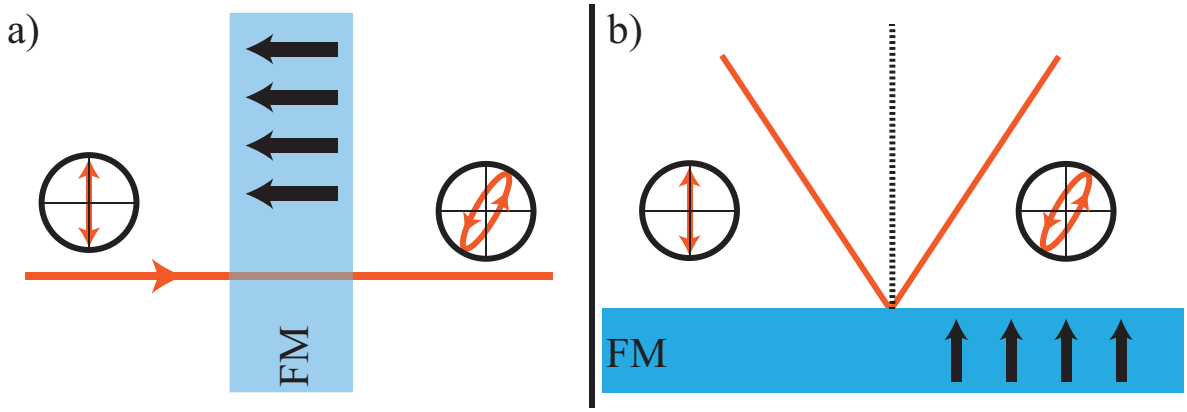

Figure 2.11: Schematic representation of the change of the linearly polarized light transmitted through (a) or reflected upon normal incidence from (b) by a material with an OOP magnetization (component).

state of light based on the magnetic properties of the material. In this section a brief overview of the origin of two of these effects: FE and MOKE.

The FE is illustrated in figure 2.11a. Linearly polarized light is incident on a (partially) transparent material with an OOP magnetization. Upon transmission two primary changes can be observed in the polarization state of the light: a rotation of the polarization θ_F and a change in the ellipticity η_F. To understand this, plane waves of linearly polarized light of frequency ω are considered. As linearly polarized light is a superposition of left and right-handed circularly polarized light, the total electric field of the wave can be written as:

$$\boldsymbol{E}_{\text{lin}} = E_0[\exp(i\{k_+ z - \omega t\}) + \exp(i\{k_- z - \omega t\})], \tag{2.10}$$

where E_0 is the magnitude of the electric field component of the light, and k_+ and k_- represent the wavenumber for counterclockwise (CCWP) and clockwise (CWP) circular polarization of the electric field respectively, with the z-direction defined as the propagation direction of the light.

If both wavenumbers are equal for CCWP and CWP light, the light remains linearly polarized upon propagation through the material. When the phase velocity becomes dependent on the handedness of the light (i.e. $k_+ \neq k_-$), a phase difference will be imposed on the light, depending on the distance the light propagates through the material. This then leads to a rotation of the polarization vector. If not only the phase velocity is different but also the absorption of CCWP and CWP, an additional ellipticity will be induced due to the prevalence of one of the two circular polarization eigenstates.

Microscopically the difference in propagation properties can be understood by considering the fact that circularly polarized light carries an angular momentum quantum. This angular momentum quantum points in the propagation direction of the light, and has a positive or negative sign depending on whether the light in question is CCWP or CWP. If the material through which the light propagates has its magnetization (component) parallel to the light angular momentum, the two circular polarization states have different selection rules for the orbital quantum numbers of dipole transitions that can be excited, which are coupled to the split density of states for up and down spin-polarized electrons. This alters the permittivity for the two polarization states, which is in turn observed as the Faraday rotation and ellipticity

[66].

MOKE is in many aspects similar to FE. The main difference is that instead of picking up the polarization rotation and ellipticity through transmission, the light is reflected from a magnetic surface instead. Many of the arguments above still hold: the difference in absorbance and reflectance is again caused by the coupling between the angular momentum of the magnetization and that of the two circular polarization states of the incident linear light. In order to be sensitive to OOP components of the magnetization, the light thus has to propagate almost normal to the sample normal, so that the light angular momentum is almost entirely parallel to the OOP direction.

The magnitude of the rotation and ellipticity can be shown to be proportional to the magnetization $\boldsymbol{M}$ of the sample and can hence be used as a probe for this quantity in thin films of magnetic material [67]. Note that, as an AFM has no net $\boldsymbol{M}$, no information about the magnetic state of AFMs can be obtained, except when a finite magnetic moment is induced by either a magnetic field or by a another source of angular momentum like a spin current.

2.5 Laser-induced ultrafast demagnetization

Optical spin currents excited by ultrafast demagnetization were used in this thesis to investigate the response of the magnetic order parameter $\boldsymbol{L}$. In this section an explanation of the processes behind this laser-induced demagnetization will be introduced, based on the 3-temperature model. Of particular interest are the spin currents that are observed upon ultrafast demagnetization. An overview will be given of two models that are used to explain the nature of these spin current: the superdiffusive spin current model proposed by Battiato et al. [69], and the dM/dt description by Choi et al. [70].

2.5.1 3-Temperature model

Laser induced ultrafast demagnetization was first observed in Ni thin films by Beaurepaire et al. [68]. The main result of this work is shown in figure 2.12a. This figure shows the normalised remenance ($\propto \boldsymbol{M}$) of the Ni film after some time Δt after the arrival of an intense 180 fs laser pulse. It can be seen that after the arrival of the laser pulse at $\Delta t = 0$, the magnetization in the layer is quenched to roughly half its original value on a sub-picosecond timescale. After this, the film returns to its original state, recovering its magnetization

One explanation was provided in the same paper through the three-temperature model. In this model a distinction is made between three coupled thermodynamic systems describing the electronic, spin and phonon degree of freedom, each with a characteristic temperature T_e, T_s and T_p (Fig. 2.12b). Understanding of the whole demagnetization process then starts at the excitation of the electron system and the associated increase in T_e. The fs laser pulse with frequency ω impinging on a metallic sample leads to electron excitations with energies up to the $\hbar\omega$. This nonequilibrium distribution then thermalizes within itself through e-e interactions, leading to a Fermi-Dirac distribution representing the instantaneous electron temperature [71, 72].

A typical trace of the subsystem temperature as a function of the delay calculated with the 3TM is shown in figure 2.12c. Realistic values from Beaurepaire's original paper were used [68]. As can be seen, the electron system is strongly heated first within 100 fs (instantaneously in the model), after which energy is transferred to the spin and phonon subsystems through different scattering mechanisms. The heating of the spin subsystem is what drives the ultrafast

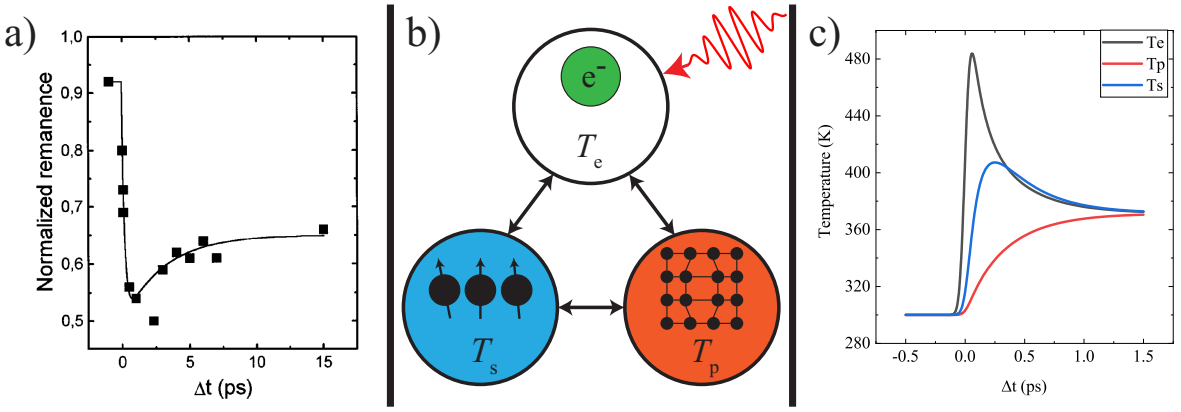

Figure 2.12: a): Ultrafast demagnetization in a 20 nm Ni film, image adapted from [68]. b): The three interacting thermodynamic systems in the 3TM, the electron system, spin system and lattice system transfer energy and angular momentum between eachother after laser excitation. c): 3TM calculation to illustrate the response of the three temperatures after laser excitation of the electron system. Realisitc parameters from [68] were used.

demagnetization observed in the experiments described above. As the net magnetization of a FM is decreased upon the temperature approaching the Curie temperature from below [37].

Optical spin current

The angular momentum that is dissipated from the spin system is accompanied by a spin current that has the same polarization as the ferromagnetic layer affected by the laser pulse. One of the first observations of these optical spin currents was shown by Malinowski et al. [73]. In this work, two FM layers were separated by a thin spacer layer. Upon demagnetization, it was observed that the demagnetization of these two layers behaved differently depending on whether the spacer layer was conducting or insulating, suggesting that angular momentum transferred by itinerant electrons is an aspect that needs to be taken into consideration.

Although it has been unequivocally shown that spin currents are being generated, there are different models that attempt to explain the origin of these spin currents. Battiato et al. proposed a model where angular momentum is carried by hot electrons with different scattering rates depending on their spin polairzation [69, 74]. Although several experiments could be explained based on this description (e.g. [73, 75]), it neglects diffusive motion of electrons which Choi et al. found to be critical for a full description of their experiments [70]. In their work it was shown that taking into account the spin angular momentum dissipated from the spin system, as in the 3TM interpretation, could also offer a full explanation of the observed behaviour of the spin accumulation after transport through a thick spacer layer. The spin generation was then linked to the time derivative of the demagnetization curve in figure 2.12, where the loss of magnetization is converted into spin current.

Though the exact nature of these optical spin currents is still under debate, they still have been a major workhorse in studies investigating the properties of magnetic multilayer systems in contemporary spintronics [34,76,77]. In this thesis, we will use this well established method of generating spin currents (i.e. ultrafast demagnetization) to investigate spin transport and transient magnetization dynamics in AFMs.

Chapter 3

Simulation results

In this chapter, the main numerical efforts for this thesis are presented. Spin transport through the multilayer stack after the ultrafast laser-induced demagnetization is modelled by the spin diffusion equation, similar to Choi et al. [70]. Based on this description, quantitative estimates of the spin accumulation impinging on the AFM can be made. These calculations and the most important physical concepts behind it are introduced in section 3.1. In the end, the main interest is in the response of the antiferromagnetic order parameter to the impinging spin accumulation. To quantify this response a macrospin model based on the micromagnetic free energy of the AFM is presented, following a description by Cheng et al. [19]. From this model the response of the sublattice spins to the spin current can be characterized for arbitrary stack geometries. The calculations of the spin dynamics are presented in section 3.2.

3.1 Model description: spin transport and dynamics

Before moving on to results, the spin transport model, the spin dynamics model and the way the coupling between these two models is described will be introduced. First, in section 3.1.1 a model for the relation between demagnetization and subsequent spin generation is presented. Furthermore the diffusive equations that describe transport of the generated mobile spin angular momentum will be briefly discussed. Next, in section 3.1.2 the response of the antiferromagnetic order parameter to a perpendicularly polarized spin current will be explored. Specifically the coupling of the spin accumulation and conversion at the normal metal (NM)/AFM interface and the way this relates to the torques on the magnetic sublattices will be expanded upon.

3.1.1 Spin transport in magnetic multilayers

Ahead of the discussion of the exact physical description of the models, it is important to understand the main aim of the experimental and computational work below. Basic schematics of these two kinds of magneto-optical experiments that have been performed are shown in figure 3.1. In figure 3.1a the experiment geometry for transient magnetization dynamics in an AFM is shown. An ultrafast laser pulse demagnetizes the FM layer with perpendicular magnetic anistropy (PMA), leading to an OOP polarized spin current through the NM to the AFM. Angular momentum transfer to the AFM spins at the interface can then lead to

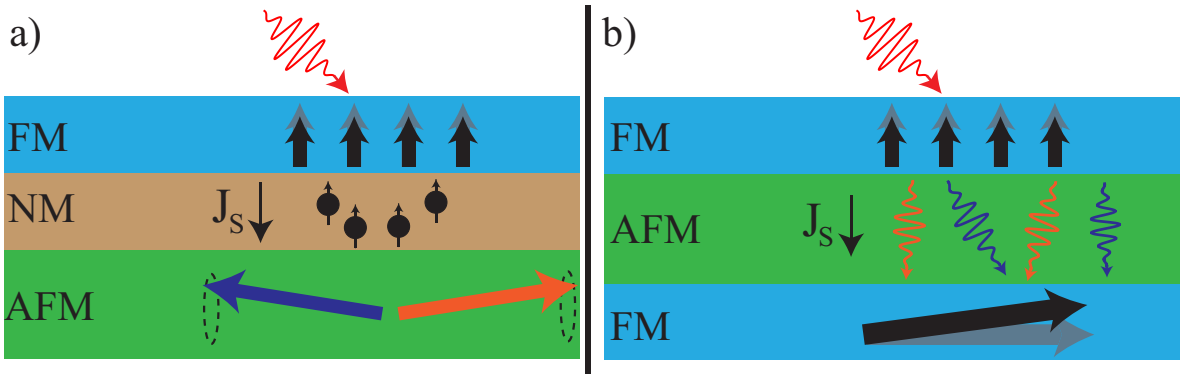

Figure 3.1: Overview of the optical experiments that have been performed for this thesis. a): Experiments where optical spin currents from a FM layer with PMA is absorbed in the AFM, where they can cause transient magnetization dynamics. b): Optical spin current transport through an antiferromangetic buffer layer. The efficiency of this spin transport can be gauged by the response of an in-plane ferromagnetic layer to any impinging spin current.

a transient OOP magnetization component in the AFM, which can be detected through the FE or MOKE. Figure 3.1b shows the experiments that were performed to test the use of very thin (around 4 nm) AFMI layers as a spin transport layer in these optical spin current experiments. A magnon carried spin current is expected to be generated in the AFM as a consequence of the spin accumulation at the FM/AFM interface, again caused by the laser-induced demagnetization of the FM layer with PMA. If the spin angular momentum from this magnon current is then absorbed by an IP ferromagnetic layer, the angular momentum transfer is expected to lead to a small OOP canting of this IP layer.

This section introduces the main concepts of the spin diffusion model, particularly in the context of the experiments related to transient magnetization dynamics (fig. 3.1a). The spin diffusion model and the way it can be used to calculate the spin accumulation at the NM/AFM interface will be discussed. The main aim is to provide the reader with the most essential aspects of the model so that the physics can be understood. Further details like the full set of equations that are solved, the imposed boundary conditions and material parameter are presented in appendix C.

Spin diffusion equation

The main physical workhorse in both experiments is the generation of optical spin currents through ultrafast laser-induced demagnetization. The transport of the generated spin accumulation is what is of interest for this thesis, and will be calculated from the spin chemical potential μ_s. This quantity is schematically illustrated in a band picture for the two spin species for a normal metal in figure 3.2a; it is defined as $\mu_s = \mu_\uparrow - \mu_\downarrow$, where $\mu_\uparrow$ and $\mu_\downarrow$ are the Fermi levels for up and down polarized electrons respectively. μ_s can be related to the local magnetization M_l as follows:

$$M_l = \mu_s \mu_B N(E_F), \tag{3.1}$$

where μ_B is the Bohr magneton and $N(E_F)$ is the density of states (DOS) at the Fermi level. Note that this only holds when the DOS is constant within a margin $\pm\mu_s$ from the Fermi

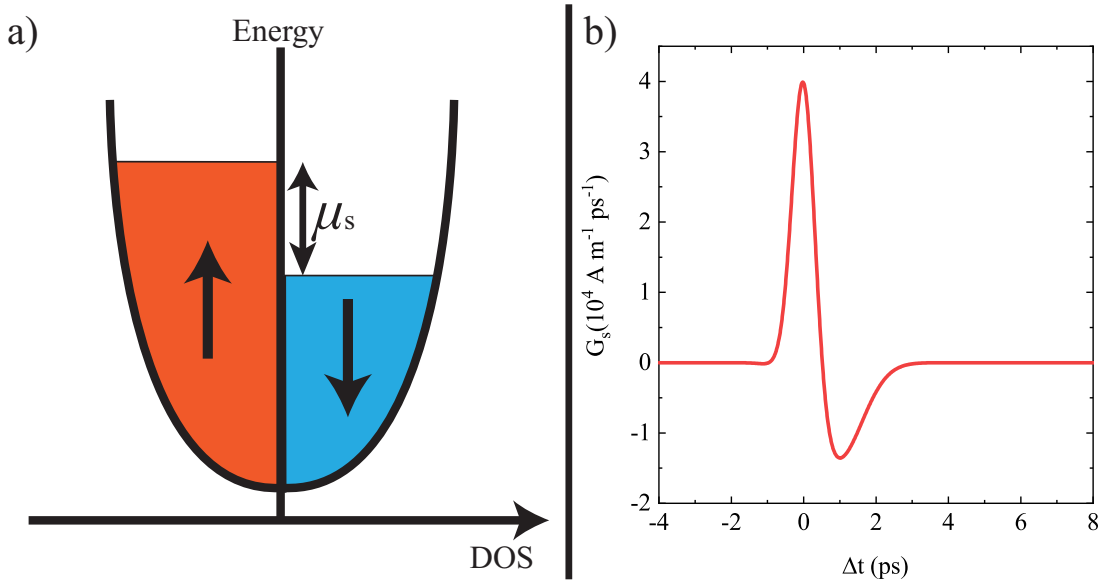

Figure 3.2: a): Schematic illustration of the Fermi-level splitting μ_s in a normal metal upon spin accumulation. b): Typical time derivative of an ultrafast demagnetization process as shown in figure 2.12a.

energy, which is an acceptable approximation for Cu [78], where the spin transfer between the spin accumulation and the AFM takes place. By means of equation (3.1), the spin accumulation at the NM/AFM interface can be expressed in common magnetic properties. The spin diffusion equation is used as a first order estimate of the spin transport as a consequence of spin accumulation in these magnetic multilayers. It should be noted that especially for films much thinner than the inelastic scattering lengths of the used materials, this model is expected to underestimate the magnitude of the spin current. Many of the electrons will in that case not have had sufficient collisions for the transport to be in the diffusive regime and are hence expected to be ballistic and have velocities near the Fermi velocity. However, since the main focus of this work is on the response of the antiferromagnetic order parameter, and the spin current pulse is the only stimulus, mostly the amount of attenuation is of interest. For these purposes the model presented is expected to suffice. The spin diffusion equation is given by [79, 80]:

$$\frac{\partial \mu_s}{\partial t} = D\frac{\partial^2 \mu_s}{\partial z^2} - \frac{\mu_s}{\tau} + G_s, \tag{3.2}$$

where D is the spin diffusion constant, τ is the spin relaxation time, and G_s is a generation term assumed to only be non-zero in the FM layer, where demagnetization takes place. Since the laser spot diameter (10 µm) where demagnetization takes place is large compared to the total metallic layer thickness (20-30 nm), the relevant spin transport only takes place along the OOP direction (i.e. the z-direction). The system has for that reason been approximated as one-dimensional and spin diffusion in the lateral (IP) directions has been neglected.

To quantify G_s, Choi et al. [70] introduced a model where the spin angular momentum

generation was directly coupled to the demagnetization of the corresponding layer. Magnon-electron coupling would lead to a proportionality of the spin generation rate G_s with the time derivative of the demagnetization $-\frac{dM}{dt}$. A simple mathematical expression derived from demagnetization measurements on a Co/Pt multilayer with PMA is plotted in figure 3.2b [70]. The laser fluence in this measurement was 1.7 mJ/cm^{-2}. The functional form of this spin generation profile is given in appendix C, and will be used in the numerical work presented below unless stated otherwise. Note that, to quantify the effects of laser fluence on the generated spin currents, an explicit model of laser heating and subsequent demagnetization needs to be introduced, which is beyond the scope of this thesis.

Boundary conditions

Equation 3.2 was thus solved numerically for the three different layers: a Pt capping layer, Co/Ni ferromagnetic multilayer and the Cu buffer layer, where the latter two layers correspond to the FM and NM layer in figure 3.1a respectively. The Co/Ni ferromagnetic multilayer was in this case treated as one layer, bypassing the multilayer structure entirely. To emulate the scattering effects of the several interfaces in this multilayer a lower spin flip relaxation time than the bulk values for Co or Ni is used to model the enhanced scattering of the several interfaces. An estimation of this relaxation time was made based on the approach to Choi et Al. [70] to estimate this time in a Co/Pt multilayer system. This estimation is discussed in more detail in appendix C.

Considering the dynamic equation (3.2), all that yet needs to be defined are the boundary conditions for μ_s. In the diffusive formalism described above, the spin current density J_μ in terms of μ_s is defined as:

$$J_\mu = D\frac{\partial \mu_s}{\partial z}. \tag{3.3}$$

At the Pt/air ($z = 0$) interface, J_μ should vanish. It is assumed that the interfaces between the metallic layers are transparent to spin currents (i.e. the spin chemical potentials at the interface between two of the metallic layers is continuous), taking into account that the finite conductance of the NM/FM interface is implicitly included as the enhanced damping in the Co/Ni multilayer stack. The definition at the boundary between the Cu and NiO boundary is less trivial to define. At this interface a conversion between a spin polarized electron current to a magnon carried spin current occurs. The main mechanism for this conversion is postulated to be Umklapp reflections as illustrated in figure 3.3 [81]. In this process, a electron with a particular spin direction is annihilated, while an electron with opposite spin angular momentum is created. Furthermore, a magnon is created in the AFMI so that locally angular momentum conservation is obeyed.

Theoretical work of this kind of conversion at an interface between normal metals and FM insulators was performed by Zhang et al. [60, 61]. In this work, the spin convertance was introduced as the parameter that determined the efficiency of the conversion of spin polarized electron accumulation to magnon accumulation. It was shown that in this description J_μ across the NM/FMI interface was given by [60]:

$$J_{\mu,\mathrm{NM/FMI}} = G_{\mathrm{em}}\mu_s, \tag{3.4}$$

where G_{em} is the spin convertance. Arguments similar to the ones presented in these papers can be used to obtain an expression for the spin convertance at NM/AFMI interfaces.

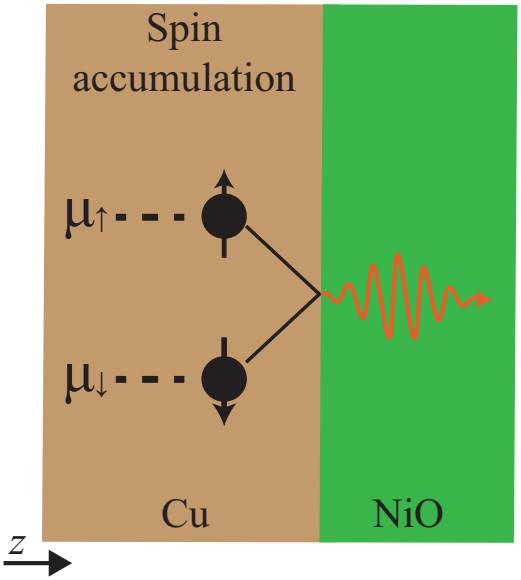

Figure 3.3: Schematic illustration of the Umklapp process that constitutes the conversion of spin accumulation into magnon accumulation at the Cu/NiO interface. A spin-down electron is annihilated, while a spin-up electron is created under the emission of a magnon with the same angular momentum as the annihilated electron.

However, since no accurate probes for several of the parameters in these theoretical predictions, like the magnon density of states, were available for this work, the spin convertance will only be used as a parameter in the numerical work presented in section 3.2. A typical value of this parameter in NiO was calculated to be $G_{\mathrm{em}} = 513$ nm/ps (see appendix C).

By combining equations (3.3) and (3.4), the resulting boundary condition for the Cu/NiO interface can be formulated:

$$\mu_{\mathrm{s,Cu/NiO}} = -\frac{D}{G_{\mathrm{em}}}\frac{\partial \mu_{\mathrm{s,Cu/NiO}}}{\partial z}. \tag{3.5}$$

The full set of boundary conditions and equations that have been solved to quantify the spin transport properties, and the values of the different parameters in the three layers can also be found in appendix C.

In essence thus, the Cu/NiO interface acts as a spin sink in this system: spin accumulation will be absorbed with an efficiency related to the value of G_{em}. In the limiting cases of $G_{\mathrm{em}} \to \infty$ and $G_{\mathrm{em}} \to 0$ the impinging spin accumulation will be completely absorbed, or completely blocked, respectively. The next step will be to link the quantitative estimates of the spin current across the Cu/NiO interface, mediated by G_{em}, to the spin dynamics of the antiferromagnetic order parameter $\boldsymbol{l}$. For this purpose it is convenient to define the spin current density along the Cu/NiO interface J_{s} (in units of A/m^2):

$$J_{\mathrm{s}} = eN_{\mathrm{Cu}}(E_{\mathrm{F}})G_{\mathrm{em}}\mu_{\mathrm{s}}, \tag{3.6}$$

where $N_{\mathrm{Cu}}(E_{\mathrm{F}})$ is the (bulk) density of states in Cu at the Fermi level. Based on the description presented above for arbitrary stack geometries J_{s} can be numerically predicted.

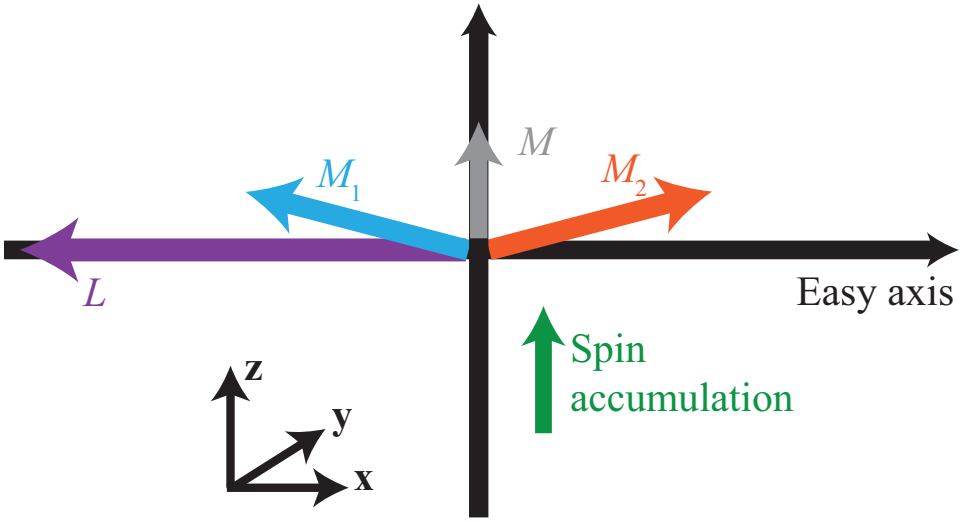

Figure 3.4: Schematic of the model system described in this section. The x-axis is the easy in-plane axis. The magnetic sublattices are shown in blue and orange. Nearby spin-accumulation polarized in the z-direction (green) will lead to a canting of both sublattices as shown in the figure. The corresponding $\boldsymbol{M}$ and $\boldsymbol{L}$ are denoted in gray and purple respectively..

The next step will be to couple this spin current at the interface to the spin dynamics of the antiferromagnetic layer.

3.1.2 Antiferromagnetic macrospin dynamics in NiO

To investigate the response of $\boldsymbol{L}$ to this absorbed spin accumulation at the NM/AFM interface, a macrospin description proposed by Cheng et al. will be employed [19].

The antiferromagnetic system and the spin accumulation by the spin current from FM layer with PMA is illustrated in figure 3.4. It is defined by two macrospin vectors in a single antiferromagnetic domain $\boldsymbol{M_1}$ and $\boldsymbol{M_2}$ that represent the sublattice magnetizations, which point in opposite directions along the x-axis in the absence of external stimuli like a spin current or an applied magnetic field. It is convenient to consider the normalized spin vectors defined as $\boldsymbol{m_1} = \boldsymbol{M_1}/M$ and $\boldsymbol{m_2} = \boldsymbol{M_2}/M$, where M is the sublattice magnetization (351 kA/m in NiO [9]). The normalized magnetization $\boldsymbol{m}$ and Neél parameter $\boldsymbol{l}$ can then also be defined as $\boldsymbol{m} = (\boldsymbol{m_1} + \boldsymbol{m_2})/2$ and $\boldsymbol{l} = (\boldsymbol{m_1} - \boldsymbol{m_2})/2$.

The spin dynamics of the antiferromagnetic order parameter, in the exchange limit ($|\boldsymbol{l}| \gg |\boldsymbol{m}|$) and neglecting effects such as spin pumping by the antiferromagnetic spins [82], is caught in the following equation [19]:

$$\boldsymbol{l} \times \left[\ddot{\boldsymbol{l}} - \omega_{\mathrm{R}}^2 l_{\mathrm{x}} \hat{\boldsymbol{x}} + 2\alpha\omega_{\mathrm{E}} \dot{\boldsymbol{l}} + 2\omega_{\mathrm{E}}\omega_{\mathrm{s}} (\hat{\boldsymbol{z}} \times \boldsymbol{l}) \right] = 0, \tag{3.7}$$

where α is the Gilbert damping coefficient, ω_{E} is the exchange field strength, $\omega_{\mathrm{R}} = \sqrt{2\omega_{\mathrm{E}}\omega_{\mathrm{a}}}$ with ω_{a} the in plane anisotropy field, and ω_s is a measure for the strength of the spin current pulse, which will be used to connect this model with the spin transport model described in section 3.1.1. ω_{s} is defined as follows [19]:

$$\omega_{\mathrm{s}} = \frac{a^3}{e\mathcal{V}} J_{\mathrm{s}} A_{\mathrm{pulse}} = \frac{a^3}{e d_{\mathrm{NiO}}} e N_{\mathrm{Cu}}(E_{\mathrm{F}}) G_{\mathrm{em}} \mu_{\mathrm{s}}. \tag{3.8}$$

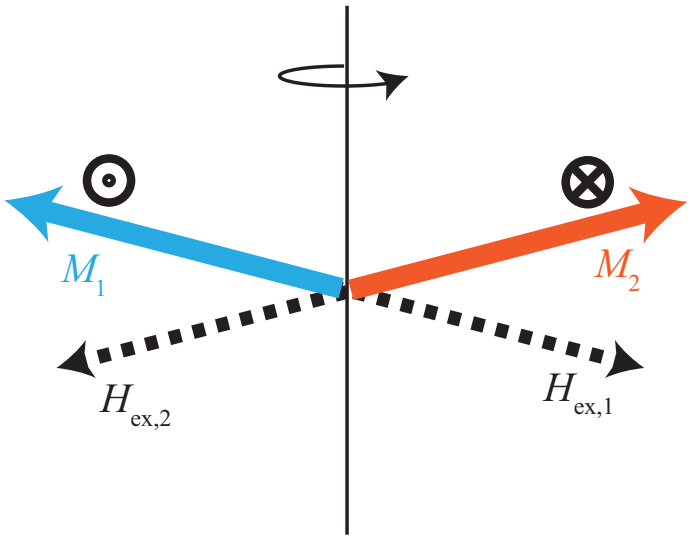

Figure 3.5: Schematic illustration of the exchange torque driven motion of the two sublattices upon OOP canting. Circles indicate rotation direction of the respective sublattice.

where a is the lattice parameter of NiO, A_{pulse} is the area of the laser pulse in which demagnetization takes place, and $\mathcal{V} = d_{\text{NiO}} A_{\text{pulse}}$ is the system volume, where it was assumed that the spin accumulation affects the whole thickness d_{NiO} of the NiO layer, which is acceptable for films with a thickness of a few nm [83].

Considering the symmetry of the system, equation (3.7) can be further simplified. Restricted by symmetry, $\boldsymbol{l}$ can only have components in the in-plane direction after the perpendicularly polarized spin current pulse, as both sublattices are affected equally. Therefore, the whole state of the antiferromagnetic order parameter can be defined by the angle $\phi(t)$ as $\boldsymbol{l} = \{l_x, l_y, 0\} = \{\cos(\phi(t)), \sin(\phi(t)), 0\}$, where ϕ is the angle between $\boldsymbol{l}$ and the easy x-axis. Using this definition in equation (3.7) yields [19]:

$$\ddot{\phi} + \frac{\omega_R^2}{2} \sin(2\phi) + 2\alpha\omega_E\dot{\phi} = 2\omega_E\omega_s(t). \tag{3.9}$$

From left tot right these terms originate from the antiferromagnetic coupling between the two sublattices, the easy axis anisotropy, the Gilbert damping and the torque exerted by the spin accumulation. The numerical values of the different parameters for NiO are presented in appendix D. In equation (3.9), particular attention should be payed to the second time derivative of ϕ; similar as in Newton's equations this leads to so called inertial spin-motion. In practice, this means that although no instantaneous change to $\boldsymbol{l}$ may be observed, the acquired momentum from a spin current or field pulse can still drive dynamics even after the initial pulse has decayed [20]. This can potentially be used to switch the magnetic state of the AFM without the need for prolonged current pulses [19].

One relevant example of this is the exchange torque driven spin dynamics of antiferromagnetically coupled systems, as can also be observed in NiO. Upon (spin current induced) canting as shown in figure 3.5, the exchange field H_{ex} generates a precessional torque on both sublattices. Depending on the magnitude of the canting, the magnetic system can build up sufficient inertia to overcome the anisotropy barrier, leading to a switch of the antiferromag-

netic order parameter to another stable state. For the model system described in this section, this phenomenon is further explored in section 3.2.2.

To summarize; both the transport model and the spin dynamics model have been defined above by equations (3.2) and (3.9) respectively. These provide a generic framework to produce quantitative estimates of the sensitivity of the response of the AFM to different parameters in the stack design and the NM/AFMI interface quality. In the end two primary parameters are left that will be varied throughout the results presented in section 3.2 below: the spin convertance G_{em} and the buffer layer thickness d_{Cu}. All other parameters are either material parameters, difficult to tune experimentally or both.

3.2 Results and discussion

In this section, the results of the numerical work based on the models presented in section 3.1 will be presented. First, the influence of the two parameters of interest, d_{Cu} and G_{em}, on the spin current across the Cu/NiO interface J_s will be investigated. The focus will be on the conceptual understanding of the observed behaviour of J_{s} as a function of G_{em} and d_{Cu}. Next, in section 3.2.2, the calculated J_{s} will then be used as input to characterize the transient magnetization induced in the AFM as well as the state of the anitferromangetic order parameter l. For all the calculations in this section the thicknesses of the Pt and Co/Ni multilayers were set to 3 nm and 2.6 nm.

3.2.1 Diffusion model

As discussed in section 3.1, in this thesis it is assumed that the spin current profile generated by optical demagnetization resembles the time derivative of the demagnetization curve. This leads to spin current profiles across the Cu/NiO interface as shown in figure 3.6. As can be seen, when d_{Cu} is small (black curve) with respect to the spin diffusion length of Cu (~100 nm [84]), the spin current strongly resembles the spin generation profile used as input (figure 3.2b). Where the sharp peak centered at Δt = 0 ps corresponds to the demagnetization, while the negative peak at Δt = 1.8 ps represents the remagnetization of the sample. In the following treatment, interest initially rests on the dependence of the magnitude of these peaks on the spacer layer thickness d_{Cu} and the spin convertance G_{em}.

Spacer layer thickness dependence

As d_{Cu} is increased in figure 3.6, three distinct effects can be distinguished. First of all, the two principal peak positions have been shifted, this is caused by the finite time it takes for the spin current pulse to travel through the thick Cu layer. Furthermore, due to the longer traveling distance, J_{s} will be more strongly attenuated. Finally due to back diffusion of spin polarized electrons, a broadening of both peaks can be observed, even leading to a disappearance of the negative peak in the profile for d_{cu} = 200 nm.

To quantify the observed attenuation of J_{s}, the values of the two principal peaks in J_{s} are calculated as a function of d_{Cu}. Figure 3.7a shows J_{s} as a function of d_{Cu} for G_{em} = 5000 nm/ps. The magnitude of the spin current decays continuously and can be separated in two regions. J_{s} decays exponentially for large values ($\gtrapprox$ 50 nm) of d_{Cu} with a decay length of 135 nm. On the other hand, for low values of d_{Cu} ($\lessapprox$ 30 nm), a $J_{\mathrm{s}} \propto 1/d_{\mathrm{Cu}}$ relation is found to fit

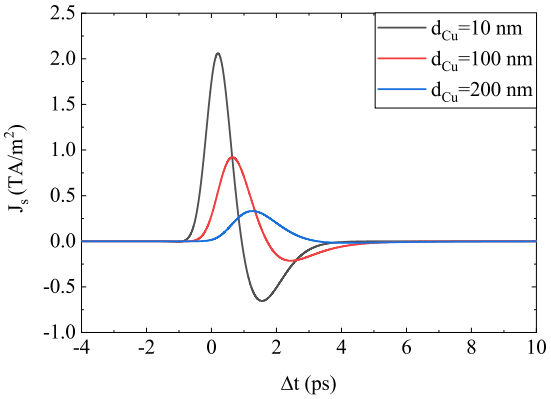

Figure 3.6: Calculated spin current across the Cu/NiO interface as a function of the delay Δt after the arrival of the demagnetizing laser pulse. Profiles for different Cu layer thicknesses of 10 (black), 100 (red), and 200 (blue) nm are shown for G_{em} = 5000 nm/ps.

the peak heights well. The two different decay regimes can be understood by considering the two different mechanisms by which spin angular momentum can be lost.

First of all, throughout all metallic layers spin decay takes place mediated by spin relaxation time τ of each specific layer. For thick Cu layers, J_{s} is dominated by the spin pulse traveling through the Cu layer, leading to exponential decay with a typical decay length in the order of 100 nm, characteristic of Cu [84]. Elseways, for low values of d_{Cu} enhanced decay of J_{s} can be observed. This has two primary causes: back-diffusion of non-converted spin accumulation into the low τ Pt and Co/Ni layers, and the high conversion efficiency of the Cu/NiO interface leading to efficient conversion of spin angular momentum at the interface. Finally it should be noted that the maximum J_s caps of for $G_{\mathrm{em}} \rightarrow \infty$, due to the limited generation of spin accumulation due to demagnetization.

This interpretation is also reflected when considering the d_{Cu}-dependence of J_{s} for different values for the spin convertance, as shown in figure 3.7b. It can be seen from this picture that, as G_{em} decreases, the region of fast decay becomes less significant at low d_{Cu}; indicating the transition from spin momentum loss dominated by spin conversion across the NM/AFM interface, to it being dominated by spin flip relaxation in the metallic layers.

Spin convertance dependence

A similar analysis was performed to find the dependence of J_{s} on the spin convertance G_{em}. Figure 3.8a shows this dependence for a stack with d_{Cu}=5 nm. As expected, the peak magnitudes increase with increasing G_{em}, in line with the interpretation of G_{em} being the efficiency with which spin current can be absorbed. When the same curve is considered for different d_{Cu} (figure 3.8b), two distinct trends can be observed. The maximum transmitted J_{s} across the Cu/NiO interface decays monotonically with d_{Cu}, which is in line with the behaviour of J_{s} as a function of d_{Cu} presented in figure 3.7b.

More interestingly, it can be observed that as d_{Cu} increases, the thickness at which J_s does not increase appreciably anymore goes down. This is explained as follows. As the spin convertance goes down, μ_{s} becomes larger at the interface, leading again to back-diffusion to the Pt and Co/Ni layers where the spin relaxation time is much shorter than in the Cu layer. As G_{em} becomes large enough though, the efficient spin transfer across the interface

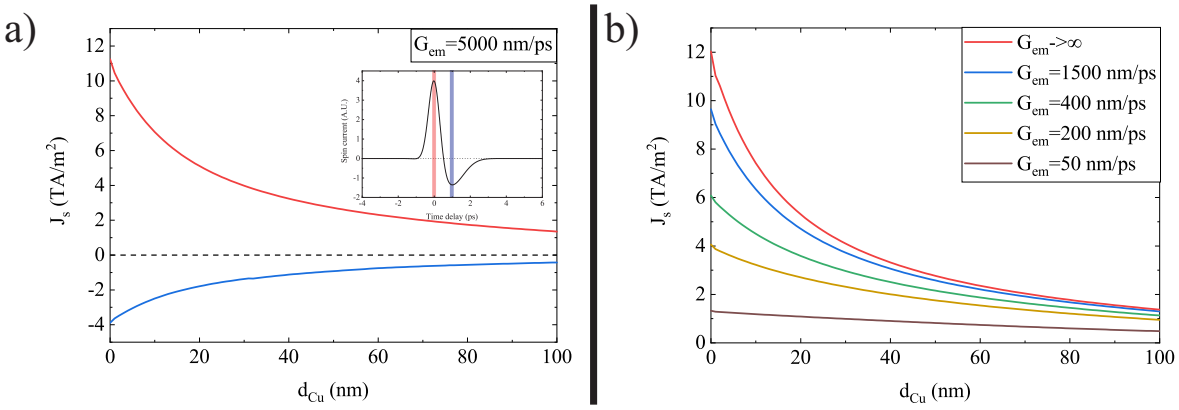

Figure 3.7: a): Magnitude of the maximum (red) and minimum (blue) in the spin current across the Cu/NiO interface J_s as a function of d_{Cu} for G_{em}=5000 nm/ps. b): Magnitude of the maximum in J_s as a function of d_{Cu} for different values of G_{em}.

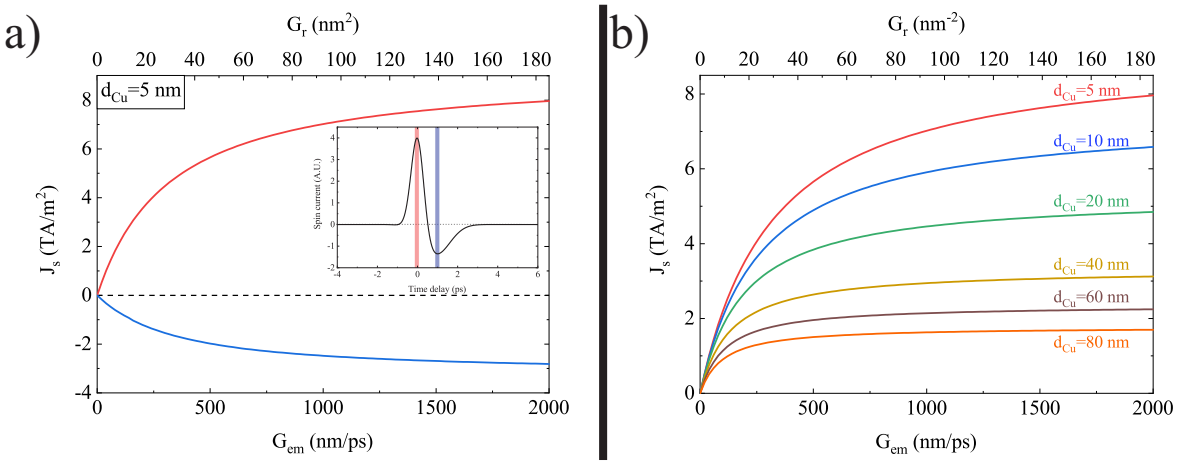

Figure 3.8: a): Magnitude of the maximum (red) and minimum (blue) in the spin current across the Cu/NiO interface J_s as a function of G_{em} for d_{Cu}=5 nm. b): Magnitude of the maximum in J_s as a function of G_{em} for different values of d_{cu}. In this figure the top x-axis shows the real part of the spin mixing conductance (see appendix C.3)

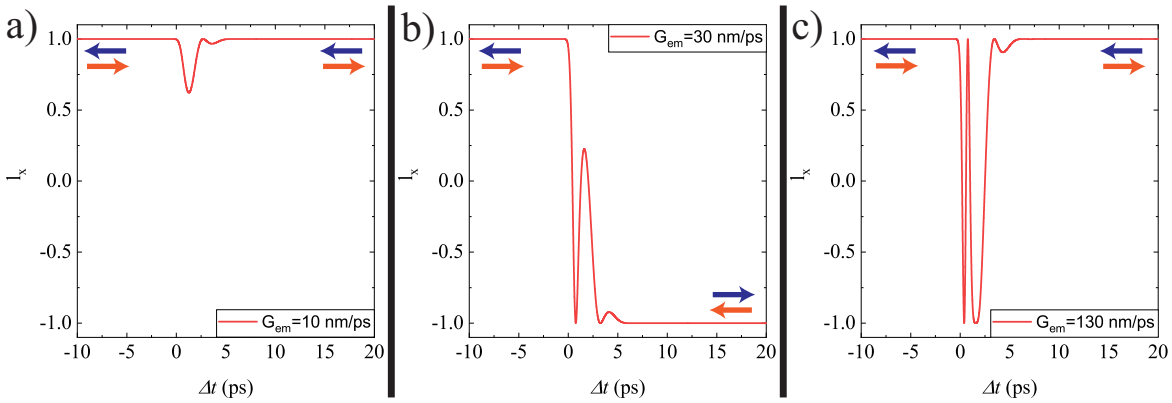

Figure 3.9: Time dependence of the x-component of the Neél parameter l_x for d_{Cu}= 20 nm and a): G_{em} = 10 nm/ps, b): G_{em} = 30 nm/ps, and c): G_{em} = 130 nm/ps.

prevents the appearance of a large spin accumulation there and by extension the importance of back-diffusion into the low-τ layers.

As G_{em} can vary with a factor of two depending on interface quality [85], it is noted that J_s can be tuned by up to 20% given d_{Cu} = 10 nm. This suggests that in real experiments interface quality is something that can strongly influence the absorbed spin current. In the end, the most important take-away message from these calculations is that for the thicknesses typical for optical spin current experiments (4-20 nm), the critical parameter is the Cu/NiO interface quality represented by G_{em} in the current model. The next step will be to see how the magnitude of J_s translates to the maximum induced OOP magnetization m_z and the end configuration of the component of the antiferromagnetic order parameter along the easy x-axis $l_{x,e}$.

3.2.2 Spin dynamics

As was discussed in section 3.1.2, when both sublattices are canted in the z-direction exchange torques lead to a rotation of $\boldsymbol{l}$ around the same canting axis (see figure 3.5). This behaviour is recovered from the model and illustrated in figure 3.9. Here, l_x is shown as a function of the delay after laser excitation Δt. This response is shown for d_{Cu} = 20 nm and G_{em} = 10, 30 and 130 nm/ps in figure 3.9a, 3.9b and 3.9c respectively.

Before the arrival of the spin current pulse, $\boldsymbol{l}$ points in the positive x-direction (+x), one of the equilibrium configurations along with the negative x-direction (-x). In figure 3.9a, the spin current is insufficiently large to provide the inertia needed to bring $\boldsymbol{l}$ from the +x to the -x state. When the spin current pulse is then increased, as shown in figure 3.9b and 3.9c, $l_{x,e}$ will alternate between the +x and -x end states.

To further illustrate this point, a phase diagram of $l_{x,e}$ as a function of d_{Cu} and G_{em} is shown in figure 3.10a. The alternating behaviour between the two different end states is again observed. Since the spin current across the Cu/NiO interface is proportional to G_{em} in this description, the phase boundaries behave similarly to the J_s curves shown in figure 3.8b.

It is instructive to compare the phase diagram to the dependence of $m_{z,max}$ on d_{Cu} and G_{em}, as shown in figure 3.10b. It is found that $m_z(\Delta t)$ follows the short optical spin current pulse adiabatically (i.e. closely following the spin current pulse). Upon comparison, the phase boundaries in figure 3.10a, closely follow lines of equal $m_{z,max}$ in 3.10b; further supporting the

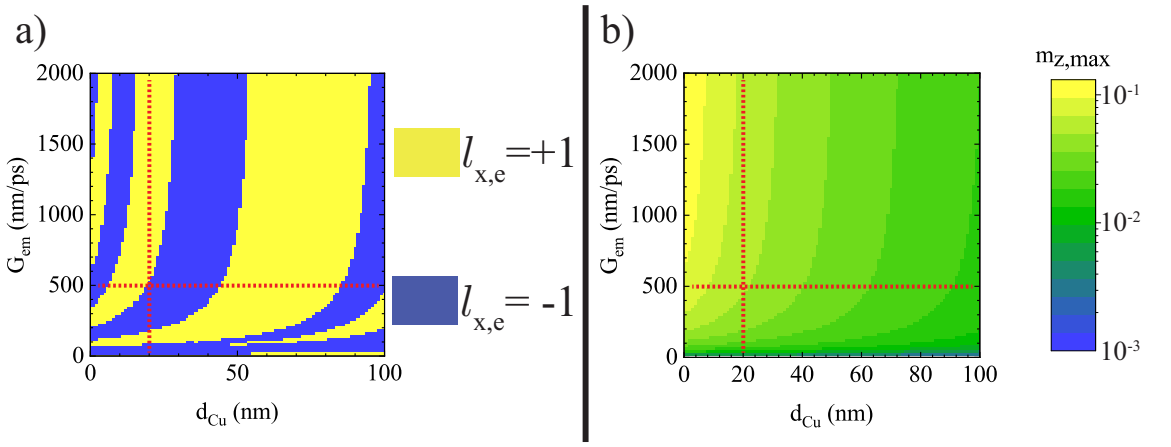

Figure 3.10: Mapping of the end configuration of the Neél parameter $l_{\mathrm{x,e}}$ (a) and the maximum of the OOP component of the magnetization $m_{\mathrm{z,max}}$ (b) as a function of d_{Cu} and G_{em}. Note that the discretization of the scale bar only serves to illustrate similarities between a and b; the calculated values of m_{z} are continuous. Red dotted lines indicate the typical parameter values of d_{Cu} = 20 nm and G_{em} = 500 nm/ps.

notion that the J_{s}, $m_{\mathrm{z,max}}$ and the end state of the AFM are strongly intertwined.

Also, $m_{\mathrm{z,max}}$ is found not to exceed 0.1, suggesting that the exchange approximation is a reasonable one for the described system. More importantly though, the induced OOP canting should indeed be optically measurable, as even for typical values of G_{em} = 500 nm/ps and d_{Cu} = 20 nm, m_{z} is still found to be close to 0.01 corresponding to a maximum tilt of 0.5 degrees of the sublattice magnetizations. This in turn corresponds to a Faraday rotation angle $\theta_{\mathrm{F}} =\sim 0.1-1$ µrad, given a Faraday rotation of ~ 0.04 µrad/nm at a laser wavelength of 800 nm [18], which should in principle be detectable through Faraday rotation measurements [34, 86]. This suggests that, provided the region affected by the spin current pulse is is in a monodomain state and $\boldsymbol{l}$ is coherently excited, the transient magnetization is detectable, which is pivotal for the optical measurements presented in chapter 5.

Finally, in figure 3.11, we present again the two kinds of phase diagrams earlier presented in figure 3.10, but for different value of the damping parameter α. It should become immediately clear that the magnitude of J_{s} needed to make $\boldsymbol{l}$ cross the anisotropy barrier decreases upon decreasing the damping. What is important to note here, is that the damping due to spin pumping may lead to an additional term of order 0.001 to the overall damping [82]. Neglect of this term in the spin dynamics is hence too crude an approximation, and should be taken into account in future descriptions of this system.

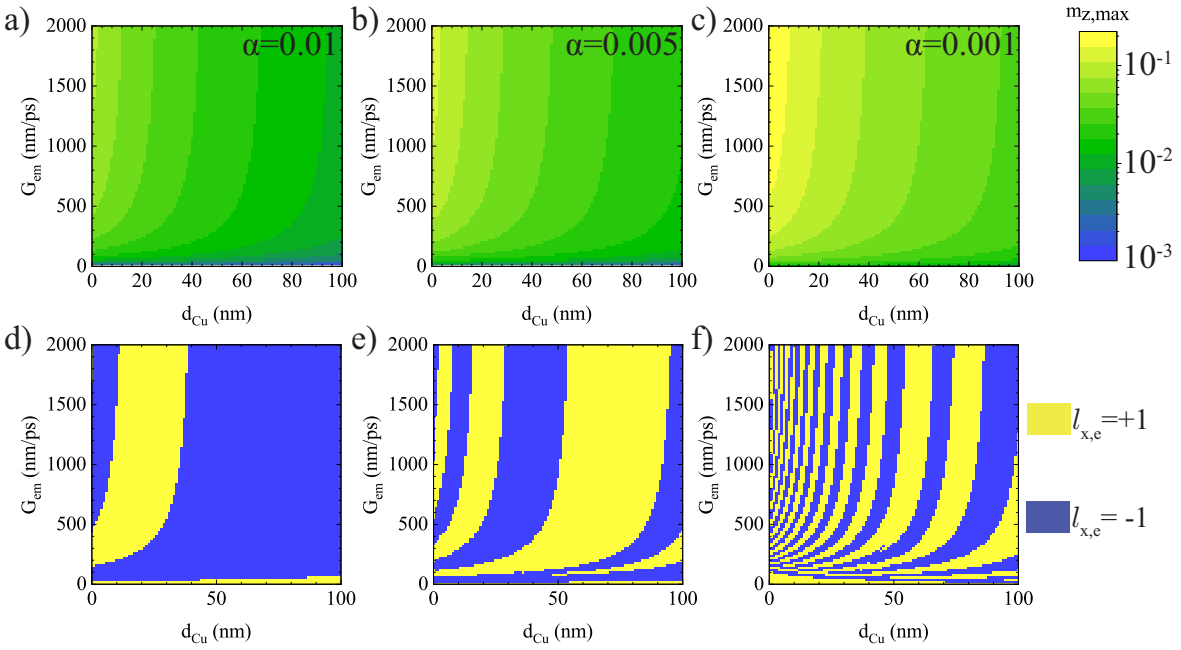

Figure 3.11: Maximum out of plane component of the OOP magnetization $m_{\mathrm{z,max}}$ (top) and the end configuration of the Neél parameter $l_{\mathrm{x,e}}$ (bottom) as a function of d_{Cu} and G_{em} for α = 0.01 (a,d), α = 0.005 (b,e) and α = 0.001 (c,f). Note that the α = 0.001 situation is not physically realistic and only serves as an illustration of the behaviour of the model. Red dashed lines prepresent typical values of G_{em} and d_{Cu}

3.3 Conclusion

In this chapter a generic framework for spin transport and dynamics after ultrafast optical demagnetization has been presented. Given realistic parameters for a $Pt/[Co/Ni]_3/Cu/NiO$ multilayer system, the model has provided numerical estimates for relevant parameters in the optical experiments described in chapter 5, such as the induced transient magnetization. As the most important result, these estimates suggest that the canting of the sublattices upon optical spin current pulse absorption should be sufficient to be measurable in Faraday rotation measurements on thin films of NiO. The next step will be to validate this description of the spin dynamics and transport. One attempt to check the validity is presented in chapter 5, where the exact stacks for which the numerical work in this chapter was performed are investigated with these optical spin current pulses.

An alternative way to test the validity is to consider a system where the AFM is replaced by an IP polarized FM. Then the response of this IP layer to an OOP polarized spin current can be studied (see e.g. [35]). Since the electron-magnon spin convertance G_{em} can be related to the spin mixing conductance, the spin transport description from section 3.1.1 may also be applied to these kind of ferromagnetic systems. In FMs, the magnetic structure is less sensitive to sample anomalies like strain and temperature effects and are more easily characterized with e.g. the FE, which are some of the reasons that their behaviour after current pulse excitaiton is well charted out.

Chapter 4

Sample growth and characterization

In this chapter the techniques used to grow and characterize the magnetic multilayer stacks are presented. These are used in the optical measurements presented in chapter 5. There are two main kinds of samples that were investigated in this work in accordance with the two research questions posed in the introduction to this thesis.

The first stack is shown in figure 4.1a. This sample was grown to directly investigate transient magnetization dynamics in NiO. Commercial crystalline MgO substrates were used with [001] [87] and [111] [88] growth directions. This substrate is used due to the excellent lattice matching between NiO and MgO; These materials have a lattice parameter of 4.176 Å [89] and 4.213 Å [90] respectively, implying a lattice mismatch of 0.9%. It will be shown below that textured thin films of NiO with the same crystal structure as the MgO substrate can be grown by sputtering. A Cu buffer layer is then included to magnetically isolate the NiO from the FM layer. Next, alternating layers of Co and Ni were grown. The surface anisotropy in these ultrathin layers gives rise to perpendicular magnetic anisotropy (PMA), related to the symmetry breaking and precise orbital overlap between the different material layers [91, 92]. Co/Ni multilayers were chosen for this purpose for their high saturation magnetization (1.3 MA/m) and spin current generation [77]. Finally a Pt capping layer is grown to prevent the magnetic layers from oxidising, as Pt is well known to be highly resistant to oxidation under ambient conditions [93].

The other stack (figure 4.1b) is intended for experiments to test the magnonic spin transport through NiO. The main difference is that a 5 nm Co layer is included between the NiO and the MgO substrate. The 5 nm Co layer is expected to have IP anisotropy based on shape anisotropy [37]. A thin NiO layer is then expected to function as a transport layer for optical spin currents. The rest of the stack is identical to the one shown in figure 4.1a, having a Cu buffer layer, a Co/Ni FM multilayer with PMA and a Pt capping layer.

This chapter will consist of two primary section. Firstly, section 4.1 describes the primary stack fabrication and characterization tools and the physical principles these rest on. Subsequently, the results from these different growth and characterization steps are presented in section 4.2.

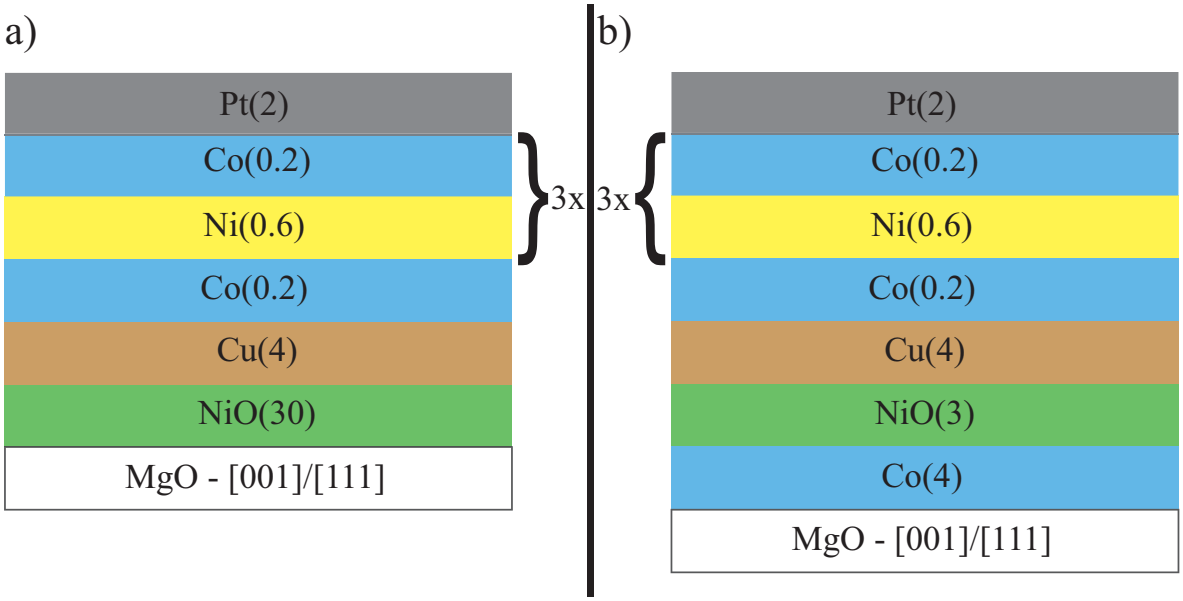

Figure 4.1: Schematic of the multilayer systems that were investigated in this work. Numbers between parentheses are layer thicknesses in nm. a): Multilayer stack grown for investigation of transient magnetization dynamics in NiO. b): Multilayer stack grown for investigation of spin transport by antiferromagnetic magnons.

4.1 Experimental methodology

In this section, the experimental techniques used for sample fabrication and characterization of the two different stacks will be introduced. Sputter deposition was used as the primary method of sample growth and will be introduced in section 4.1.1. Particular attention will be paid to reactive sputtering, which was employed for the growth of NiO. To check whether samples had the correct stoichometry and crystallinity, X-ray photoelectron spectroscopy (XPS), low-energy electron diffraction (LEED), and X-ray diffraction (XRD) were performed. These three experimental tools will be described in the subsequent subsections 4.1.2, 4.1.3, and 4.1.4 respectively. Finally, the main method of characterizing the ferromagnetic part of the multilayer, the magneto optical Kerr effect (MOKE), will be introduced in section 4.1.5. Some more sparsely used experimental techniques like vibrating sample magnetometry (VSM) and Raman spectroscopy will be briefly introduced in the results section of this chapter.

4.1.1 Sputter deposition

Sputtering is a fabrication method which allows for the deposition of thin layers of a target material on a sample. Sputtering takes place in a vacuum chamber with low-pressure ($\mathcal{O}\{10^{-2}$ mBar$\}$), high-purity gas. Noble gases are typically used for this purpose due to their low reactivity. While it is known that heavier atom species provide a higher sputtering rate [94], Argon is used. The reason for this is that heavier noble gases are either radioactive (Ra) or expensive (Kr,Xe).

A sketch of a typical sputtering chamber is shown in figure 4.2a. In this illustration the three parameters p, d and P represent the Argon pressure during the sputtering process,

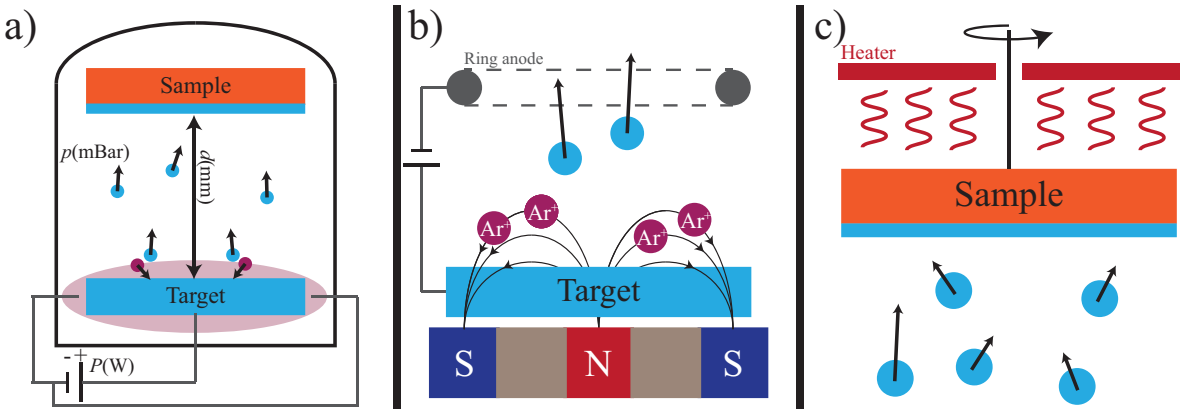

Figure 4.2: Schematic of the workings of magnetron sputter deposition showing: a): The full chamber, b): A close-up of the area around the target, c): A close-up of the area around the sample.

the distance between the target and the sample and the power used to maintain the plasma respectively. An Ar plasma (purple in figure 4.2a) is ignited around a target material. This target is typically a high purity disk of a pure metal, alloy or insulator. The high energy particles in the plasma are capable of overcoming the binding energy of the atoms at the surface of the target, effectively separating atoms from the target. The ejected atoms travel through the chamber towards the sample. As the target atoms arrive at the substrate the atom will diffusively move around said substrate depending on the nature (e.g. surface morphology or crystal facet [95–97]) and temperature of the substrate [94]. At some point atoms start moving together on the substrate, making re-evaporation less likely. These nucleating islands will then grow until they become so big that they coalesce. This process of island formation, growth and coalescence continues until continuity is reached. By calibrating the growth rate for the specific sample and reactor conditions, deposition of layers of well-defined thickness with accuracy up to 1 Å is possible [98]. This technique is also widely used to make coatings for its scalability.

Figure 4.2b shows a close-up of the region around the target. The plasma is ignited by applying a voltage difference between the target material and a conductive coil (ring anode) near the sample. An applied magnetic field is used to confine the plasma and target radicals as well as secondary electrons to the region around the target. This in turn leads to a more dense plasma around the target material. An important consequence is that the plasma can be maintained at lower operating pressures and powers [99], which is particularly relevant for the experiments described in section 4.2.3. By using different targets one can accurately engineer different ultrathin multilayer stacks which is a centerpiece of current day spintronic research (e.g [25, 100–102]). It is also possible to deposit compounds of the target material through reactive sputtering. In this case another gas beside Ar is introduced into the chamber near the sample (e.g. O_2, N_2) which allows for the growth of e.g. oxides or nitrides [103, 104].

Finally, different mechanisms to manipulate and/or improve the sputtering process are shown in figure 4.2c; this figure shows the region around the sample. It is common practice to rotate the sample around its normal to improve film homogeneity. In this work a heating module was also used to heat the substrate, which is critical for the growth of several crystalline films [105, 106].

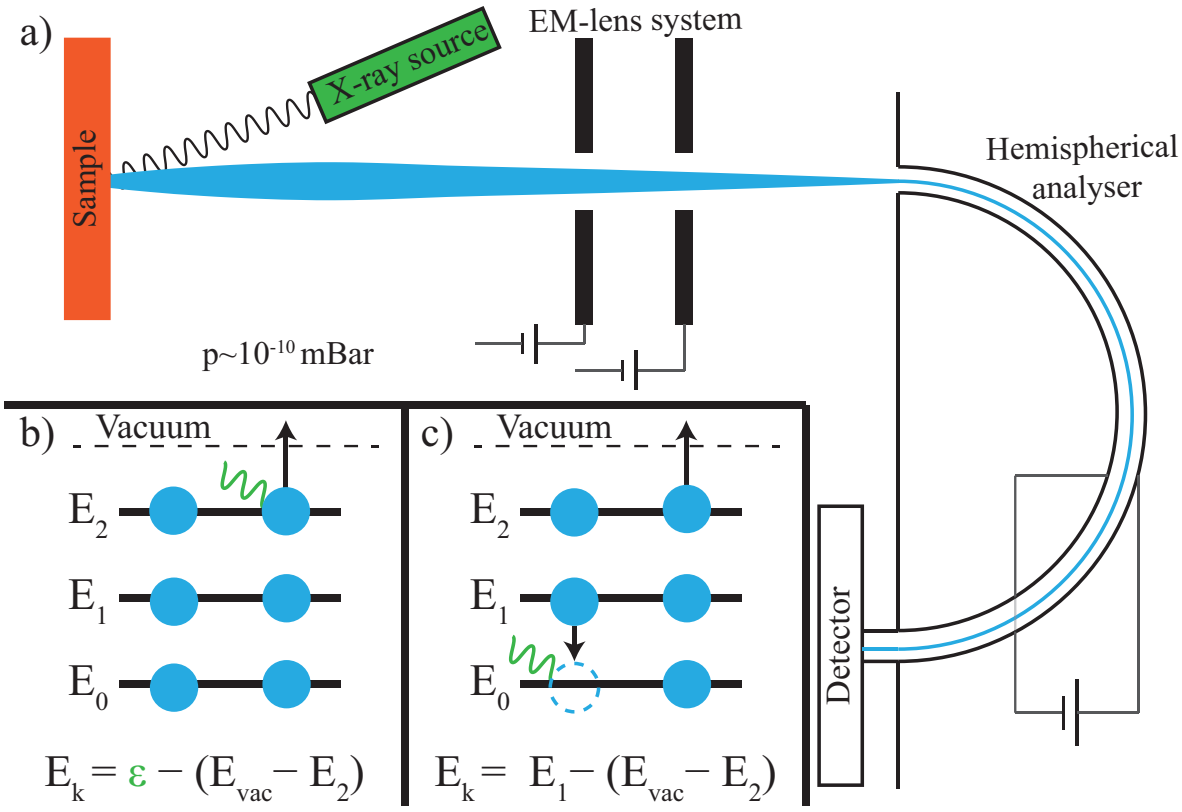

Figure 4.3: Basics of XPS: a): Illustration of a typical XPS setup. b): Illustration of the photoelectron mechanism for electron ejection. c): Illustration of the Auger mechanism for electron ejection.

4.1.2 X-ray photo-electron spectroscopy

To test whether a sputtered sample has the right composition, a probe for the deposited atoms and compounds is required. XPS is a spectroscopic technique used at ultra-high vacuum (UHV) that probes the elemental composition of the investigated sample. It relies on the specific energy that is associated with ejecting electrons from their atomic orbitals. High energy x-rays eject electrons from their respective orbitals at the surface of the sample. The kinetic energy after ejection is thus dependent on the specific energy associated of the electronic orbitals of the probed sample, making the XPS spectrum a fingerprint of the material under investigation.

An illustration of an XPS measurement setup is shown in figure 4.3a. The sample is bombarded with x-rays from an Al source. The emitted x-rays ionise electrons from the sample material. The ionized electrons are accelerated towards the hemispherical analyser and focused by an electromagnetic (EM) lens system. The hemispherical analyser consists of two hemispheres of radii 75 and 125 mm respectively. By electrically biasing the two hemispheres with respect to each other, only electrons with a specific pass energy E_p are detected. The pass energy E_p is defined as:

$$E_\mathrm{p} = -q \cdot k \cdot \Delta V, \tag{4.1}$$

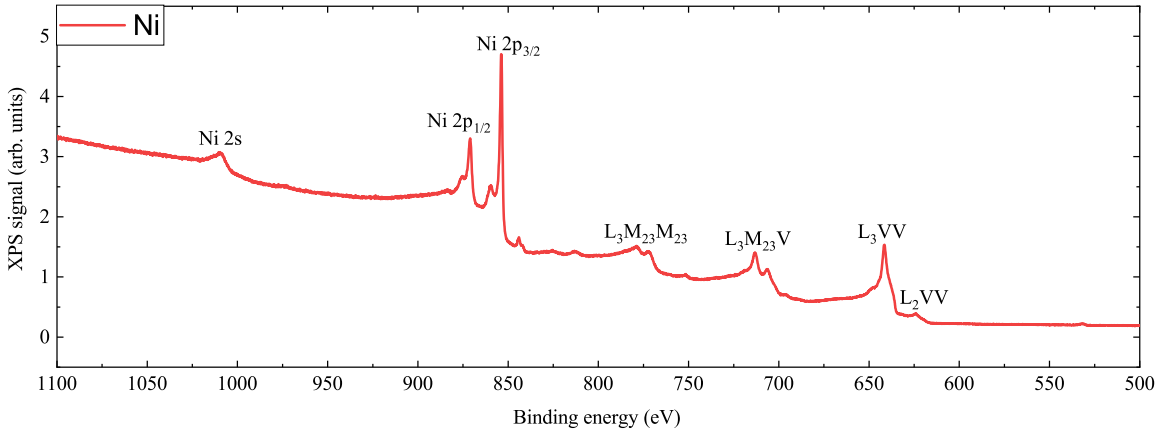

Figure 4.4: Typical XPS-spectra for metallic Ni. Primary peaks photoelectron and Auger peaks are labeled.

Electrons with kinetic energy higher than E_p will collide with the outer hemisphere, while electrons with a lower energy collide with the inner hemisphere. Thus, by tuning ΔV, it is possible to selectively probe electrons with a specific kinetic energy. It should be noted that due to the limited mean free path of the ionized electrons the probe depth of XPS is limited to the first few nm; A property that makes XPS suitable for thin film and surface characterization studies.

The XPS-spectrum gives a fingerprint of the energy levels of the atoms in the sample, and by comparing the spectra to known reference spectra it is possible to obtain qualitative and quantitative information about the presence of atomic species, their stoichometry and the presence of compounds. In the analysis of XPS spectra it is important to distinguish between two different ionization mechanisms: photoelectron emission and Auger emission. Figure 4.3b shows a cartoon photoelectron emission. The energy of an x-ray photon (green) is transferred to one of the electrons in the material. This electron is subsequently excited to the vacuum level after which it enters the measurement scheme shown in figure 4.3a. The kinetic energy of the emitted electron E_k is then defined as the difference between ϵ and the energy needed to eject the electron from its orbital to the vacuum.

The Auger excitation mechanism is shown in figure 4.3c. It occurs when an electron moves to a vacant energy level with lower energy ($\mathrm{E}_1 \rightarrow E_0$ in figure 4.3c). The excess energy is transferred to an electron in a higher orbital (E_2 in figure 4.3c), which can lead to ionization. One important consequence is that E_k in this case no longer depends on the initial x-ray energy, but on the energy difference between the vacant level and the initial state of the electron that decayed to a lower energy state.

XPS was used as a tool to check the quality of the deposited NiO films, as past research has shown XPS to be an effective probe for the surface chemistry of these transition metal oxides and hydroxides [107–109]. Figure 4.4 shows a typical full energy spectrum on which photoelectron and Auger transitions for Ni are observed. A wide variety of peaks can generally be explained based on the two basic types of transitions shown in figures 4.3b and 4.3c [110]. When labeling the different peaks in the XPS spectrum figure 4.4, regular naming conventions were used. For a photoelectron emission process, labels like Ni2s were used, referring to the atomic species and the associated orbital from which the electron was ejected. For Auger-

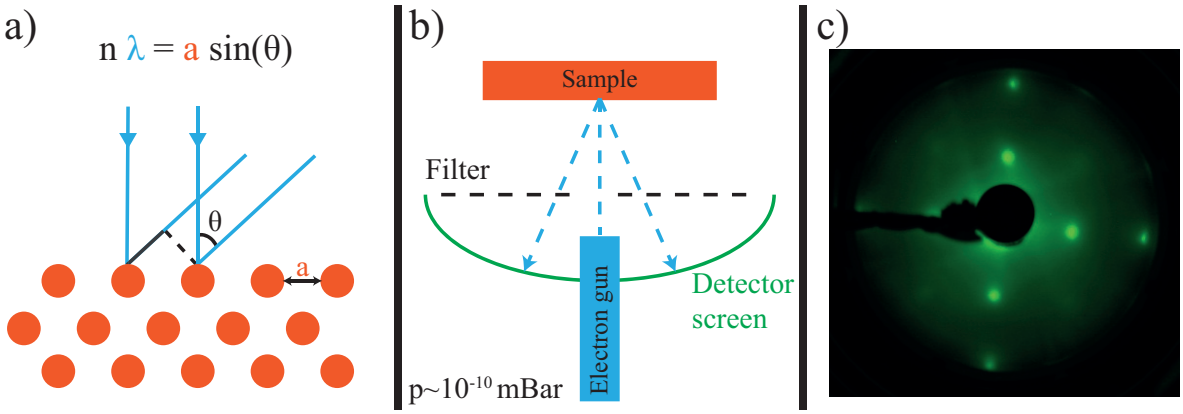

Figure 4.5: Basics of LEED: a): Bragg condition for scattering of low energy electrons off the first few layers of atoms. b): Schematic of the experimental setup used to measure a LEED diffraction pattern. c): LEED-spectrum measured on a [001]-MgO substrate. Note the square diffraction pattern as expected for the [001]-facet of materials that crystallize in a rock salt structure [116, 117].

processes (figure 4.4c), labeled by e.g. $L_3M_{23}M_{23}$, the three letters and suffices refer to the initial states of the electron excited by the photoelectric effect, the initial state of the electron decaying to the lower energy vacant orbital, and the electron ejected by the excess energy of the decay process [111]. In section 4.2.1 particular focus will be put on the 2p photoelectron peaks around 870 eV for the comparison between Ni and NiO.

4.1.3 Low-energy electron diffraction

Besides composition, another important parameter in the magnetic stack fabrication is crystallinity, particularly of the samples where lattice matching growth of NiO on MgO is required. Qualitative and quantitative information about the crystal structure can be obtained through low-energy electron diffraction (LEED). This technique was first used by Davisson et al. to show the wave-nature of electrons [112] and has since then been used as a surface probe for single crystals [113, 114]. A LEED experiment revolves around a beam of low energy (20-500 eV) electrons of well defined energy impinging on some (crystalline) sample. The beam will be diffracted based on the crystal structure of the sample within the first few monolayers due to the low mean free path of low energy electrons [115]. This process is a form of Bragg scattering, where constructive interference between the waves scattered off different atomic cores (in the case of LEED) leads to sharp diffraction peaks for crystalline samples following Braggs law:

$$n\lambda = a \sin\theta, \tag{4.2}$$

where a is the lattice parameter, θ is the angle between the scattered beam and the surface normal, n is an integer and λ the wavelength of the electrons. A cartoon of Bragg's condition is shown in figure 4.5a.

The electron wavelength can subsequently be derived by using the De Broglie relation between the electron momentum p_e and λ:

$$\lambda = \frac{h}{p_e} = \frac{h}{\sqrt{2meV_{\text{acc}}}}, \tag{4.3}$$

where m is the electron mass and V_{acc} the accelerating voltage used to create the electron beam. A cartoon of the LEED setup that was used during this research is shown in figure 4.5b. At UHV (10^{-10} mBar was routinely reached) a tungsten hot filament was used as an electron source for the beam which at focus provides spot sizes of order 300 µm. The ejected electrons are accelerated by an applied voltage V_{acc} and are scattered by the sample surface leading to a diffraction pattern governed by Bragg's law (equation (4.2)). The scattered electrons pass through an energy filter grid which only allows electrons which scattered elastically to pass through.

The elastically scattered electrons finally collide with a fluorescent screen leading to a pattern as shown in figure 4.5c. This pattern can be visualised with a camera. The figure shows the LEED pattern produced by a clean crystalline [001]-MgO substrate. Since the diffraction pattern is a fingerprint of the reciprocal space of the crystal (see e.g. [118]), the square lattice of the [001]-facet of MgO is expected to show a square diffraction pattern, which it does.

4.1.4 X-ray diffraction

In order to get in-depth quantifiable information of the crystal structure of the grown films, films are removed from the UHV environment in which the previously mentioned measurements and growth took place to perform XRD. XRD is spectroscopic technique which makes use of the wave character of x-ray radiation to produce a diffraction pattern based on the sample crystal structure. There are a few important distinctions between XRD and LEED. Firstly, X-rays penetrate much deeper into the sample than low-energy electrons. In practice, this means that the full depth of the sample as shown in figure 4.1 can be investigated. Furthermore, since X-rays are reflected off the lattice planes the Bragg condition for constructive interference needs to be altered slightly:

$$2d \sin\theta = n\lambda, \tag{4.4}$$

where now d is the lattice plane spacing, and θ is the angle between the X-ray-beam and the sample plane. The Bragg condition for XRD is shown schematically in figure 4.6a.

In an XRD measurement generally the angle θ is varied over an angular region of interest. Diffraction peaks are observed when the Bragg condition is obeyed. Figure 4.6b shows two characteristic XRD peaks measured on as-received crystalline MgO substrates. Due to the difference in lattice spacing d between the two growth directions, the Bragg condition is thus obeyed at higher θ for the [001]-crystal. The peak-splitting that can be observed is caused by the non-monochromaticity of the Cu x-ray source ($\lambda = 1.54$Å). Spectra as shown in figure 4.6b carry information about the materials present in the grown sample and, more critical to this work, the crystal structure of said material.

One important property used to gain insight in the crystal structure on the nanoscale and the way different crystal facets stack up in the material is the crystallite size. Crystalline materials do not consist of one sample-spanning crystal, but rather of several crystallites. These crystallites are regions with a well defined crystal structures and are separated in the simplest image separated by regions of amorphous materials. To quantify crystallite sizes d from diffractograms, the Scherrer equation can be used [119, 120]:

$$d = \frac{K\lambda}{w\cos(\theta)_{\text{c}}}, \tag{4.5}$$

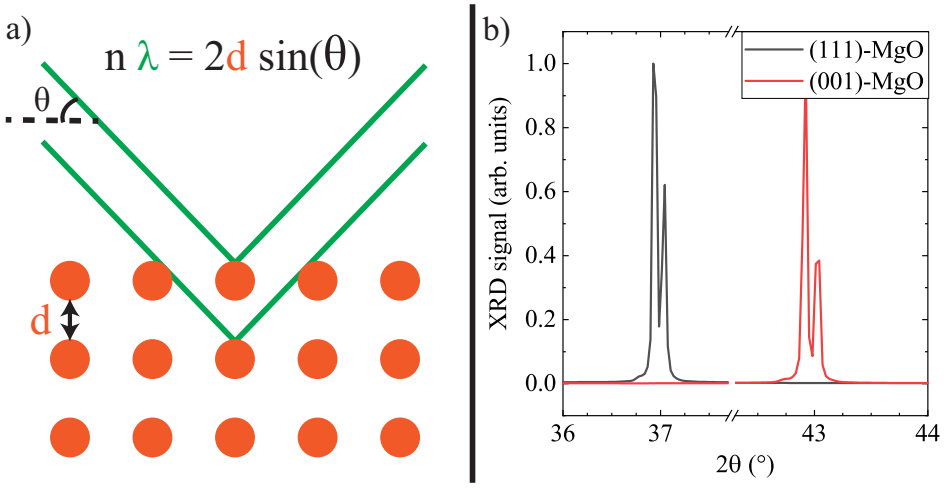

Figure 4.6: Basics of XRD. a): Illustration of the Bragg condition for constructive interference of x-rays with wavelength λ incident on a material with lattice plane spacing d. b): [111]-and [001] XRD peaks measured for as-received crystalline MgO substrates.

where K is a shape factor of the crystallites, λ is the X-ray radiation's wavelength, w is the peaks FWHM and $(2\theta)_c$ is the peak position. Since in this project no direct probe for visualization of these crystallites was used, an approximation of spherical crystallites in crystal with cubic symmetry will be used in this work. In this case the form factor is $K = 0.94$ [121].

For the analysis presented in the results section of this chapter, it is also important to recognize the influence of strain on the width and position of diffraction peaks. Figure 4.7 shows the simplest strain dependencies of peak position and width. Suppose a material which has a bulk lattice spacing d_0 and hence, according to equation (4.4), a diffraction peak at a characteristic angle θ_0 (figure 4.7a). Note that even for a material with perfectly uniform lattice spacing, a finite width is found due to instrumental line broadening. If a uniform tensile or compressive strain is exerted on the material in the stacking direction this leads to a shift of the diffraction peak to higher and lower angles respectively (figure 4.7b). Contrarily, the presence of a non-uniform strain leads to a broadening of the diffraction peak. This can be understood as an effect of the smearing out of the lattice spacing. This sort of broadening can e.g. be caused by strain effects between different lattice mismatched materials relaxing along the growth direction.

4.1.5 Magneto-optic Kerr effect

Finally, to characterize the magnetic properties of the ferromagnetic layers that are deposited MOKE measurements have been performed. A typical setup for these experiments is shown schematically in figure 4.8. Light from a continuous wave laser source is linearly polarized by a polarizer "P". The beam is then focused onto the sample and will, pick up a polarization rotation and ellipticity proportional to the out-of-plane component of the magnetization in the sample, as discussed in section 2.4. This change in polarization angle and ellipticity can be quantified by sending the reflected beam through another polarizer referred to as the analyzer "A". A photodetector is then used to convert the beam intensity to a usable signal. To improve the signal-to-noise ratio in this measurement, a photoelastic modulator

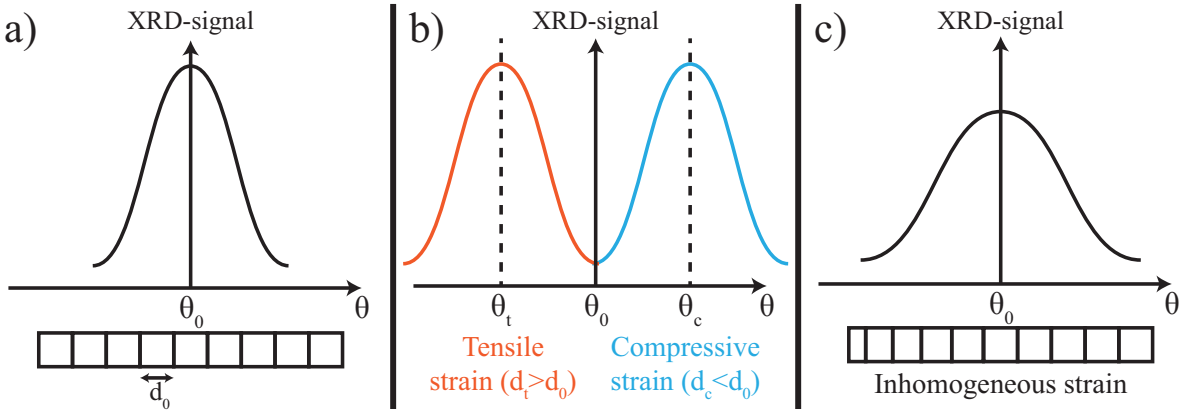

Figure 4.7: a): Illustration of the XRD-signal of a crystalline material with uniform lattice plane spacing d_0. b): Illustration of the XRD-signal of the material from a) under uniform tensile (orange) or compressive (blue) strain. c): Illustration of the broadening of the diffraction peak as a consequence of inhomogeneous strain.

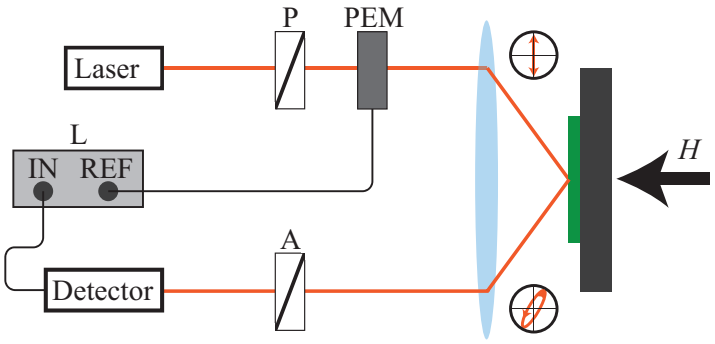

Figure 4.8: Schematic of the MOKE setup. The polarization of the light after the polarizer (P) and after the sample (in green) are illustrated in the top and bottom circles respectively. Legend: P = polarizer, PEM = photo-elastic modulator, A = analyser, L= lock-in amplifier.

(PEM) is introduced after P. The PEM modulates the polarization state of the beam at a fixed frequency. By locking in on this reference frequency the detector signal quality can be drastically improved. By then measuring this locked-in signal and sweeping an external magnetic field H at the sample location, magnetic hysteresis loops can be obtained. These loops are used in section 4.2.2 to characterize the magnetic properties of the sputtered Co/Ni multilayers.

4.2 Results and discussion

In this section, the sample growth process and associated experiments are described. Section 4.2.1 describes the characterisation of the AFM layer using XPS, VSM, Raman spectroscopy and XRD. The focus will be on the AFM character of the deposited films and the crystal structure as the magnetic structure in NiO is strongly linked to the crystallinity (see section 2.3). Next, the growth of the Cu buffer layer and the FM multilayer is discussed in section

4.2.2. Finally, in section 4.2.3, an alternative stack geometry that was explored during this project will be introduced. This stack geometry makes use of a Pt buffer layer between the MgO substrate and the NiO film to influence the magnetic structure through the compressive strain between Pt and NiO.

4.2.1 Growing NiO thin films

As discussed before, most samples under investigation in this thesis were grown on top of crystalline MgO substrates. MgO is a transparent non-magnetic insulator that is known to hydroxylate when exposed to water and air [122]. In order to have pristine substrates to grow the multilayers on, they were ion beam milled for 5 minutes immediately prior to deposition. In this process, roughly 900 nm of material was milled away, which is insignificant with respect to the substrate thickness (500 µm), but more than enough to get rid of any hydroxylation during the transfer of the substrate to the vacuum system where milling and sputtering took place [122]. XRD and LEED measurements on the crystalline MgO substrates confirmed their monocrystallinity; these results are shown in appendix E.

As stated, the NiO layers were sputtered reactively in an environment with a gas mass flow of 15 and 1.5 sccm Ar and O_2 respectively. The target-to-sample distance, base pressure, plasma power and temperature were set to 120 mm, 1e-3 mBar, 20 W and 430°C respectively. Substrate milling, reactive sputtering, LEED and XPS measurements were all performed in a single UHV system, where the deposited sample can be prepared and investigated with these techniques without having to be removed from UHV.

XPS

Within this UHV cluster, the first test that was performed to check the quality of the deposited layers was a measurement of the XPS spectrum of the deposited layers. In the setup used for the measurements, similar to the one shown in figure 4.3, a dual anode x-ray source equipped with a Al filament was used. The Al anode has an excitation energy of $\epsilon = \hbar\omega = 1487$ eV.

In order to illustrate the change in the spectrum for NiO in comparison to atomic Ni, the broad range spectrum of a 30 nm Ni (red) and NiO (black) films is shown in figure 4.9a. When comparing the two spectra and indentifying the XPS-response of NiO, three regions are of particular interest. First of all, the appearance of the two oxide related peaks, demarked by the dotted lines are a first indication that an O-compound is formed. Most usually though, the focus lies on the 2p photoelectron emission peaks in the blue region in figure 4.9a. This part of the spectrum has been shown enlarged in figure 4.9b. The $2p_{3/2}$ and $2p_{1/2}$ photoelectron transitions are labeled.

The split between these two orbitals in Ni is a consequence of spin-orbit coupling (see e.g. [123]). Furthermore, smaller satellite peaks can be observed for both orbitals at 860 and 880 eV respectively. These peaks arise from two different mechanisms in which empty 4s and $3d^9$ orbitals can be filled [124]. In general, due to the appearance of charge-transfer states and ionic cores in the material structure in NiO, the spectrum is altered from the atomic state [110, 124]. The main feature that was used to distinguish between the atomic state and the compound state is the magnitude of the spin-orbit splitting which should increase by 1 eV. In these spectra, we found an increase of the spin-orbit splitting of 0.90 ± 0.03 eV, suggesting that indeed our deposited films have the expected composition. Film stoichiometry can also be checked from this spectrum through proper fitting of the different diffraction peaks. The

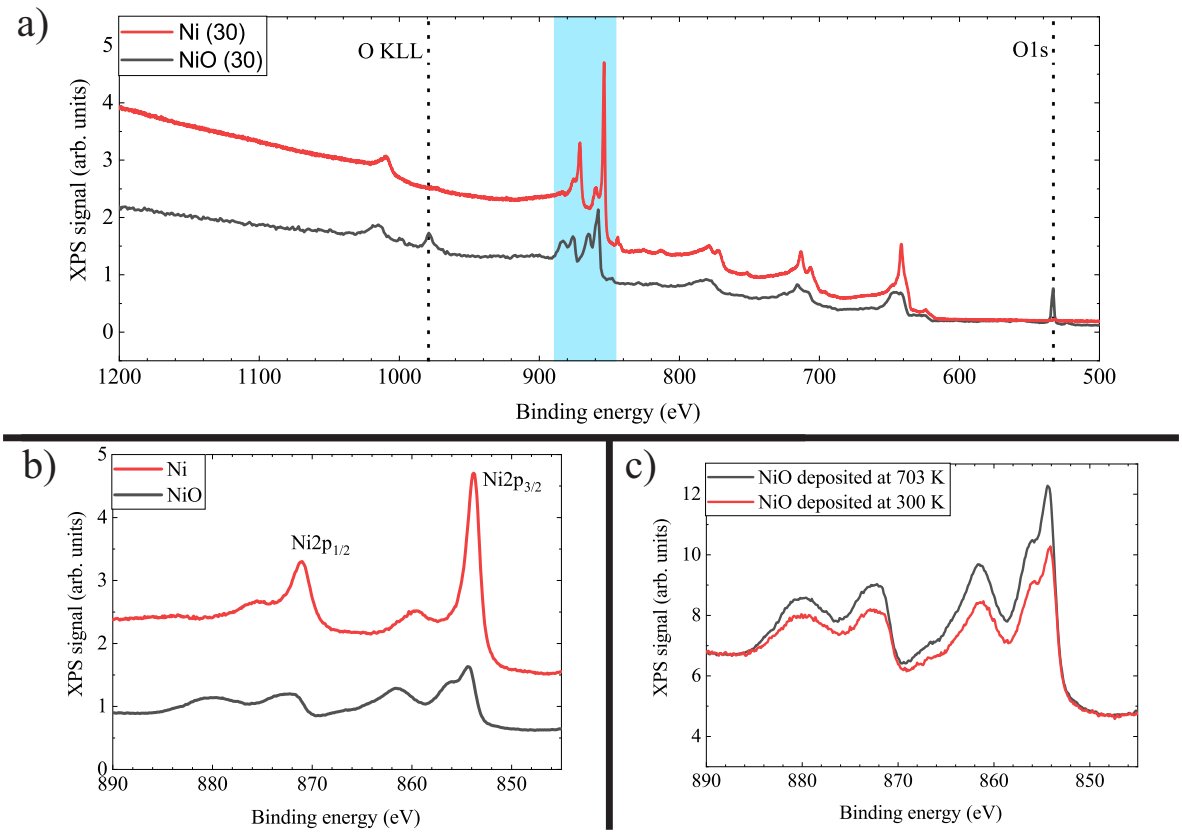

Figure 4.9: Comparison of XPS spectra of Ni and NiO (a,b), as well as for NiO films deposited at different temperatures (c). a): Broad spectrum of the NiO film deposited at high temperature. Appearance of the marked oxygen peaks is a first indication of oxidation during deposition. Region in blue shown enlarged in b. b): Comparison of the Ni2p spectrum for 30 nm films of Ni and NiO. c): Comparison of the Ni2p spectrum for 30 nm films of NiO deposited at 703 K and 300 K for transient magnetization and spin transport measurements.

fitting procedures are highly non-trivial though, both in terms of background subtraction and interpretation [110], and is beyond the scope of this thesis.

Finally a comparison is made between the spectra of NiO films grown with the same growth procedure spare the substrate temperature. The Ni2p spectra are shown in figure 4.9c for growth of 30 nm films at 300 K (red) and 703 K (black). It should be noted that the peak ratios observed in this figure are in qualitative agreement with spectra observed in literature, but the difference in peak ratios suggests a difference in stoichiometry between the two films [125]. More detailed analysis needs to be performed to derive reliable quantitative estimates of the film composition from the XPS data. Further tests have therefore been performed, mostly pertaining to the magnetic properties of the film.

Exchange bias

One indirect measure of the antiferromagnetic ordering is exchange bias (EB) at AFM/FM interfaces. EB is a form of direct exchange between the spins of the AFM and FM layer at the interface, which is present at temperatures lower than the characteristic blocking temperature T_B [126]. It is measured as a shift H_{EB} of the hysteresis loop of the FM layer.

To introduce the origins of EB, a simple bilayer consisting of a FM and an AFM layer is considered. In this system an EB can be created at the interface between the two materials in a simple experiment shown in figure 4.10a. When the system is heated above T_B, the interfacial exchange coupling disappears. This leads to a typical M-H loop as illustrated in the figure, symmetric around $H = 0$ in the absence of any particular coupling at the interface.

When then the temperature is lowered again in the presence of an external magnetic field (figure 4.10b), the uncompensated spins in the AFM at the interface (i.e. carrying a net magnetic moment when integrated over the entire surface) can align and couple with the FM spins. This leads to an energetic preference for the FM system to be aligned to the "fixed" AFM spins at the interface. Supposing the field is applied in the direction of positive H during cooling, as in figure 4.10b, this will lead to an M-H loop as shown in the bottom of the figure. The additional unidirectional anisotropy due to the EB coupling leads to the H_{EB} shift of the loop to the negative field direction.

This can be phenomenologically understood as the ferromagnetic spins being pinned when they align with the uncompensated plane of the AFM (i.e. along the positive field direction). This pinning leads to a higher required switching field to get to the state where the FM spins are antiparallel to the uncompensated plane of the AFM. On the other hand, when the ferromagnetic spins are originally oriented antiparallel to the AFM spins, the energetic preference for them to be aligned to the AFM leads to a lower required switching field to the parallel state.

To check for EB in the deposited NiO films, MgO[111]/NiO(50)/Co(2)/Pt(4) stacks were grown. M-H loops were measured in a superconducting quantum interference device (SQUID) through VSM, a method that allows for direct quantification of $\boldsymbol{M}$ in a FM [127]. Two hysteresis M-H loops were measured and are shown in figure 4.10c. The red curve corresponds to the as-deposited sample. It can be observed that the loop is symmetric around $H = 0$, i.e. no EB is observed. Directly after this measurement, the sample was first heated to above T_B (450 K,) after which it was cooled down to room temperature in an applied field of 1 T. After this procedure the second M-H loop was measured, shown as the black curve in figure 4.10. Two important changes can be observed when compared to the as-deposited sample: an increase of the coercive field of ΔH_c =13.6 mT and an EB shift of H_{EB}=-6.8 mT. The shift in

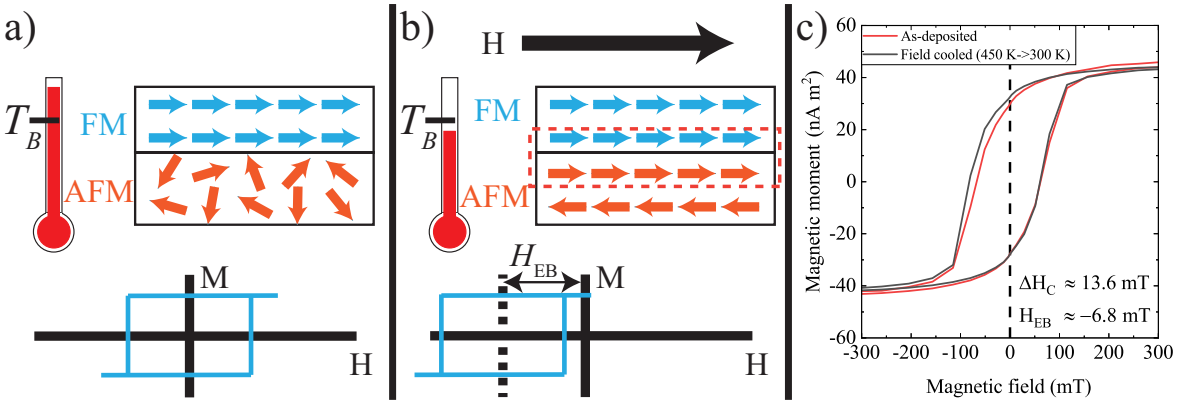

Figure 4.10: Exchange bias experiment as performed in this thesis. a): FM/AFM bilayer is heated above the blocking temperature, qualitative behaviour of a M-H loop is sketched. b): Field cooling leads to exchange coupling between spins at the FM/AFM interface. The insensitivity of the AFM order parameter to an external field leads to an exchange bias field shift of the M-H curve. c): VSM measurement on a NiO(50)/Co(2) multilayer system before (red) and after (black) field cooling as shown in b).

the negative field direction is what is expected for a positive applied field during field cooling.

Chen et Al. reported an H_{EB} and ΔH_{c} of 0.9 and 12.4 mT respectively in NiO(50)/Co(10) multilayer stacks grown on amorphous Si/SiO substrates. Though the coercivity increase is of a similar magnitude, which is expected to be related to AFM domain formation at the AFM/FM interface [128], H_{EB} reported in literature is significantly smaller than the value that was found in this thesis. The disparity in the measured H_{EB} can be explained by considering the spin structure of NiO as introduced in section 2.3. When it is grown in the [111]-direction, the stacking direction of the FM planes coincides with the film normal. The consequence is that the net magnetic moment of the first atomic plane of the AFM will be mostly uncompensated, which yields more efficient exchange coupling than when the first atomic plane is fully compensated.

These measurements suggest indeed that the NiO films that are grown are antiferromagnetic. The high H_{EB} compared to literature can be linked to the specific crystal growth direction of our films, leading to uncompensated planes and hence efficient exchange coupling.

Raman spectroscopy

Another probe for the AFM properties of NiO is Raman spectroscopy, an optical technique that probes the creation and annihilation of magnonic, rotational and vibrational excitations in the investigated material. A brief introduction to Raman spectroscopy is supplied in appendix F. The Raman spectra were obtained with a commercial Renishaw Raman spectroscope equipped with a 532-nm laser. Part of the measured spectrum at room temperature is shown in figure 4.11a. In this image two distinct peaks can be distinguished which can be attributed to two separate excitation processes. The left peak (~1100 cm^{-1}) corresponds to the excitation of two longitudinal-optical (LO) phonons. The right peak is caused by the excitation of two magnons (2M) with opposite wavenumber [129]. The presence of the 2M peak is a clear indicator for the AFM ordering in the film.

To check the AFM nature of this peak, the temperature dependence of the 2LO and 2M

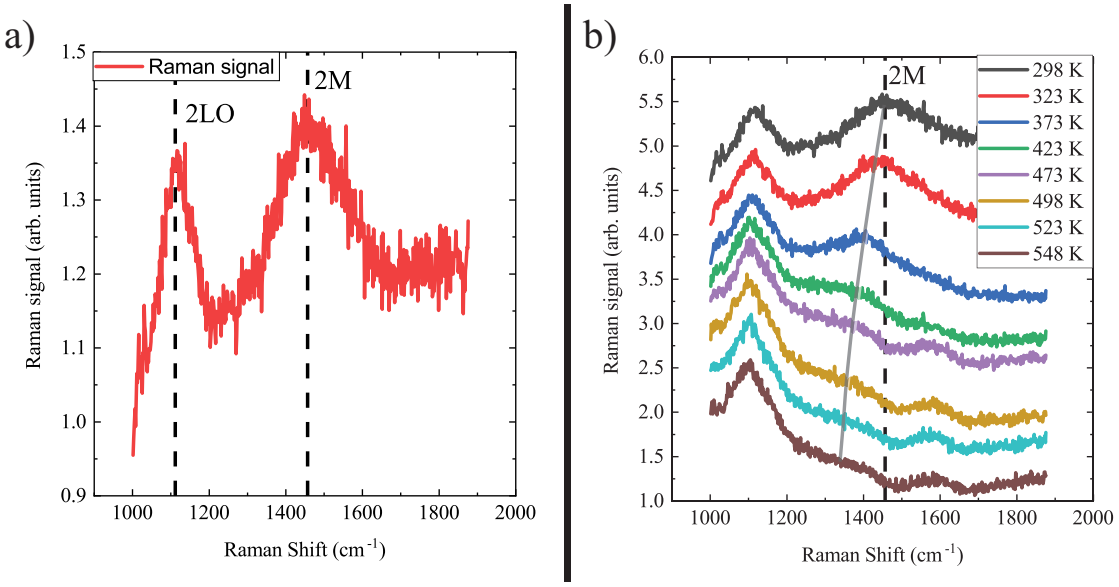

Figure 4.11: Raman spectroscopy measurements on 30 nm of NiO [130]. a): RT Raman spectrum showing the characteristic two-magnon (2M) and two longitudinal optical phonon emission peak. b): Temperature series of the Raman spectrum. Approaching T_N = 525 K the 2M mode peak intensity decays and moves towards lower raman shifts. Dashed line shows the RT Raman shift of the 2M peak. Gray line through the 2M peak at different temperatures is a guide for the eye.

peak was investigated. Raman spectra for temperatures from 298 K to 548 K are shown in figure 4.11b. The 2LO peak is a phonon peak, and shows no change in terms of magnitude and position with increasing temperature. The 2M peak however shows both a peak shift towards lower shifts, and has a decreasing magnitude with increasing temperature. The shift can be understood by considering that at higher temperature the strength of the exchange coupling, which drives the ultrafast dynamics, decreases and hence also the associated precession frequencies decrease [131], leading to the observed shift. As the AFM ordering is destroyed by the increasing temperature, the intensity of the 2M peak is expected to decrease. The observed temperature-dependent behaviour of both the 2LO as the 2M peak is consistent with similar measurements performed by Lacerda et al. [132]. These results suggest that the expected antiferromagnetic ordering is indeed present in the sputtered NiO films.

XRD

The antiferromagnetic nature as well as the stoichiometry of the reactively sputtered NiO films have been confirmed through XPS, Raman and exchange bias experiments. Another important requirement for the deposited films is that we can influence the crystal structure through the crystalline MgO substrate. For instance, when growing in the [111]-direction, the stacking directions of the FM planes in NiO are expected to be oriented along the growth direction, leading to uncompensated planes at the interface between NiO and the layer grown on top of it. This is predicted to influence the efficiency for magnon-electron spin current conversion at an metal/insulator interface [60], hence why it is investigated.

There are two critical aspects to the growth of these crystalline AFM layers through sput-

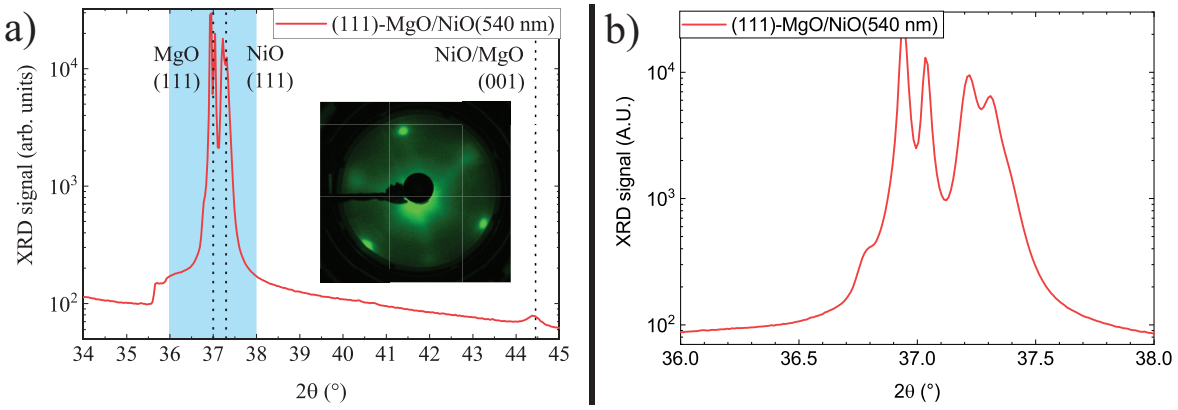

Figure 4.12: a): XRD diffractogram of NiO films reactively sputtered on a MgO[111]-substrate. The relevant peak locations are demarked by dotted lines. Inset shows the LEED pattern obtained for this sample at V_{acc} = 77 V., showing the sixfold symmetry expected for the [111]-facet. The region of the diffractogram in blue is shown enlarged in b).

tering. Firstly, the high temperature increases the mobility of the sputtered atoms promoting crystalline growth [105]. Next, the lattice matching between the AFM and the substrate should be as good as possible, as the antiferromagnetic order in NiO (and most other AFMs) is strongly linked to strain effects [8]. Furthermore, strain can lead to surface reconstruction if the lattice mismatch is large enough [133], which hampers control of the spin structure of the deposited films as well as the layered structure that is critical in the appearance of PMA in the FM multilayer in the stacks shown in figure 4.1.

The crystal structure was investigated using a commercial Panalytical XRD setup equipped with a Cu anode X-ray source. Figure 4.12a shows the XRD diffractogram of a 500 nm NiO film reactively sputter deposited at 430 °C on [111]-MgO. Five distinct features can be distinguished. The four most prominent diffraction peaks are located in the blue region. This region is also shown enlarged in figure 4.12b. Two pairs of peaks can be distinguished in this region, centered around $2\theta \approx 37°$and $2\theta \approx 37.3°$. These pairs correspond to the [111]-facet of MgO and NiO respectively and are labeled as such. Again, the peak splitting is caused by the two different k-α radiation wavelengths of the Cu anode. The close vicinity of the two [111]-peak pairs is consistent with their close lattice matching. A ternary structure in figure 4.12a can be observed at an angle of 44.5°. The peak position corresponds to the [001] facet of either the MgO substrate or the deposited NiO film. The width of the peak makes it impossible to distinguish the two. To make a quantitative comparison between the separate peaks, the following Lorentzian profile for the XRD signal was fit to the five peaks:

$$\text{XRD signal} = (2\theta)_0 + a(2\theta) + \frac{2A}{\pi}\frac{w}{4((2\theta)-(2\theta)_c)^2 + w^2}, \tag{4.6}$$

where, $(2\theta)_0$ is the offset in the signal, a is the slope of a linear background correction, A is the area below the Lorentzian profile, w is the full width at half maximum (FWHM) and $(2\theta)_c$ represents the peak position. Of particular interest for the comparison of the two crystal facets are w and the area below the beak A, as these parameters can be used to estimate the relative prevalence of certain growth directions. Using the Scherrer equation (4.5), the approximate crystallite size d can also be computed. The most important results of the fitting procedure are presented in table 4.1.

Table 4.1: Fitting parameters of the Lorentzian for the different diffraction peaks in the MgO[111]/NiO(540 nm) stack.

Crystal facet	$(2\theta)_c$	$w(^\circ)$	A(A.U.)	d(nm)
MgO[111]	36.94	0.025	1.14	350
MgO[111]	37.04	0.027	0.57	324
NiO[111]	37.21	0.08	0.69	109
NiO[111]	37.31	0.086	0.78	102
MgO/NiO[001]	44.40	0.35	0.0076	26

Since the area beneath the diffraction peak is proportional to the XRD signal, it immediately becomes clear that the [111]-facet of NiO contributes about two orders of magnitude more to the overall signal than the MgO/NiO[001] facet. Furthermore, based on the significantly broader diffraction peak for the [001] texture, the crystallite size is significantly smaller than for [111]-NiO. The found crystallite size for the substrate (350 nm) is slightly higher than the values typically found in literature of roughly 200 nm [134, 135]. It should be taken into account however, that due to the lack of knowledge of the crystallite size the estimate of the shape factor might not be representative of the actual crystallite shape and can vary by a factor of 2 [121], and therefore the exact values are only a crude estimate. The ratio between the different crystallite sizes is what should be focused. In that regard, these results suggest that the crystalline MgO[111] substrate strongly promotes the growth of the [111]-facet in NiO during reactive sputtering at high temperature, as was the aim of this growth scheme.

4.2.2 Cu and [Co/Ni]-multilayer growth

With the confirmation of the antiferromagnetic properties and the correct crystal structure of the NiO layer, the focus will shift towards the growth of the rest of the stack. This section will be split into two parts, the first one focussing on the XPS characterization of the Cu layer to check for oxidation effects of the deposited Cu layers, which are particularly relevant as the growth substrate is an oxide (NiO). The second part will focus on the magnetic properties of the FM Co/Ni multilayer systems as characterized by MOKE measurements.

Cu layer

After the high temperature deposition of NiO, the system cools down to room temperature. Following this step, a thin Cu layer of 4-5 nm is deposited to magnetically decouple the AFM layer from the FM multilayer on top for the optical experiments. XPS measurements were performed to obtain information about the Cu/NiO interface. Of main interest in these measurements is the possibility of Cu being oxidized. Stanescu et Al. investigated NiO layers deposited through molecular beam epitaxy on sputtered Cu[111] layers [136]. It was observed in this work that especially at sub-nm thicknesses, Cu dislocations lead to step edge intermixing leading to a mixed wetting layer of Cu, Ni and O.

To check the composition of the interface between NiO and Cu, explorative XPS measurements of an uncapped NiO(30)/Cu(2) sample were made. These measurements are shown in figure 4.13a and 4.13b. The thin Cu layer should still allow photoelectrons from the NiO layer

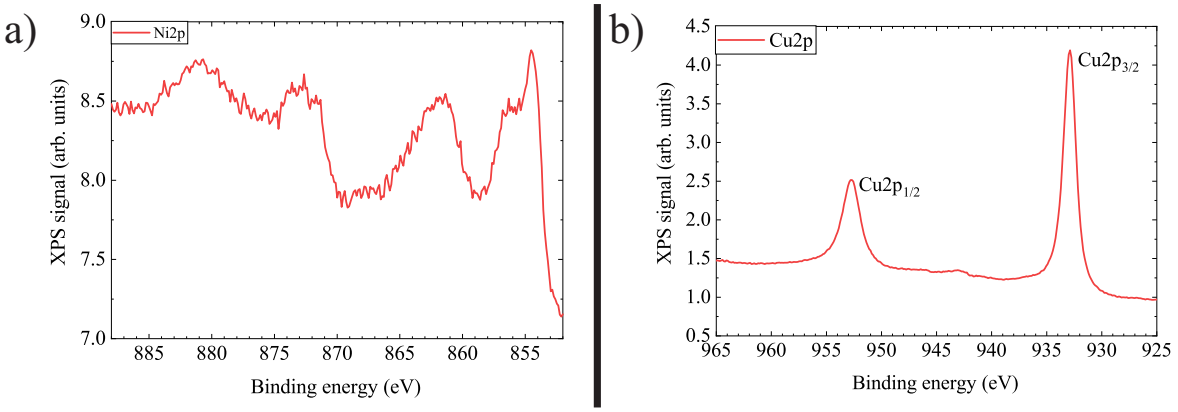

Figure 4.13: XPS spectra of the NiO/Cu(2) sample. a): Spectrum of the Ni2p photoelectron peaks. b): Spectrum of the Cu2p photoelectron peaks.

to be detected, while still being sensitive to its chemical state. As shown earlier, the XPS response of the 2p electrons in Ni changes appreciably upon oxidation. Similar behaviour is observed in CuO_2 if it is formed, where the position of the Cu2p main peaks shown in figure 4.13 is a gauge for the formation of different Cu-O compounds [137]. The peak energy for the $2p_{3/2}$ peak was found to be 932.88 eV. This position of the $2p_{3/2}$ peak is slightly higher than the values of 932.63 and 932.12 eV reported in literature [138] for pure Cu and Cu_2O respectively. However. Given an instrumental inaccuracy of 0.3 eV this suggests that the degree of oxidation of the Cu buffer layer is limited in the deposited samples. It should however be noted that a very small O1s can also be observed in the spectrum (not shown), which suggests that indeed some degree of oxidation can still have taken place.

Even though the formation of Cu_2O is likely limited based on the results presented above, the identification of the different compounds is not trivial, and as such the analysis of XPS spectra of Cu differs between different authors [137]. Furthermore, based on these measurements alone, oxidation during the (in-vacuum) transport from the sputtering chamber to the XPS chamber cannot be excluded. For full understanding of this relatively complex sputtering interface, where oxidation of the deposited layer may play a role, more systematic research is warranted. Further research may include techniques like HRTEM to investigate the composition of the interface, and may elucidate the degree of oxidation of Cu in vacuum to identify the exact oxidation mechanism in this system. This sort of experimental work is, however, outside the scope of this thesis.

Co/Ni multilayer

Another essential aspect of the investigated multilayer stack is the FM Co/Ni multilayer system used to generate spin currents. It is deposited after the Cu buffer layer described above and should exhibit PMA. Two different kinds of samples are investigated in this section. The first sample configuration that was characterized is the basic stack for transient magnetization dynamics shown in figure 4.1a: 10 nm of NiO was deposited at high temperature on a MgO[111] substrate, after which the chamber was cooled down to room temperature (RT). Next, Cu(4) and 3 repeats of Ni(0.6)/Co(0.2) finished by a Pt(1) capping layer were grown. The OOP M-H loop for this stack was measured by polar MOKE and is shown in figure 4.14a. A clear easy axis response of the FM multilayer stack can be observed by merit of the nearly

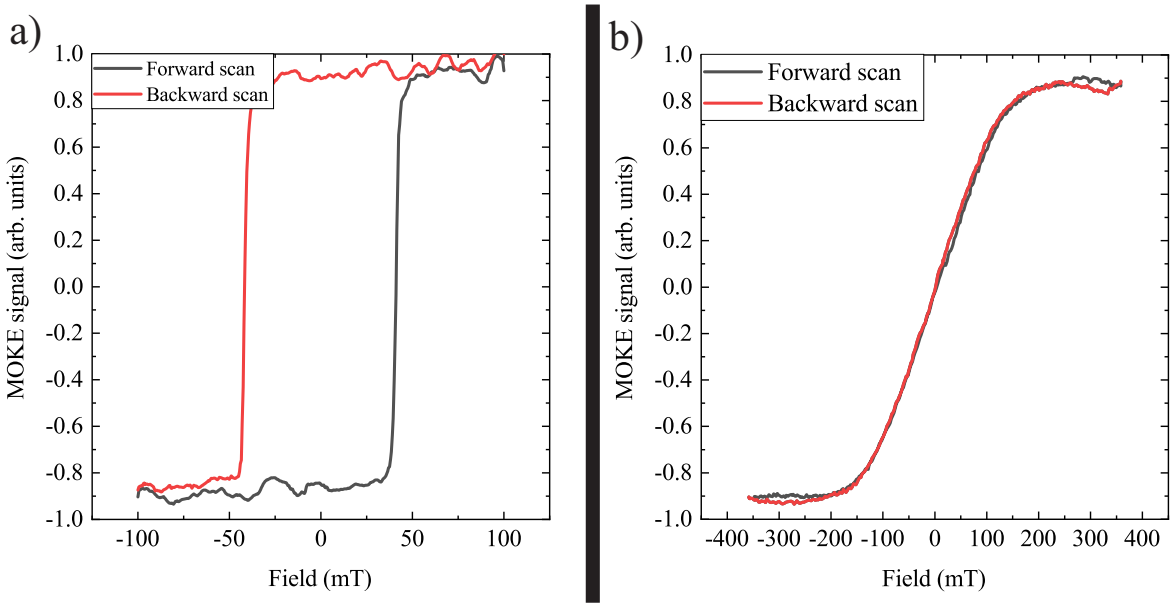

Figure 4.14: Polar MOKE measurements of the Co/Ni multilayers layers of samples a): MgO[111]/NiO(high T)/Cu(4)/Co(0.2)/[Ni(0.6)/Co(0.2]$_3$/Pt(2), and b): MgO[111]/Co(4)/NiO(RT)/Cu(4)/Co(0.2)/[Ni(0.6)/Co(0.2]$_3$/Pt(2). Thicknesses in nm between parentheses.

square magnetization switching, confirming the expected PMA. M_s was found to be 760 ± 20 kA/m. Furthermore, a coercivity of 50 mT was measured which, considering, the coercivity of Co/Ni multilayer systems can vary significantly depending on the fabrication method and the substrate (e.g. [139, 140]), is a realistic result.

For the fabrication of the second sample (figure 4.1b) the growth scheme was different in two regards: firstly a 5 nm Co layer was deposited on the crystalline MgO substrate. Also, the subsequent 5 nm NiO film was deposited at room temperature. The reason for this, as stated, is that crystal structure is expected to be less critical factor in the AFM spin transport experiment. Furthermore at high temperature the oxidation rate of Co is significantly increased [141], further supporting the argument that RT deposition is preferable for these experiments. After the 5 nm Co layer and the 5 nm NiO film, Cu(4) and 3 repeats of Ni(0.6)/Co(0.2) finished by a Pt(1) capping layer were grown identical to the sample for transient magnetization measurements described earlier in this section. The measured M-H hysteresis is presented in figure 4.14b. No easy out-of-plane axis was observed in this sample. The observed response is interpreted is as the hard-axis behaviour of the 5 nm Co layer. This layer is expected to be oriented in-plane in the absence of an external field. The coherent rotation towards the external field direction is a fingerprint of the hard axis behaviour of this layer, as discussed in section 2.1. This observation is confirmed by investigating an identical stack where the Co layer is absent and no hard axis magnetic response is observed.

It was found that the presence of the Cu layer played a central role in the appearance of PMA, as replacing the 5 nm Cu layer by a 2 nm Pt layer restored PMA. There are several potential explanations that can be explored for this apparent importance dependence on the layer on which the FM multilayer is grown. Firstly, the growth dynamics of Cu can differ depending on whether they grown on the crystalline NiO film grown at high temperature

or on the films without a particular crystallographic orientation grown at RT. In literature, the growth conditions for growth on the [111]- and [001] Cu facets was investigated [95–97]. In the work on Co/Cu[111] it was shown through scanning tunneling microscopy that island formation is the growth mode for 0.6 monolayer of Co in their system. These islands were found to form at the terrace steps in the Cu[111]-substrate and had a typical height of 0.8 nm [95] . This is both driven by efficient diffusion on the Cu[111]-substrate, as well as potentially driven as a means of strain relaxation [142].

This island formation is in contrast to what is observed for the first monolayer of Co when grown on a Cu(100) substrate. Here it was observed that a reduced mobility of the Co atoms promotes the growth in uniform layers over the island formation in the sub-nm regime [96,97]. These results indicate that the growth mechanism is fundamentally different depending on the precise crystal structure of the substrate layer. It is hypothesised that this sensitivity translates to our own growth process. In the measurements performed for this thesis, it was shown that for Cu/Co grown on crystalline NiO and RT NiO the magnetic properties are fundamentally different. If indeed the growth direction of Cu differs significantly between these two samples shown in figure 4.14a and 4.14b, this may also lead to the observed change in magnetic properties of the Co/Ni mulitlayer stack through a decrease of interface quality.

Further research into this interesting interface can focus on the understanding of the Cu buffer layer. LEED and XRD can be used to check the crystal structure of the Cu layer, and high spatial resolution techniques like STM or HR TEM can give more detailed insight of the Co/Ni multilayer system, especially for the first few monolayers grown. Finally, if surface reconstruction plays a role, temperature variation during deposition may also influence the quality of the FM multilayer, as the higher temperature leads enhanced diffusion of deposited atoms [99]. It should however be noted that interdiffusion effects can start playing a role for ultrathin layers of Co grown on Cu [143].

4.2.3 Long range ordering - Pt/NiO

With this, the most important aspects and challenges surrounding the growth of the stacks for the optical experiments have been treated. As shown, the adddition of crystallinity to the sputtering process creates extra restrictions on the growth process and poses new challenges. Particularly, in the context of AFMs, the strain exerted by the substrate (MgO) on the deposited film (NiO) becomes an important parameter. The magnetic structure of NiO is coupled to strains in the material through magnetostriction, giving possibilities to strain driven domain wall motion and imaging antiferromagnetic domains through linear birefringence [45]. Furthermore, recently it has been shown that compressive and tensile strains exerted on NiO through a crystalline substrate can strongly influence the preferred spin direction [144]. The compressive (tensile) strain exerted by a $SrTiO_3$ (MgO) substrate was calculated to lead to an IP (OOP) preferred direction of the Neél parameter with respect to the FM planes in which the spins are aligned.

This result from ab initio calculations opens up interesting possibilities for the thin film engineer. Being able to directly influence the spin structure in AFMs simply by exerting the right strains can be very valuable for the intended experiments in this thesis. It is expected based on the work above that a compressive strain leads to an in-plane anisotropy which leads to a 90 degree angle between the OOP polarized spin current and the AFM spins when it is grown in the [111]-direction. To induce this compressive strain, a Pt layer is used as a template layer as it is possible to grow material with the right texture on crystalline MgO

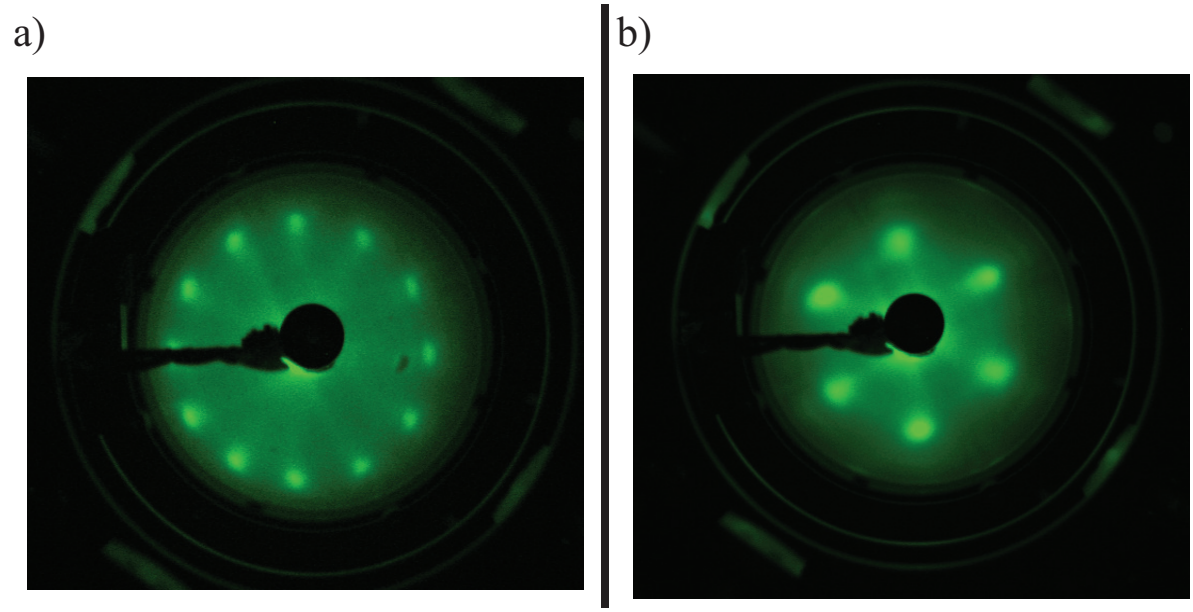

Figure 4.15: a): Representative LEED diffractogram of the Pt(20)/NiO(60) films grown on Si/SiO_2 and MgO[001] substrates. b): LEED diffractogram of the Pt(20)/NiO(60) films grown on MgO[111].

by sputtering [105]. In this experiment we use the growth scheme proposed in the work by Lairson et al.; The temperature was set at 565°C, while the pressure, sample to target distance and power were set at $4 \cdot 10^{-3}$ mBar, 60 mm and 5 W respectively. Films of 20 nm Pt and 60 nm of NiO were grown on three different substrates: MgO[001], MgO[111] and Si/SiO_2. It is expected that any strain caused between the Pt and MgO layer has decayed over the 20 nm thickness of the film, so that the strain from the Pt on the NiO is compressive.

LEED

The first test to check the crystallinity of the deposited sample is LEED. Figure 4.15a and 4.15b respectively show a representative diffractogram of the Pt/NiO films deposited on Si/SiO_2 and MgO[001] (a), and the Pt/NiO films deposited on MgO[111] (b). The diffractogram of the bilayer grown on Si/SiO_2 and MgO[001] shows a twelvefold symmetry which is not expected from bulk NiO. The increase in symmetry axes with respect to growth on MgO can be understood as follows. Due to the preferred [111] growth direction of the Pt, two distinct FCC stacking sequences can be distinguished in which every second layer is twisted by 60°with respect to the other stacking sequence [145]. In the MgO[111] crystal, the depostied Pt[111] film adopts the stacking direction of the (face centered cubic) MgO[111] substrate, hence only leading to one stacking sequence manifesting in the diffractogram. The hexagonal and dodecagonal symmetry of the LEED spectra is a first indication that the [111] facet is dominant on all three substrates. To further quantify these observations, XRD measurements have been performed.

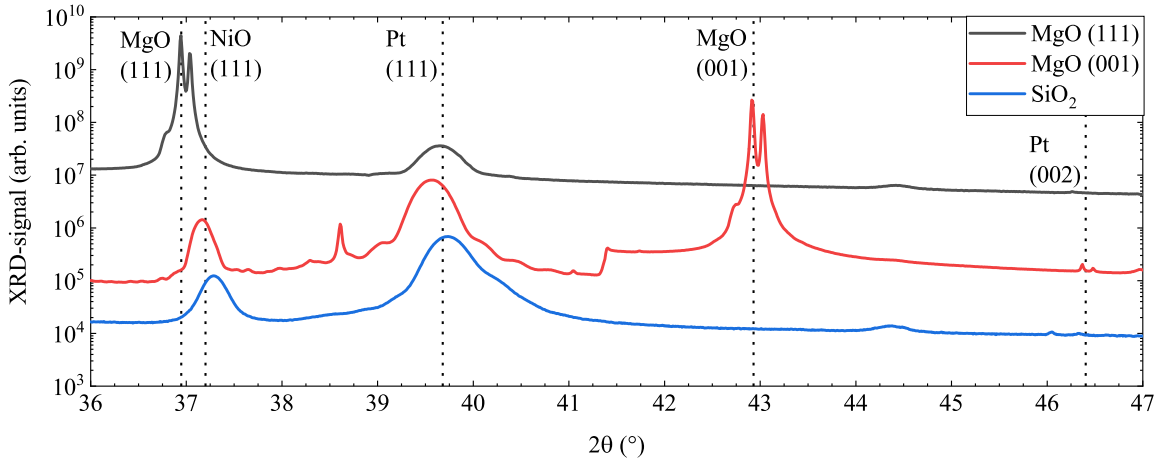

Figure 4.16: XRD spectra of the Pt(20)/NiO(60) films grown on MgO[111] (black), MgO[001] (red) and Si/SiO_2 (blue). Diffraction peaks of interest are labeled and marked by dotted lines.

XRD

The XRD diffractogram obtained for the deposition on the three substrates are shown in figure 4.16. The first distinctive feature is that on all three samples the Pt[111] texture ($2\theta = 39.7°$) is dominant over other directions. This result suggests that the growth scheme that was used leads to textured growth, contrary to the epitaxial growth observed by Larison. This observation was confirmed by a scan of the [111] peak intensity as the sample is rotated around its normal as illustrated by ϕ in figure 4.17a [105].

A second important observation is the appearance of the Pt(002) peak at $2\theta = 46.4°$ for the sample grown on MgO[001]. Thus, to some extent the crystal structure of the substrate is present, as in neither of the other two samples (MgO[111] and Si/SiO_2) these [001]-peaks are visible. However, the relative peak intensity of the Pt[111] and Pt[001] peaks shows that the growth parameters strongly favour the reorientation of the sample to the [111] face. The associated peak shift of the Pt[111] peak in this sample can be explained by the tensile strain from the substrate, as shown in figure 4.7. As can be seen, the most relevant growth mode on the MgO[001] sample is still the NiO[111] direction, meaning that this scheme at this point does not offer the texture templating required for efficient strain control while also inducing the crystal structure from the substrate onto the NiO layer.

The final striking feature of the diffractograms presented in figure 4.16 is the absence of the NiO[111] peak in the MgO[111]-sample. A surprising result, since the LEED spectrum for this sample clearly shows the sixfold symmetry expected for [111]-NiO, suggesting that there is a crystaline material present on the sample. To study the texture of this sample in more detail, a texture map was performed. To understand this measurement it is important to understand the different tilt and rotation angles available in the setup. Figure 4.17a shows a cartoon of the measurement geometry. The angles θ, ω en ϕ represent the angle between the X-ray beam and the horizontal, the angle between the sample plane and the horizontal plane, and the rotation angle of the sample around its normal respectively. By tilting and rotating the sample, sensitivity to slightly tilted lattice planes and orientation dependent reflections can be achieved. An example of a tilt sweep can be observed in figure 4.17b. Here the sample is kept at constant ϕ while varying the tilt angle ω. As can be seen a tilt of about 2° already

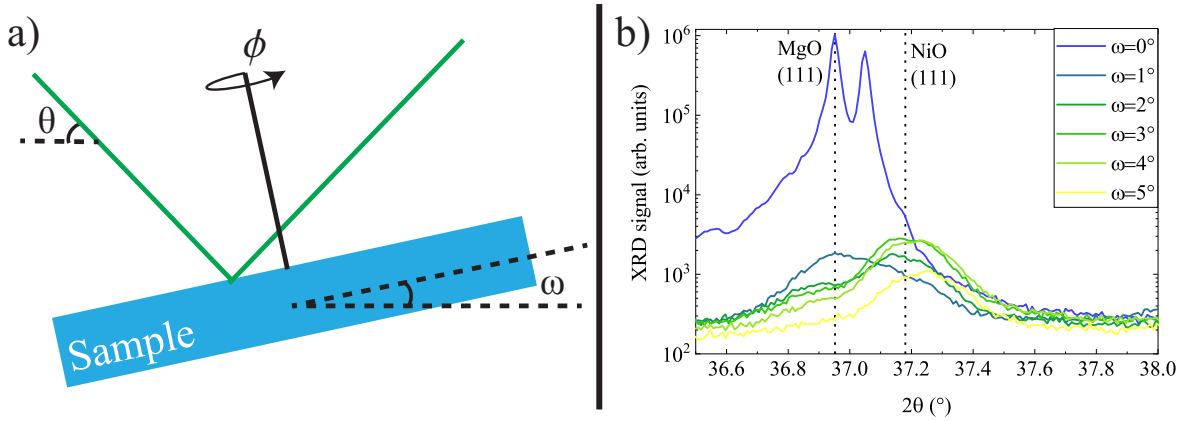

Figure 4.17: a): Illustration of the tilt and rotation angles used in the texture mapping experiments described in this section. b): XRD diffractograms of the MgO[111] peaks and the NiO response for various tilt angles ω

completely filters out the response from the MgO[111] substrate. Furthermore, from $\omega = 2°$, a relatively broad feature appears at $2\theta = 37.2°$, consistent with the NiO[111] texture. A texture map of the 37.2° peak is shown in figure 4.18. This polar contour plot shows the peak intensity as a function of ϕ (azimuthal angle) and ω (radius). It is clear that the texture of the [111] texture is tilted with respect to the MgO[111] crystal plane. Tilted grain boundaries have been observed before in NiO and can be caused by a manifold of different phenomena, such as but not limited to edge dislocations and stacking faults [146]. Note that for positive tilt, the NiO peak response is not centrosymmetric in ϕ. There is as of yet no explanation for this observation.

Further understanding of the growth of the Pt layer on the different substrates is therefore essential to be able to exploit the strain-dependence of the magnetic anisotropy in NiO. Starting points for improving the templating procedure could be the variation of growth temperature, and the growth of thinner Pt so that relaxation to the Pt-[111] face is not promoted.

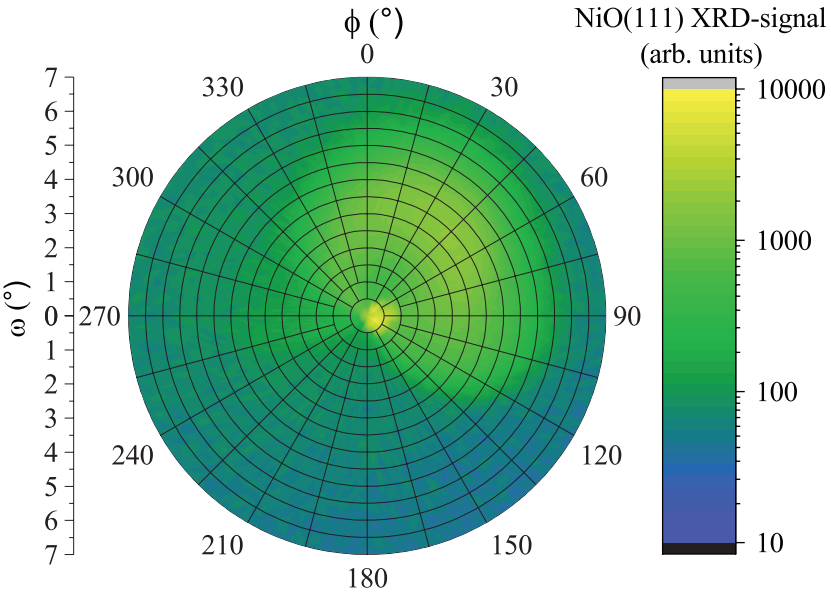

Figure 4.18: Polar contour plot of the NiO[111]-peak intensity as a function of the tilt angle ω (radius) and the rotation angle ϕ of the sample (azimuthal).

4.3 Conclusion

In this chapter, it has been demonstrated that antiferromagnetic thin NiO films can be deposited through high temperature reactive sputter deposition. The antiferromagnetic properties of these films were confirmed through exchange bias experiments and Raman spectroscopy, specfically focused on the two-magnon peak in the spectrum. Furthermore, the depostied films were found by XRD to possess the same texture as the crystalline MgO substrates on which they were grown. The magnitudes of the [111]-texture peak and the [001]-texture peak signal differed by two orders of magnitude.

In order to facilitate the optical experiments both a Cu buffer layer and a Co/Ni multilayer stack needed to be grown on top of the NiO layers. To characterized the interface between the Cu and NiO layer explorative XPS measurements were performed. Though further quantitative analysis of the spectrum is required, first comparison of the spectra to literature suggest little formation of Cu-O compounds.

The FM Co/Ni multilayers which should exhibit PMA were characterized with MOKE in the polar geometry. When Cu is grown on the NiO films deposited at high temperature, the multilayers exhibit clear PMA with a coercivity of 48 mT. When the Cu film and the Co/Ni multilayer are grown on NiO deposited at RT however, the PMA disappears. One potential explanation is the difference in the growth modes on different textures of Cu. This difference in texture may then arise from the difference in crystallinity between the NiO films grown at high T on crystalline MgO, and the NiO films grown at RT on amorphous SiO_2. Further experiments are required however to establish the cause of the lack of PMA.

Finally, a novel growth scheme was presented to manipulate the strain from the substrate on NiO. By using Pt as a buffer layer between NiO and the MgO, the strain from the substrate can potentially be changed from tensile to compressive. The first prerequisite then is that the Pt layer exhibits the same texture as the MgO substrate. First experiments using this

Pt buffer layer indicate that with the first proposed growth scheme, the reorientation of the Pt layer to the [111] face is faovurable during growth. It is however also shown that some of the substrate texture is still present suggesting that there is space to improve the templating quality of the MgO on the Pt.

Chapter 5

Optical measurements

In the previous two chapters, a numerical description of the response of the antiferromagnetic order parameter to optical spin currents was described, as well as the growth and characterization of sputter deposited AFMI NiO films in magnetic multilayer stacks. Based on the combined spin transport and dynamics model described in chapter 3, quantitative estimates of the maximum induced magnetization in the AFM and the dynamics of the magnetic state have been made. Next, in chapter 4, the sample growth and characterization process was treated, leading to the magnetic multilayer stacks used in this chapter.

Two kinds of experiments on the developed samples are considered in this chapter: In the first one, optical spin currents are excited from a ferromagnetic multilayer, which are expected to induce a small transient magnetization in the NiO, which if present can be measured by merit of the Faraday effect (see section 2.4). The second experiment tests the use of NiO as a spin transport layer, where a spin current impinging on the Cu/NiO interface can be converted in a magnonic spin current. If this perpendicularly polarized magnon spin current then reaches an IP Co layer, a small canting of the magnetization is expected, which can also be detected with the Faraday effect. These two experiments were illustrated conceptually in figure 3.1a and 3.1b respectively.

Before going to the results of the experiments, the experimental basics of the time-resolved Faraday effect (TRFE) will be discussed in section 5.1. This technique was used to investigate the response of the magnetic multilayer sytems to laser excitation on fs timescales. The main results for these pilot measurements on antiferromagnetic spin dynamics and the magnonic spin transport in sputtered NiO films are presented in sections 5.2.1 and 5.2.2 respectively.

5.1 Experimental methodology: time-resolved Faraday effect

To characterize the magnetic state of the stack as a function of time, TRFE is used. In figure 5.1 a schematic representation of the TRFE setup used for the experiments shown in section 5.2 is presented. A 5 W continuous-wave diode-pumped laser is sent through a Ti:Sapphire oscillator which produces 80 fs pulses with a tunable wavelength between 720 and 780 nm at a repetition rate of 80 MHz. The beam is sent through a 90:10 beamsplitter, which separates it into two beams. The high (low) intensity beam is referred to as the pump (probe). The pump is used to demagnetize the sample, while the probe is used to measure the magnetic state of the sample after demagnetization.

Similar to the MOKE setup described in section 4.1.5 the probe beam is sent through

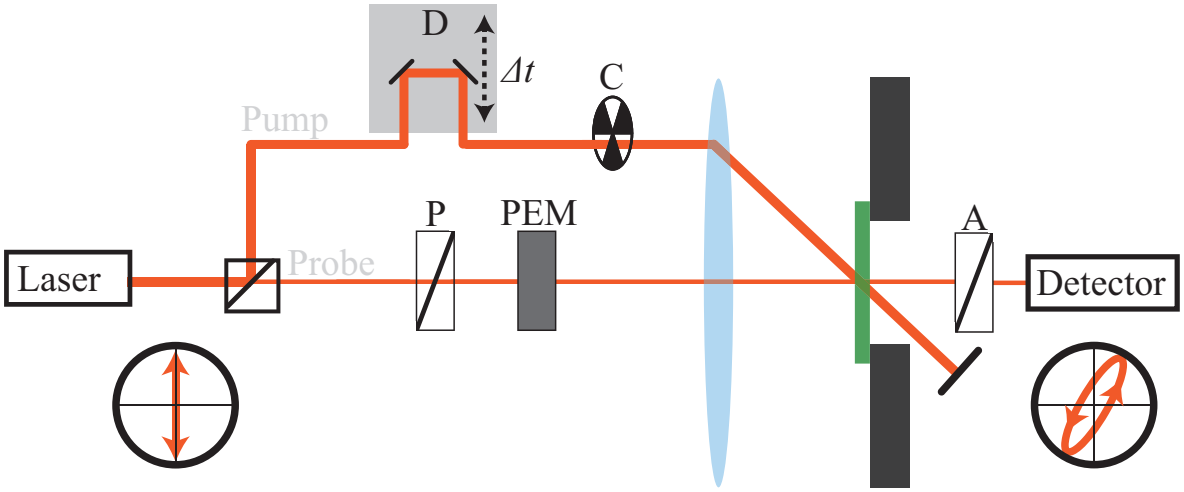

Figure 5.1: Schematic representation of the TRFE setup. The polarization of the light after the polarizer (P) and after the sample (in green) are illustrated in the left and right circles respectively. Legend: P = polarizer, PEM = photo-elastic modulator, D = delay stage, C = chopper, A = analyser.

a polarizer and will undergo a change in ellipticity and a rotation of the polarization proportional to the OOP component of the magnetization in the sample (green). The analyser is then introduced after to characterize this rotation angle in terms of the transmitted laser intensity. Again, the PEM is used so that after locking in on its modulation frequency, the signal-to-noise ratio can be improved.

The pump on the other hand, will be sent through a delay stage (D) which consists of a retroreflector mounted on a motorized translation stage. When the retroreflector is at its starting position the path length of the pump and probe beam will be the same, i.e. they arrive at the sample at the same time: $\Delta t = 0$. When the retroreflector is now moved so that the pump-path is made shorter, the pump will arrive earlier than the probe: $\Delta t > 0$. By moving the retroreflector 0.15 mm, a delay of 1 ps can be achieved. By sweeping the position of the retroreflector, the magnetization as a function of Δt can be measured. Given the fs width of the laser pulses, sub-ps resolution of the magnetization can be obtained in the temporal domain. A chopper (C, $f \sim 60$ Hz) is also included in the setup, by locking-in on the chopper frequency only pump-induced changes to the magnetic state are detected.

Since the samples described in chapter 4 are grown on transparent substrates, the measured quantity is the Faraday rotation (i.e. circular birefringence) due to the OOP component of the magnetization, ΔM_{OOP}. For this purpose, the sample is mounted on a custom sample holder (see appendix G for exact specifications). After the pump and the probe have been focused on and transmitted through the sample, the pump is blocked, while the probe is detected by a Si-amplified photodetector. The detected signal is then sent through two consecutive lock-in amplifiers locked in on the PEM and chopper frequencies respectively. The resultant signal is then proportional to ΔM_{OOP} (see section 2.4). All the experiments described in this chapter are performed at room temperature. For a more in depth and quantitative treatment

of these setups for MOKE measurements which are in many aspects similar to TRFE, the following references can serve as a starting point for further reading [34, 35].

5.2 Results and discussion

With the measurement scheme described in the previous section, the time-resolved behaviour of ΔM_{OOP} can be measured. In this section the TRFE measurements that were performed on the samples for transient magnetization and spin transport are shown. First, the experiment to measure transient magnetization dynamics will be discussed. From the numerical work in chapter 3, a measurable out-of-plane component of the magnetization is expected if the excited spin dynamics are coherent. This response should only be observable for Δt <10 ps, which is the temporal region on which shall be focused in these measurements presented in section 5.2.1.

5.2.1 Transient magnetization dynamics in NiO

The first step in the transient magnetization dynamics experiments described below was to confirm that the sign of the magnetization of the FM layer with PMA could be distinguished. Figure 5.2a shows two typical demagnetization curves measured for either positive or negative ΔM_{OOP}. The observed sign change in V_{mag} between positive and negative ΔM_{OOP} can be understood by realizing that the magnetic signal $V_{\mathrm{mag}} \propto \theta_{\mathrm{F}} \propto \Delta M_{\mathrm{OOP}}$ and hence a change in sign of the magnetization also entails a sign change in the magnetic signal. Furthermore, by considering the difference between these two signals, any non-magnetic pump-induced effects can be filtered out; as non-magnetic effects, like transient reflectivity, do not change sign upon switching of the FM layer magnetization direction. When the two signals are thus subtracted, the magnetic component remains.

To further explain the observed transient behaviour, the black trace in figure 5.2a will be considered in more detail. For negative time delays, the magnetization is constant as the demagnetizing pump has not yet arrived. Then starting at $\Delta t = 0$ (disregarding the finite temporal profile of the pump) the electron system is heated on a timescale of less than 0.1 ps. The heat transfer to the spin system (in the 3TM interpretation) leads to a decrease of the magnetization and therefore the change in the Faraday rotation of the linearly polarized light of the probe. This is measured as the decrease in signal in the first 0.6 ps. Next, through heat diffusion out of the sample via the substrate, and equilibration with the phonon system, the magnetization returns to its original value on the time scale of several tens to hundreds of picoseconds.

This kind of measurement will be used to investigate the response of the NiO film to optical spin currents. Therefore a detailed measurement series was made of the response of NiO to ultrafast demagnetization in the temporal region denoted in blue in figure 5.2a on the following sample: [111]-MgO/NiO(30)/Cu(20)/Co(0.2)/$[\mathrm{Ni}(0.6)\mathrm{Co}(0.2)]_3$/Pt(3), where numbers between parentheses represent thicknesses in nm. The averaged result after subtracting the signal for positive and negative ΔM_{OOP} is shown in figure 5.2b in red. Two physical quantities were assessed based on the measured data: the characteristic relaxation timescales associated with the demagnetization process, and the transient magnetization response of the AFM.

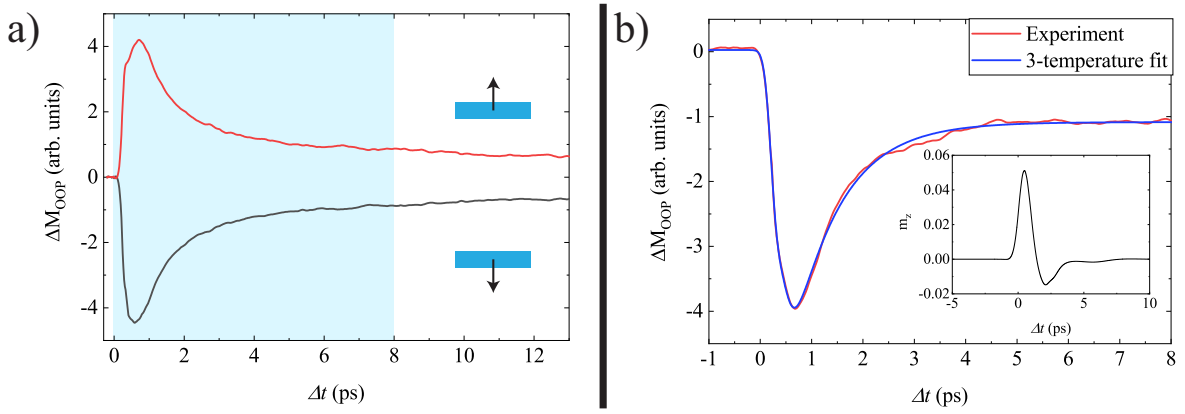

Figure 5.2: a): Polarity dependence of the measured signal to the OOP component of the magnetization on a [111]-MgO/NiO(30)/Cu(20)/Co(0.2)/[Ni(0.6)Co(0.2)]$_3$/Pt(3) sample. b): Measurement series (red) of the blue region in (a). A fit to the experimental data based on equation (5.1) is shown in blue. Series consisted of 10 measurements for positive and negative ΔM_{OOP}, which were subtracted from each other to filter out non-magnetic components of the signal. Inset: time trace of the induced OOP magnetization m_z in the NiO as calculated with the model presented in chapter 3 for typical values G_{em} = 500 nm/ps and d_{Cu} = 20 nm.

Characteristic time-scales

To obtain information about these characteristic timescales associated with the demagnetization, an analytic solution of the 3-temperature model in the low-fluence limit, derived by Dalla Longa [147], was fit to the experimental data shown in figure 5.2b:

$$\Delta M_{\mathrm{OOP,3T}} = \Theta(\Delta t)\left[- \frac{\left(A_2\tau_{\mathrm{e\text{-}p}} - A_1\tau_{\mathrm{M}}\right)\exp(-\Delta t/\tau_{\mathrm{M}})}{\tau_{\mathrm{e\text{-}p}} - \tau_{\mathrm{M}}} - \frac{\tau_{\mathrm{e\text{-}p}}(A_1 - A_2)\exp\left(-\Delta t/\tau_{\mathrm{e\text{-}p}}\right))}{\tau_{\mathrm{e\text{-}p}} - \tau_{\mathrm{M}}} + A_1\frac{1}{\sqrt{t/\tau_0 + 1}}\right] * \Gamma(\Delta t), \quad (5.1)$$

where $\Theta(\Delta t)$ is the Heaviside step function, τ_0 is the characteristic time scale for heat diffusion out of the system, τ_{M} is the angular momentum loss time scale for the generated spin accumulation, $\tau_{\mathrm{e\text{-}p}}$ is the typical electron-phonon (e-p) coupling timescale of the equilibrating scattering processes occurring after the laser-induced heating, $\Gamma(\Delta t)$ is the (assumed) Gaussian temporal pulse shape of the laser, A_1 is proportional to the equilibrium signal before the pump beam arrives, and A_2 is proportional to the initial heating of the electron subsystem. The two leftmost terms between square brackets represent the heat exchange between the three subsystems (electron, phonon and spin) after heating, whereas the rightmost term describes the heat diffusion out of the system.

All parameters from the fitting procedure are shown in table 5.1. Good agreement between theory and data is found. The found parameters for the characteristic time scales $\tau_{\mathrm{e\text{-}p}}$, τ_{M} and τ_0 are roughly in line with what is typically reported for these metallic systems and insulating

substrates, namely around 400, 100 (metal) and 4000 (substrate) fs respectively [147–149], which supports the notion that the demagnetization of the [Co/Ni] multilayer is measured.

Table 5.1: Parameters for the fit to the transient magnetic birefringence measurement shown in figure 5.2.

Parameter	Unit	Value
A_1	*a.u.*	-8.85 ± 0.09
A_2	*a.u.*	-131 ± 3
$\tau_{\text{e-p}}$	fs	350 ± 6
τ_{M}	fs	107 ± 2
τ_0	fs	5600 ± 200

Transient magnetization

With the typical timescales confirmed to correspond to those typically seen in ultrafast laser induced demagnetization, the magnetic response of the NiO film can be considered. The typical transient behaviour of the OOP magnetization m_z that was induced in the NiO was calculated with the model presented in chapter 3 and plotted in the inset of figure 5.2b. As discussed in chapter 3, it resembles the spin current pulse ($J_s \propto dM/dt$). This transient behaviour of m_z was expected to be superimposed on the demagnetization curve shown in figure 5.2b in the $1 - 10$ ps range. However, no response can be observed other than the typical demagnetizing behaviour of the Co/Ni multilayer.

The physical reason for the absence of a measurable magnetization can be caused by several potential complicating factors when comparing the experimental system to the simplified model discussed in chapter 3, one of which is the domain structure. Recently, Xu et al. observed domains of order 1 µm in NiO films with similar thickness as the ones used in this thesis [150]. Supposing that domains of the NiO films grown in this thesis are of a similar size as those shown by Xu, which is reasonable given the similar fabrication methods, the laser pulse diameter ($\sim$ 5µm) is significantly larger than the $\sim$ 1 µm domains. It is therefore deemed likely that the generated spin current pulse impinges on an antiferromagnetic multi-domain state.

This would imply that the macrospin approximation discussed in chapter 3 – which states that the oscillating magnetization component in the AFMI is uniform throughout the area affected by the spin current – may be an unsufficiently accurate description of the physics. Recent work by Ross et al. showed that the damping of collective exciations like magnons in AFMIs are governed by their interaction with domain walls, and hence the domain size [151]. Any domain structure may due to pinning effects therefore further limit the measurable magnetization component in the optical measurements presented in this section. Given the expected multidomain structure from the work by Xu et al. [150], the spin dynamics on the time scale of the laser pulse is thus expected to be influenced by the presence of these domain walls.

Several other factors can also play a role in these fairly complex multilayers, such as the quality of the Cu/NiO interface, and local heating of the AFM, which may also alter the magnetic structure in NiO [8,45,59]. In general however, the numerically estimated magnitude of the transient magnetization from chapter 3 is potentially an overestimation considering the

model completely ignores any internal magnetic structure of the AFMI. Taking into account the already relatively small Faraday rotation estimated from these idealized model results (order 0.1-1 µrad), the actual Faraday rotation may well be below the noise floor of the used measurement setup (order 1-10 nrad [86]). Further research is hence required, which should initially focus on visualizing the domain structure of the sputtered NiO layers, and quantify their influence on the spin dynamics in NiO. A more detailed outlook is provided in chapter 6.

5.2.2 Spin transport through NiO

In this section, the pilot experiments on the magnonic spin transport samples (see figure 4.1b) are presented. TRFE measurements were performed to characterize the properties of NiO as a spin transport layer in the following sample geometry, where numbers between parentheses indicate thicknesses in nm: [001]-MgO/Co(4)/NiO(5)/Cu(4)/Co(0.2)/$[Ni(0.6)Co(0.2)]_3$/Pt(3). As was discussed in section 4.2.2, the [Ni/Co] multilayer did not show PMA in these samples and should consequentially have an IP easy axis. Since the probe laser beam, was aligned to propagate through the middle of the focusing lens and hence perpendicular to the sample surface, no demagnetization signal from such an IP oriented FM is expected (see section 2.4).

Figure 5.3 shows (in red) the detected signal ΔR as a function of Δt from a measurement series on such a [001]-MgO/Co(4)/NiO(5)/Cu(4)/Co(0.2)/$[Ni(0.6)Co(0.2)]_3$/Pt(3) sample. The non-magnetic origin of this curve was confirmed by the absence of the switch in signal polarity upon applying an external magnetic field such as that shown in figure 5.2a. Since the curve strongly resembles the demagnetization signal, it is hypothesised that the observed response also originates from the ultrafast heating of the sample via laser absorption by the metallic layer; a similar response is observed in transient pump-probe reflectance measurements in normal metals, which originates from the same ultrafast heating by a pump pulse [72, 152].

As the same e-p relaxation processes are expected to play a role in the equilibration of the sample after heating, it is instructive to compare this specific typical time scale $\tau_{\text{e-p}}$ to that found from the 3-temperature fit in section 5.2.1. To get an estimate of $\tau_{\text{e-p}}$ from the temporal profile shown in figure 5.3, a simple 2-temperature model was used. Contrary to the 3-temperature model, the absence of an OOP magnetization suggests that the magnetic subsystem does not play a prominent role. From the 2-temperature model, a similar expression as equation (5.1) can be derived [148, 153]:

$$V_{\text{OOP,2T}} = \Theta(\Delta t)\left[K_1 \exp\left(-\Delta t/\tau_{\text{e-p}}\right)[1 - \exp(-\Delta t/\tau_{\text{th}})] + K_2[1 - \exp(-\Delta t/\tau_{\text{th}})]\right] * \Gamma(\Delta t), \quad (5.2)$$

where K_1 and K_2 are proportionality constants representing the magnitude of laser induced heating of the electron bath and lattice repectively, and τ_{th} is the initial electron thermalization time scale. Within the outer square brackets, the first and second term represent the electronic and lattice system response to the laser excitation. Note that only the electronic system is affected by the laser heating represented by the term $[1 - \exp(-\Delta t/\tau_{\text{th}})]$. The fit of equation (5.2) to the data is shown in blue in figure 5.3; the fit parameters are shown in table 5.2. $\tau_{\text{e-p}}$ was found to be 361 ± 4 fs, which corresponds to values typically found in these metallic multilayer systems (~ 400 fs) [147, 148], as well as being in the same order of magnitude as $\tau_{\text{e-p}}$ found in the transient magnetization measurements (360 ± 6 fs). This further substantiates that indeed the nascent electron distribution induced by laser heating

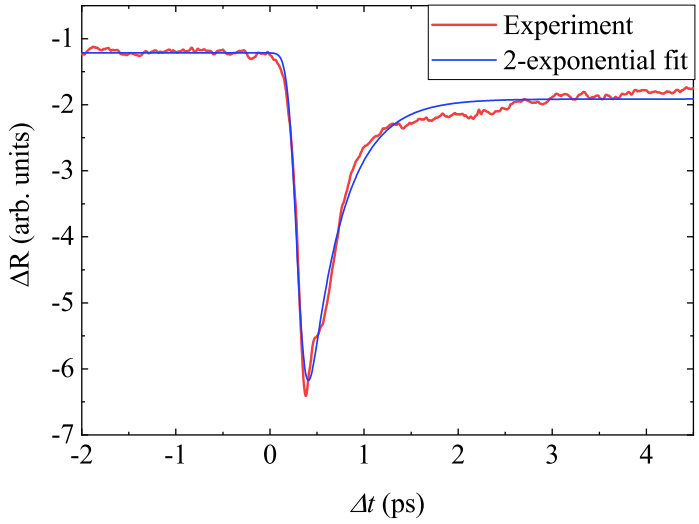

Figure 5.3: Time-resolved pump-induced change to the polarization rotation angle ΔR in a [001]-MgO/Co(4)/NiO(5)/Cu(4)/Co(0.2)/$[Ni(0.6)Co(0.2)]_3$/Pt(3) sample, thicknesses in parentheses in nm. Red is a measurement series from the experiment, blue is a fit based on the two exponential model from equation (5.2). Note that in the absence of an OOP magnetization component, no subtraction of curves for positive or negative magnetization was performed.

and the subsequent equilibration with the phonon system is responsible for the observed transient profile of ΔR. It should be noted that this very simple model does not account for heat diffusion, hence the poorer fit at longer time scales.

Table 5.2: Parameters for the fit to the time-resolved measurement shown in figure 5.3.

Parameter	Unit	Value
K_1	arb. units	7.18 ± 0.05
K_2	arb. units	0.698 ± 0.007
τ_{th}	fs	90 ± 10
$\tau_{\text{e-p}}$	fs	391 ± 4

One possible explanation for the transient signal is that the non-equilibrium electron distribution after heating enhances/diminishes the transmittance of the sample. To pinpoint what exact processes figure 5.3 represents though, further work is required. Follow-up research should first confirm unequivocally whether this transient behaviour is indeed a transient reflectance effect and not a magnetic artefact of the IP FM layers. This can be done by fabricating a stack with similar absorptance, but omitting the ferromagnetic metals in favour of NMs. If the observed transient response then persists, it is a clear indication that it is simply a change in absorptance of the metallic layers due to the non-equilibrium electron distribution induced by ultrafast laser-induced heating. Such a contribution can in measurements of ultrafast demagnetization easily be filtered out by subtracting the (field-dependent) signals from "up" and "down" magnetization as discussed above.

5.3 Conclusion

In summary, the two optical experiments for transient magnetization dynamics in NiO and spin transport through NiO have been described in this chapter. Regarding the first experiment, no transient behvaiour of an OOP magnetization component could be observed. The current hypothesis is that the AFM is in a multidomain state and that the presence of many domain walls in the area affected by the optical spin current leads to enhanced damping of any collective dynamics, which means that the estimated induced magnetization $m_z =\sim 0.01 - 0.1$ calculated in chapter 3 may be an overestimation. In order to gather more understanding of the deposited NiO films, more information on the precise domain structure, the way it influences the presented measurements and the way it can be manipulated must be acquired.

When the multilayer system for spin transport measurements was measured in the TRFE setup, it was found that a distinct transient response was still present in the signal. In the absence of an OOP component of the magnetization (see section 4.2.2) in these stacks, the measured signal is expected to be a transient reflectance effect of the metallic system upon laser heating. The typical e-p relaxation timescale based on a 2-exponential fit gave a value of 391 ± 4 fs, which is typical for this parameter in laser-induced heated metallic systems. To unequivocally confirm whether this is indeed a response of the metallic system and not a magnetic artefact from the IP layers, the same stack should be repeated, but with the magnetic layers replaced by NMs.

Chapter 6

Conclusion & outlook

This thesis revolved around the manipulation of AFMs through optically excited spin current pulses in magnetic multilayer samples. This was approached both from a numerical point of view, as well as an experimental point of view. Throughout the previous three chapters, the main numerical and experimental results obtained for this purpose have been presented. In this chapter the reader will be provided with an overview of the most important conclusions (section 6.1) of this thesis. Finally, in sections 6.2 and 6.3 some more detailed light is shed on proposal for modelling S-domains in AFMs, as well as a simple tool to start experiments on antiferromagnetic domain visualisation respectively.

6.1 Conclusions

Numerical description

In order to describe the generation and transport of spin angular momentum in the metallic multilayer systems, a diffusive description of this transport was presented in chapter 3. The presented formalism can be used to compute estimates of the spin current injected into the AFM for arbitrary stack geometries, which can in turn be used to calculate the dynamic response of the AFM into which the optical spin current is injected.

Described by a simple macrospin, the response of the antiferromagnetic order parameter to the spin current pulse was calculated. This suggested that if a mono-domain state could be excited coherently, the induced transient magnetization should be large enough to be measured in the optical experiments presented in chapter 5. The model can potentially also be used to predict the magnetic response of noncollinear ferromagnetic systems, which could serve as a test case to test the validity of the diffusive description in these kind of quantitative estimates.

Sample growth and characterization

For the purpose of these same optical experiments, multilayer stacks were designed. These were grown through sputter deposition and characterized in chapter 4. There were several aspects of importance in the stack design of these systems which consisted basically of three essential components: the AFM under investigation (NiO), the NM that decouples the magnetic layers and transmits spin currents(Cu), and the FM ([Co/Ni]) multilayer that generates

the spin currents. First, the antiferromagnetic properties of the NiO films were confirmed through two different experiments:

- Raman spectroscopy revealed the specific antiferromangetic 2-magnon peak at the expected frequency, which is a fingerprint of the long range magnetic order in NiO. Furthermore, as the temperature approached the Neél temperature, the peak intensity was found to decay to the point where it was no longer measurable, consistent with the phase transition from antiferromagnetic to paramagnetic.

- In [111]-NiO/Co stacks, a distinct exchange bias shift of 6.8 mT was observed, consistent with earlier reported values in literature for the exchange bias in these systems.

Since the antiferromagnetic order is strongly linked to the crystal structure in NiO, this property of the NiO films was also investigated through XRD and LEED:

- The XRD signal corresponding to the different NiO textures was fit with a Lorentzian lineshape. It was found that the grown NiO films had the same texture as that of the single crystal MgO substrate. The peak in the diffractogram corresponding to this texture was two orders of magnitude larger than that of other textures (such as [001]-textures when growing on a [111]-MgO substrate). This suggests that the crystallographic texture of the NiO films is strongly influenced via the lattice-matched crystalline MgO substrate. This observation was also supported by the performed LEED measurements.

- By merit of the Scherrer equation, the width of the different texture peaks was coupled to the grain size in the thick NiO films. An estimated typical crystallite size for NiO of roughly 100 nm was found, further supporting the claim that the deposited films are nearly "single crystal," as for these kinds of substrates a typical grain size of around 200 nm is reported in literature. To make this claim more rigorous, further work that can reveal the local crystal structure near the MgO/NiO interface needs to be performed if exact dimensions of the grain size are required.

The next step that was described in the development of the sample growth scheme, was to check the growth of the NM, and FM multilayer. Here distinct behaviour was observed for the polycrystalline NiO grown at RT for the spin transport experiments, contrary to the crystalline NiO that were grown at high temperature for the transient magnetization dynamics experiments. The conclusions for these two growth schemes are given by:

- The PMA needed in the FM multilayers was not present when the NM/FM stack was grown on polycrystalline NiO grown at RT. A hypothesis for the origin of this observation is provided in section 4.2.2, based on the difference in mobility of sputtered Co atoms on different crystal facets of Cu. However, it still remains an important challenge to understand what drives the absence of PMA in this stack recipe.

- In the NM/FM deposited on crystalline NiO grown at high temperature, PMA was observed in M-H measurements. A coercivity of 50 mT and saturation magnetization of 760 ± 20 kA/m were found for these films which are reasonable values for these kind of FM multilayers.

Further characterization of the Cu surface on which the Co/Ni multilayer is grown for the two different stacks can shed light on the role this interface plays on the Co/Ni multilayer growth. This may include LEED, to compare the crystallinity between the two surfaces, as well as atomic force microscopy to check the roughness of the surface. Finally, it was found that replacing the Cu layer by a Pt layer brings back PMA in the FM multilayer, however due to its large spin orbit interaction and associated high spin flip scattering cross section this material is not suited as a buffer layer in the noncollinear systems under consideration. It may however be interesting to investigate the use of a Pt dusting layer (~ 0.2 nm) to alter the growth dynamics of the Co/Ni multilayer.

Finally, exploratory experiments were shown of using a Pt buffer layer between the NiO film and the crystalline MgO substrate. If the texture of the MgO substrate was adopted by the Pt layer, and also leads to the same textured growth in NiO, the compressive strain from the Pt layer can potentially be used to manipulate the magnetic structure of the AFM. The main conclusion that can be drawn from this work is that, though some of the original MgO texture is still present, the [111]-texture of Pt dominates the XRD spectra that were taken. Further process optimization is required. For instance, the influence of the deposition temperature and thickness of the Pt layer need to be charted out in more detail.

Optical experiments

The designed stacks were investigated in a TRFE-setup to perform the intended optical experiments, as discussed in chapter 5. It is instructive to again separate the conclusions for these separate experiments (i.e. transient magnetizationn in NiO, and spin transport through NiO):

- The first exploratory measurements in the transient magnetization experiments did not show any measurable OOP component of the magnetization in the AFM.

It was hypothesized that this is (partially) related to the small domain structure of the AFM when compared to the diameter of the demagnetizing laser spot (~5µm). In the case of a multidomain state in the AFM, the estimation for the induced magnetization from the model in chapter 2 is no longer reliable since it assumes a monodomain state, which might omit enhanced damping from pinning at domain walls. This combined with the small Faraday rotation ($1-0.1$ µrad) calculated from the model in chapter 3 suggests that the response from the AFMI may be below the noise floor of the used setup. In order to better understand the response of the NiO layer to impinging spin currents, it is pivotal to visualize the domain structure and account for this in the model. Suggestions for the development of experiments that can facilitate this domain visualization will be provided in section 6.3. If the domain size is indeed found to be a limiting factor in exciting measurable spin dynamics in AFMs, steps can be taken to engineer larger domain sizes. These can include field annealing and using different substrates for the NiO film like Pt.

Finally, the transient response to laser-induced heating of the samples intended for the spin transport experiments (i.e. FM/NiO/FM) is discussed;

- Even though no magnetic contrast was measured in the sample for spin transport, a transient response characteristic of the ultrafast heating of the electron system and subsequent redistribution of the heat was observed.

This phenomenon can either be related to the unintended detection of the response of the IP FM layers due to the propogation direction of the laser beam not being entirely perpendicular to the investigated film, or a transient reflectance effect induced by the strongly non-equilibrium electron distribution after laser-induced heating. Further research will be needed to identify the nature of the transient behaviour in these multilayers and to what extent it needs to be taken into account when measuring TRFE.

6.2 Modelling antiferromagnetic domains

The presented model for spin transport and dynamics provides reasonable estimates of the relevant spin currents in the metallic layers, and the dynamic behaviour of the AFM. One important approximation that was made in this section, is the complete neglect of the antiferromagnetic domain structure, which was discussed in section 2.3.1. The reader is reminded that in NiO, two different kinds of domains can be distinguished: T-domains are distinguished by the $\langle 1\,1\,1 \rangle$ stacking axis of the antiferromagnetically coupled FM planes; within these planes the spin can align along three stable IP directions, the S-domains.

In the model described in chapter 3, a monodomain state was assumed, both in terms of T and S-domains. Furthermore, for the approximations made for the equations describing the spin dynamics to be valid, the stacking direction of the FM planes should be parallel to the film normal. This should be the case for growth in the [111]-direction as was done for the experiments described in chapter 5. To improve the model, an interesting next step will be to investigate whether the domain structure can be implemented in the equations of motion. Especially the effect of S-domains and their domain walls is of interest here, as T-domains (contrary to S-domains) can in principle be engineered to be larger than the 5 µm spot size of the laser [8, 59], although this has yet to be shown for the sputtered NiO films used in this thesis.

As a first idea to model the domain structure in the AFM, a system as illustrated in figure 6.1 can be considered. The AFM would here be modelled as a square lattice of S-domains, where in each cell the spin axis in the ferromagnetic planes points randomly across one of the three stable axes S_1, S_2 and S_3. In the simplest image, the domain wall pins the spins at the interface between domains [154]. Neglecting spatially inhomogeneous spin dynamics within a domain with spin axis S_1, the (enhanced) damping in a particular domain α_D can be approximated as:

$$\alpha_D = \alpha_0 + \alpha_i \sum_j 1 - \delta_{S_1,S_j}, \tag{6.1}$$

where α_0 is the intrinsic damping of a mono-domain state, α_i is the damping due to pinning at the interface, and the summation runs over the nearest neighbours of the cell with S_j the stable spin configuration in domain j, i.e. it counts the neighbours that have a different equilibrium easy axis of the Neél parameter. Note that this is a crude approximation, and that for a full description the interaction between the domain wall and the overall dynamics in a domain needs to be developed.

Besides this proposal for the implementation of the domain structure in the NiO film, there are several small ways in which the model could be made more realistic:

- Implementation of the 3-temperature model to investigate fluence dependencies in the model, as this is an interesting tunable parameter in experiments.

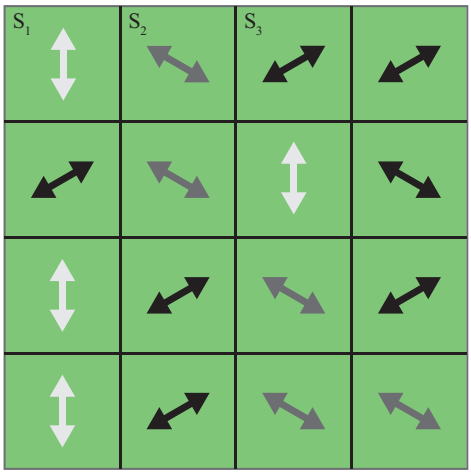

Figure 6.1: Illustration of a model system for the domain structure in antiferromagnets. S-domains are modelled as a square lattice of domains with one of the three possible orientation in these kind of domains. Arrows indicate the Neel parameter easy axis.

- Taking into account spin pumping effects due to the dynamics of the antiferromagnetic order parameter [82].
- Make a more detailed description of the regime (ballisitc, super-diffusive, diffusive) in which spin transport takes place.

6.3 Domain visualization

Knowledge about the domain structure in AFMs is invaluable for proper analysis of the experiments performed in this thesis. Recently Xu et al. demonstrated the use of magneto-optical birefringence induced by the contraction along the stacking direction of the FM planes to image domains [58]. This birefringent effect can be measured as a rotation angle of the polarization of the light, similar to the Faraday rotation discussed in section 2.4. The envisioned setup for measuring this effect is shown in figure 6.2. It is very similar to the MOKE and TRFE setups discussed in sections 2.4 and 5.1 respectively. A continuous-wave or pulsed laser is focused on the sample and picks up a rotation depending on the angle between the propagation direction of the light and the optical axis of the antiferromagnetic domain.

By moving the sample with respect to the beam position a map of the birefringent effect can in principle be produced which translates to the magnetic structure of the NiO film. The translation stage to which the sample holder was attached in the work in this thesis has a resolution of well under 1 µm, hence suggesting that typical NiO domains can be resolved in this way [58]. This would imply that the HALO-objective that was used in this thesis, with which a spot size of 5-10 µm could be achieved, has to be replaced with an objective lens that can also reach this 1 µm resolution. As a starting point for developing these kind of experiments simple MgO/NiO/Pt stacks can be characterized. This way it can be tested whether the broad-field, reflection-based measurement geometry of Xu translates to the scanning microscopy method described in this section. If this method does not yield results, second harmonic generation measurements may need to be considered as an optical way to visualize the domains in NiO.

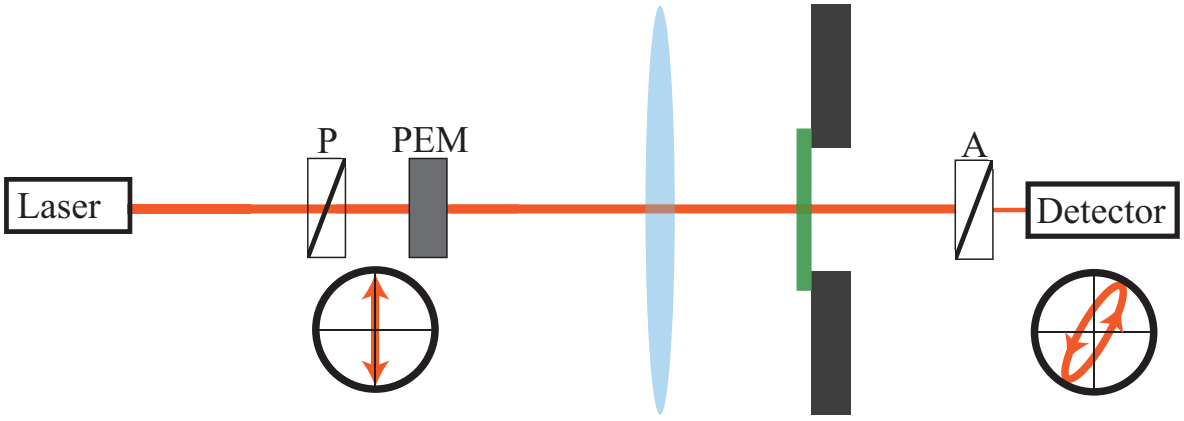

Figure 6.2: Transmission setup intended for antiferromagnetic domain visualisation. P= polarizer, PEM= photo-elastic modulator, A = analyser. Polarization states after the first polarizer and after the sample are shown in the left and right circles respectively.

6.4 Future applications

This thesis has been able to address several first steps in the implementation of the AFMI NiO, including: the presentation of a simple formalism to start numerically estimating the response of the AFM to optical spin pulses, demonstration of a fabrication procedure to implement NiO in the noncollinear system, and the exploratory characterization of these magnetic multilayer stacks in a TRFE setup. Even though plenty of challenges still remain, it is instructive to move the focus to the horizon and consider the end goal in terms of experiments on these systems.

When the experiments described in this thesis work, the described system can be used to investigate the spin dyanmics of many different types of AFM(I)s to optical spin current excitation. As discussed in the introduction is that an entire experiment of excitation of spin current excitation and detection of the dynamic response can be measured in one sample, bypassing the need for a THz radiation source or complicated lithography-based fabrication steps. The magnetic multilayer stack can then serve as an ideal environment to investigate the dynamic behviour of thin films of NiO in the case of FM/NM/AFM stack geometries, as with the sub-ps resolution of the time-resolve measurements that can be performed nowadays, even the ultrafast dynamics of AFMs can be resolved in ways electrical measurements will not be able to emulate. This can in turn provide valuable insight was interactions (anisotropy, indirect exchange, pinning effects) influence the dynamics primarily and from that provide perspective on their applicability in a technological context.

Similarly, the use of sputter deposited NiO films as a spin transport layer, as in the FM/AFM/FM stacks, can potentially replace metallic spacer layers if the spin current attenuation is low enough and the NiO/FM interface is sufficiently efficient at transmitting spin currents. Although this research is still at a very early stage, the fact that spin current transmission is already possible for polycrystalline films [128], the first experiments to test the use of the sputtered NiO films for this purpose can be performed as soon as the issue with absent PMA is fixed.

Bibliography

[1] Nobel Prize organisation. `https://www.nobelprize.org/prizes/physics/1970/neel/facts/`. [Online; accessed 29-january-2019].

[2] L. E. F. Néel. Magnetism and the local molecular field. *Nobel Lectures, vol. Physics 1963–1970*, pages 318–341, 1970.

[3] W. L. Roth. The magnetic structure of Co_3O_4. *Journal of Physics and Chemistry of Solids*, 25(1):1 – 10, 1964.

[4] J. D. Cashion, A. H. Cooke, J. F. B. Hawkes, M. J. M. Leask, T. L. Thorp, and M. R. Wells. Magnetic properties of antiferromagnetic $GdAlO_3$. *Journal of Applied Physics*, 39(2):1360–1361, 1968.

[5] R. M. Moon. Antiferromagnetism in V_2O_3. *Phys. Rev. Lett.*, 25:527–529, Aug 1970.

[6] W. C. Koehler, R. M. Moon, A. L. Trego, and A. R. Mackintosh. Antiferromagnetism in chromium alloys. i. neutron diffraction. *Phys. Rev.*, 151:405–413, Nov 1966.

[7] S. Nomura, R. Santoro, J. Fang, and R. Newnham. Antiferromagnetism in cobalt orthosilicate. *Journal of Physics and Chemistry of Solids*, 25(8):901 – 905, 1964.

[8] W. L. Roth. Neutron and optical studies of domains in NiO. *Journal of Applied Physics*, 31(11):2000–2011, 1960.

[9] M. T. Hutchings and E. J. Samuelsen. Measurement of spin-wave dispersion in NiO by inelastic neutron scattering and its relation to magnetic properties. *Physical Review B*, 6(9):3447, 1972.

[10] S. Bhatti, R. Sbiaa, A Hirohata, H Ohno, S. Fukami, and S. N. Piramanayagam. Spintronics based random access memory: a review. *Materials Today*, 20(9):530 – 548, 2017.

[11] Kyoto University. `https://www.tlo-kyoto.co.jp/english/patent/post-341.html`. [Online; accessed 7-february-2020].

[12] J. Zelezný, P. Wadley, K. Olejník, A. Hoffmann, and H. Ohno. Spin transport and spin torque in antiferromagnetic devices. *Nature Physics*, 14(3):220–228, 2018.

[13] P. Nemec, M. Fiebig, T. Kampfrath, and A. V. Kimel. Antiferromagnetic opto-spintronics. *Nature Physics*, 14(3):229–241, 2018.

[14] T. Jungwirth, X. Marti, P. Wadley, and J. Wunderlich. Antiferromagnetic spintronics. *Nature Nanotechnology*, 11(3):231–241, 2016.

[15] S. Cheong, M. Fiebig, W. Wu, L. Chapon, and V. Kiryukhin. Seeing is believing: visualization of antiferromagnetic domains. *npj Quantum Materials*, 5(1):3, 2020.

[16] A. Pashkin, A. Sell, T. Kampfrath, and R. Huber. Electric and magnetic terahertz nonlinearities resolved on the sub-cycle scale. *New Journal of Physics*, 15(6):065003, jun 2013.

[17] T. Satoh, S. Cho, R. Iida, T. Shimura, K. Kuroda, H. Ueda, Y. Ueda, B. A. Ivanov, F. Nori, and M. Fiebig. Spin oscillations in antiferromagnetic NiO triggered by circularly polarized light. *Physical review letters*, 105(7):077402, 2010.

[18] C. Tzschaschel, K. Otani, R. Iida, T. Shimura, H. Ueda, S. Günther, M. Fiebig, and T. Satoh. Ultrafast optical excitation of coherent magnons in antiferromagnetic NiO. *Physical Review B*, 95(17):174407, 2017.

[19] R. Cheng, M. W. Daniels, J. Zhu, and D. Xiao. Ultrafast switching of antiferromagnets via spin-transfer torque. *Physical Review B*, 91(6):064423, 2015.

[20] A. V. Kimel, B. A. Ivanov, R. V. Pisarev, P. A. Usachev, A. Kirilyuk, and Th. Rasing. Inertia-driven spin switching in antiferromagnets. *Nature Physics*, 5(10):727–731, 2009.

[21] M. Fiebig, D. Fröhlich, Th. Lottermoser, V. V. Pavlov, R. V. Pisarev, and H-J. Weber. Second harmonic generation in the centrosymmetric antiferromagnet NiO. *Physical review letters*, 87(13):137202, 2001.

[22] R. D. Johnson, P. Barone, A. Bombardi, R. J. Bean, S. Picozzi, P. G. Radaelli, Y. S. Oh, S.-W. Cheong, and L. C. Chapon. X-ray imaging and multiferroic coupling of cycloidal magnetic domains in ferroelectric monodomain $BiFeO_3$. *Phys. Rev. Lett.*, 110:217206, May 2013.

[23] S. Dutta, S. Chang, N. Kani, D. E. Nikonov, S. Manipatruni, I. A. Young, and A. Naeemi. Non-volatile clocked spin wave interconnect for beyond-cmos nanomagnet pipelines. *Scientific reports*, 5:9861, 2015.

[24] H. Wang, C. Du, P. C. Hammel, and F. Yang. Antiferromagnonic spin transport from $Y_3Fe_5O_{12}$ into NiO. *Physical review letters*, 113(9):097202, 2014.

[25] R. Lebrun, A. Ross, S. A. Bender, A. Qaiumzadeh, L. Baldrati, J. Cramer, A. Brataas, R. A. Duine, and M. Kläui. Tunable long-distance spin transport in a crystalline antiferromagnetic iron oxide. *Nature*, 561(7722):222, 2018.

[26] T. Numata, H. Hayashi, H. Sakimura, and K. Ando. Parametric spin pumping into an antiferromagnetic insulator. *Physical Review B*, 100(14):144430, 2019.

[27] P. R. T. Ribeiro, F. L. A. Machado, M. Gamino, A. Azevedo, and S. M. Rezende. Spin seebeck effect in antiferromagnet nickel oxide in wide ranges of temperature and magnetic field. *Physical Review B*, 99(9):094432, 2019.

[28] Y. Cheng, R. Zarzuela, J. T. Brangham, A. J. Lee, S. White, P. C. Hammel, Y. Tserkovnyak, and F. Yang. Nonsinusoidal angular dependence of fmr-driven spin current across an antiferromagnet in $Y_3Fe_5O_{12}$/NiO/Pt trilayers. *Physical Review B*, 99(6):060405, 2019.

[29] Q. Li, M. Yang, C. Klewe, P. Shafer, A. T. N'Diaye, D. Hou, T. Y. Wang, N. Gao, E. Saitoh, C. Hwang, R. J. Hicken, J. Li, E. Arenholz, and Z. Q. Qiu. Coherent ac spin current transmission across an antiferromagnetic CoO insulator. *Nature Communications*, 10(1):5265, 2019.

[30] G. Tatara and C. O. Pauyac. Theory of spin transport through an antiferromagnetic insulator. *Physical Review B*, 99(18):180405, 2019.

[31] K. Shen. Pure spin current in antiferromagnetic insulators. *Physical Review B*, 100(9):094423, 2019.

[32] S. M. Rezende, A. Azevedo, and R. L. Rodríguez-Suárez. Introduction to antiferromagnetic magnons. *Journal of Applied Physics*, 126(15):151101, 2019.

[33] T. Kampfrath, A. Sell, G. Klatt, A. Pashkin, S. Mährlein, T. Dekorsy, M. Wolf, M. Fiebig, A. Leitenstorfer, and R. Huber. Coherent terahertz control of antiferromagnetic spin waves. *Nature Photonics*, 5(1):31, 2011.

[34] A. J. Schellekens, K. C. Kuiper, R. R. J. C. De Wit, and B. Koopmans. Ultrafast spin-transfer torque driven by femtosecond pulsed-laser excitation. *Nature communications*, 5:4333, 2014.

[35] M. L. M. Lalieu. Femtomagnetism meets spintronics and magnonics. 2019.

[36] A. J. Schellekens. *Manipulating spins: novel methods for controlling magnetization dynamics on the ultimate timescale*. PhD thesis, PhD thesis, Eindhoven University of Technology, 2014.

[37] J. M. D. Coey. *Magnetism and magnetic materials*. Cambridge university press, 2010.

[38] D. J. Griffiths and D. F. Schroeter. *Introduction to quantum mechanics*. Cambridge University Press, 2018.

[39] E. C. Stoner and E. P. Wohlfarth. A mechanism of magnetic hysteresis in heterogeneous alloys. *IEEE Transactions on Magnetics*, 27(4):3475–3518, July 1991.

[40] A. Kohn, A. Kovács, R. Fan, G. J. McIntyre, R. C. C. Ward, and J. P. Goff. The antiferromagnetic structures of $IrMn_3$ and their influence on exchange-bias. *Scientific reports*, 3:2412, 2013.

[41] S. Manz, M. Matsubara, T. Lottermoser, J. Büchi, A. Iyama, T. Kimura, D. Meier, and M. Fiebig. Reversible optical switching of antiferromagnetism in $TbMnO_3$. *Nature Photonics*, 10(10):653, 2016.

[42] J. Milano, L. B. Steren, and M. Grimsditch. Effect of dipolar interaction on the antiferromagnetic resonance spectra of NiO. *Physical review letters*, 93(7):077601, 2004.

[43] J. Milano and M. Grimsditch. Magnetic field effects on the NiO magnon spectra. *Physical Review B*, 81(9):094415, 2010.

[44] Z. Wang, S. Kovalev, N. Awari, M. Chen, S. Germanskiy, B. Green, J-C. Deinert, T. Kampfrath, J. Milano, and M. Gensch. Magnetic field dependence of antiferromagnetic resonance in NiO. *Applied Physics Letters*, 112(25):252404, 2018.

[45] W. L. Roth and G. A. Slack. Antiferromagnetic structure and domains in single crystal NiO. *Journal of Applied Physics*, 31(5):S352–S353, 1960.

[46] H. A. Kramers. L'interaction entre les atomes magnétogènes dans un cristal paramagnétique. *Physica*, 1(1-6):182–192, 1934.

[47] J. Kanamori. Superexchange interaction and symmetry properties of electron orbitals. *Journal of Physics and Chemistry of Solids*, 10(2-3):87–98, 1959.

[48] P. W. Anderson. New approach to the theory of superexchange interactions. *Physical Review*, 115(1):2, 1959.

[49] W. L. Roth. Magnetic structures of MnO, FeO, CoO, and NiO. *Physical Review*, 110(6):1333, 1958.

[50] J. B. Goodenough. An interpretation of the magnetic properties of the perovskite-type mixed crystals $La_{1-x}Sr_xCoO_3$ - λ. *Journal of Physics and Chemistry of Solids*, 6(2):287 – 297, 1958.

[51] M. Fraune, U. Rüdiger, G. Güntherodt, S. Cardoso, and P. Freitas. Size dependence of the exchange bias field in NiO/Ni nanostructures. *Applied Physics Letters*, 77(23):3815–3817, 2000.

[52] A. Hochstrat, C. H. Binek, and W. Kleemann. Training of the exchange-bias effect in NiO-Fe heterostructures. *Physical Review B*, 66(9):092409, 2002.

[53] S. A. Makhlouf, H. Al-Attar, and R. H. Kodama. Particle size and temperature dependence of exchange bias in NiO nanoparticles. *Solid State Communications*, 145(1-2):1–4, 2008.

[54] Y. Wang, D. Zhu, Y. Yang, K. Lee, R. Mishra, G. Go, S. Oh, D. Kim, K. Cai, E. Liu, et al. Magnetization switching by magnon-mediated spin torque through an antiferromagnetic insulator. *Science*, 366(6469):1125–1128, 2019.

[55] H. P. Rooksby. A note on the structure of nickel oxide at subnormal and elevated temperatures. *Acta Crystallographica*, 1(4):226–226, 1948.

[56] G. A. Slack. Crystallography and domain walls in antiferromagnetic NiO crystals. *Journal of Applied Physics*, 31(9):1571–1582, 1960.

[57] T. Yamada, S. Saito, and Y. Shimomura. Magnetic anisotropy, magnetostriction, and magnetic domain walls in NiO. ii. experiment. *Journal of the Physical Society of Japan*, 21(4):672–680, 1966.

[58] J. Xu, C. Zhou, M. Jia, D. Shi, C. Liu, H. Chen, G. Chen, G. Zhang, Y. Liang, J. Li, W. Zhang, and Y. Wu. Imaging antiferromagnetic domains in nickel oxide thin films by optical birefringence effect. *Phys. Rev. B*, 100:134413, Oct 2019.

[59] I. Sänger, V. V. Pavlov, M. Bayer, and M. Fiebig. Distribution of antiferromagnetic spin and twin domains in NiO. *Physical Review B*, 74(14):144401, 2006.

[60] S. S. L. Zhang and S. Zhang. Spin convertance at magnetic interfaces. *Physical Review B*, 86(21):214424, 2012.

[61] S. S. L. Zhang and S. Zhang. Magnon mediated electric current drag across a ferromagnetic insulator layer. *Physical review letters*, 109(9):096603, 2012.

[62] F. L. A. Machado, P. R. T. Ribeiro, J. Holanda, R. L. Rodríguez-Suárez, A. Azevedo, and S. M. Rezende. Spin-flop transition in the easy-plane antiferromagnet nickel oxide. *Physical Review B*, 95(10):104418, 2017.

[63] L. A. L. E. Landau and E. Lifshitz. On the theory of the dispersion of magnetic permeability in ferromagnetic bodies. In *Perspectives in Theoretical Physics*, pages 51–65. Elsevier, 1992.

[64] S. M. Rezende, R. L. Rodríguez-Suárez, and A. Azevedo. Diffusive magnonic spin transport in antiferromagnetic insulators. *Physical Review B*, 93(5):054412, 2016.

[65] H. Wang, C. Du, P. C. Hammel, and F. Yang. Spin transport in antiferromagnetic insulators mediated by magnetic correlations. *Phys. Rev. B*, 91:220410, Jun 2015.

[66] E. Hecht. *Optics*. Pearson, 2015.

[67] H. Piller. Chapter 3 faraday rotation. volume 8 of *Semiconductors and Semimetals*, pages 103 – 179. Elsevier, 1972.

[68] E. Beaurepaire, J. Merle, A. Daunois, and J. Bigot. Ultrafast spin dynamics in ferromagnetic nickel. *Physical review letters*, 76(22):4250, 1996.

[69] M. Battiato, K. Carva, and P. M. Oppeneer. Superdiffusive spin transport as a mechanism of ultrafast demagnetization. *Physical review letters*, 105(2):027203, 2010.

[70] G. Choi, B. Min, K. Lee, and D. G. Cahill. Spin current generated by thermally driven ultrafast demagnetization. *Nature communications*, 5:4334, 2014.

[71] W. S. Fann, R. Storz, H. W. K. Tom, and J. Bokor. Electron thermalization in gold. *Physical Review B*, 46(20):13592, 1992.

[72] C. Sun, F. Vallée, L. H. Acioli, E. P. Ippen, and J. G. Fujimoto. Femtosecond-tunable measurement of electron thermalization in gold. *Physical Review B*, 50(20):15337, 1994.

[73] G. Malinowski, F. Dalla Longa, J. H. H. Rietjens, P. V. Paluskar, R. Huijink, H. J. M. Swagten, and B. Koopmans. Control of speed and efficiency of ultrafast demagnetization by direct transfer of spin angular momentum. *Nature Physics*, 4(11):855, 2008.

[74] M. Battiato, K. Carva, and P. M. Oppeneer. Theory of laser-induced ultrafast superdiffusive spin transport in layered heterostructures. *Phys. Rev. B*, 86:024404, Jul 2012.

[75] A. Melnikov, I. Razdolski, T. O. Wehling, E. Th. Papaioannou, V. Roddatis, P. Fumagalli, O. Aktsipetrov, A. I. Lichtenstein, and U. Bovensiepen. Ultrafast transport of laser-excited spin-polarized carriers in Au/Fe/MgO(001). *Phys. Rev. Lett.*, 107:076601, Aug 2011.

[76] J. Železnỳ, Y. Zhang, C. Felser, and B. Yan. Spin-polarized current in noncollinear antiferromagnets. *Physical review letters*, 119(18):187204, 2017.

[77] M. L. M. Lalieu, P. L. J. Helgers, and B. Koopmans. Absorption and generation of femtosecond laser-pulse excited spin currents in noncollinear magnetic bilayers. *Physical Review B*, 96(1):014417, 2017.

[78] J. F. Janak. Accurate computation of the density of states of copper. *Physics Letters A*, 28(8):570–571, 1969.

[79] M. D. Stiles, J. Xiao, and A. Zangwill. Phenomenological theory of current-induced magnetization precession. *Physical Review B*, 69(5):054408, 2004.

[80] T. Valet and A. Fert. Theory of the perpendicular magnetoresistance in magnetic multilayers. *Physical Review B*, 48(10):7099, 1993.

[81] R. Cheng, J. Xiao, Q. Niu, and A. Brataas. Spin pumping and spin-transfer torques in antiferromagnets. *Physical review letters*, 113(5):057601, 2014.

[82] A. Qaiumzadeh, H. Skarsvåg, C. Holmqvist, and A. Brataas. Spin superfluidity in biaxial antiferromagnetic insulators. *Physical review letters*, 118(13):137201, 2017.

[83] M. W. Daniels, W. Guo, G. M. Stocks, D. Xiao, and J. Xiao. Spin-transfer torque induced spin waves in antiferromagnetic insulators. *New Journal of Physics*, 17(10):103039, 2015.

[84] S. Yakata, Y. Ando, T. Miyazaki, and S. Mizukami. Temperature dependences of spin-diffusion lengths of Cu and Ru layers. *Japanese journal of applied physics*, 45(5R):3892, 2006.

[85] G. R. Hoogeboom, A. Aqeel, T. Kuschel, T. T. M. Palstra, and B. J. van Wees. Negative spin hall magnetoresistance of Pt on the bulk easy-plane antiferromagnet NiO. *Applied Physics Letters*, 111(5):052409, 2017.

[86] A. C. H. Rowe, I. Zhaksylykova, G. Dilasser, Y. Lassailly, and J. Peretti. Polarizers, optical bridges, and sagnac interferometers for nanoradian polarization rotation measurements. *Review of Scientific Instruments*, 88(4):043903, 2017.

[87] MTI Corporation. `https://www.mtixtl.com/MG-a-101005S2.aspx`. [Online; accessed 4-november-2019].

[88] MTI Corporation. `https://www.mtixtl.com/MG-c-101005S1.aspx`. [Online; accessed 4-november-2019].

[89] L. C. Bartel and B. Morosin. Exchange striction in NiO. *Physical Review B*, 3(3):1039, 1971.

[90] D. K. Smith and H. R. Leider. Low-temperature thermal expansion of LiH, MgO and CaO. *Journal of Applied Crystallography*, 1(4):246–249, 1968.

[91] F. J. A. Den Broeder, E. Janssen, W. Hoving, and W. B. Zeper. Perpendicular magnetic anisotropy and coercivity of Co/Ni multilayers. *IEEE transactions on magnetics*, 28(5):2760–2765, 1992.

[92] G. H. O. Daalderop, P. J. Kelly, and F. J. A. Den Broeder. Prediction and confirmation of perpendicular magnetic anisotropy in Co/Ni multilayers. *Physical review letters*, 68(5):682, 1992.

[93] M. A. van Spronsen, J. W. M. Frenken, and I. M. N. Groot. Observing the oxidation of platinum. *Nature communications*, 8(1):429, 2017.

[94] B. Chapman. Glow discharge processes, 1980.

[95] J. de la Figuera, J. E. Prieto, C. Ocal, and R. Miranda. Scanning-tunneling-microscopy study of the growth of cobalt on Cu(111). *Phys. Rev. B*, 47:13043–13046, May 1993.

[96] J. J. de Miguel, A. Cebollada, J. M. Gallego, R. Miranda, C. M. Schneider, P. Schuster, and J. Kirschner. Influence of the growth conditions on the magnetic properties of fcc cobalt films: from monolayers to superlattices. *Journal of Magnetism and Magnetic Materials*, 93:1 – 9, 1991.

[97] A.K. Schmid and J. Kirschner. In situ observation of epitaxial growth of Co thin films on Cu(100). *Ultramicroscopy*, 42-44:483 – 489, 1992.

[98] J. Lucassen, F. Kloodt-Twesten, R. Frömter, H. P. Oepen, R. A. Duine, H. J. M. Swagten, B. Koopmans, and R. Lavrijsen. Scanning electron microscopy with polarization analysis for multilayered chiral spin textures. *Applied Physics Letters*, 111(13):132403, 2017.

[99] P. J. Kelly and R. D. Arnell. Magnetron sputtering: a review of recent developments and applications. *Vacuum*, 56(3):159–172, 2000.

[100] M. L. M. Lalieu, R. Lavrijsen, R. A. Duine, and B. Koopmans. Investigating optically excited terahertz standing spin waves using noncollinear magnetic bilayers. *Physical Review B*, 99(18):184439, 2019.

[101] M.L.M. Lalieu, R. Lavrijsen, and B. Koopmans. Integrating all-optical switching with spintronics. *Nature communications*, 10(1):110, 2019.

[102] F. C. Ummelen, T. Lichtenberg, H. J. M. Swagten, and B. Koopmans. Controlling skyrmion bubble confinement by dipolar interactions. *Applied Physics Letters*, 115(10):102402, 2019.

[103] Y. Lu, W. Hwang, J. S. Yang, and H. C. Chuang. Properties of nickel oxide thin films deposited by rf reactive magnetron sputtering. *Thin Solid Films*, 420:54–61, 2002.

[104] W. D. Sproul. Very high rate reactive sputtering of TiN, ZrN and HfN. *Thin Solid Films*, 107(2):141–147, 1983.

[105] B. M. Lairson, M. R. Visokay, R. Sinclair, S. Hagstrom, and B. M. Clemens. Epitaxial Pt (001), Pt (110), and Pt (111) films on MgO (001), MgO (110), MgO (111), and Al_2O_3 (0001). *Applied physics letters*, 61(12):1390–1392, 1992.

[106] M. J. Carey, F. E. Spada, A. E. Berkowitz, W. Cao, and G. Thomas. Preparation and structural characterization of sputtered CoO, NiO, and $Ni_{0.5}Co_{0.5}O$ thin epitaxial films. *Journal of materials research*, 6(12):2680–2687, 1991.

[107] M. W. Roberts and R. St. C. Smart. The defect structure of nickel oxide surfaces as revealed by photoelectron spectroscopy. *Journal of the Chemical Society, Faraday Transactions 1: Physical Chemistry in Condensed Phases*, 80(11):2957–2968, 1984.

[108] A. F. Carley, S. D. Jackson, J. N. O'shea, and M. W. Roberts. The formation and characterisation of Ni^{3+}—an x-ray photoelectron spectroscopic investigation of potassium-doped Ni (110)–o. *Surface science*, 440(3):L868–L874, 1999.

[109] L. M. Moroney, R. St. C. Smart, and M. W. Roberts. Studies of the thermal decomposition of β NiO (OH) and nickel peroxide by x-ray photoelectron spectroscopy. *Journal of the Chemical Society, Faraday Transactions 1: Physical Chemistry in Condensed Phases*, 79(8):1769–1778, 1983.

[110] A. P. Grosvenor, M. C. Biesinger, R. St. C. Smart, and N. S. McIntyre. New interpretations of xps spectra of nickel metal and oxides. *Surface Science*, 600(9):1771–1779, 2006.

[111] D. R. Vij. *Handbook of applied solid state spectroscopy*. Springer Science & Business Media, 2007.

[112] C. Davisson and L. H. Germer. The scattering of electrons by a single crystal of nickel. *Nature*, 119(2998):558, 1927.

[113] M. A. Vanhove, W. H. Weinberg, and C. Chan. *Low-energy electron diffraction: experiment, theory and surface structure determination*, volume 6. Springer Science & Business Media, 2012.

[114] M. G. Lagally and J. A. Martin. Instrumentation for low-energy electron diffraction. *Review of scientific instruments*, 54(10):1273–1288, 1983.

[115] K. Oura, M. Katayama, A. V. Zotov, V. G. Lifshits, and A. A. Saranin. Elementary processes at surfaces i. adsorption and desorption. In *Surface Science*, pages 295–323. Springer, 2003.

[116] X. Zhou, F. Matthes, D. E. Bürgler, and C. M. Schneider. Magnetic surface domain imaging of uncapped epitaxial FeRh (001) thin films across the temperature-induced metamagnetic transition. *AIP Advances*, 6(1):015211, 2016.

[117] [Substrate LEED measurement performed by Ir. C. F. Schippers.].

[118] C. Kittel et al. *Introduction to solid state physics*, volume 8. Wiley New York, 1976.

[119] A. L. Patterson. The scherrer formula for x-ray particle size determination. *Phys. Rev.*, 56:978–982, Nov 1939.

[120] H. P. Klug and L. E. Alexander. *X-Ray Diffraction Procedures: For Polycrystalline and Amorphous Materials, 2nd Edition*. 1974.

[121] J. I. Langford and A. J. C. Wilson. Scherrer after sixty years: A survey and some new results in the determination of crystallite size. *Journal of Applied Crystallography*, 11(2):102–113, Apr 1978.

[122] E. Carrasco, M. A. Brown, M. Sterrer, H. Freund, K. Kwapien, M. Sierka, and J. Sauer. Thickness-dependent hydroxylation of MgO (001) thin films. *The Journal of Physical Chemistry C*, 114(42):18207–18214, 2010.

[123] C. S. Fadley and D. A. Shirley. Multiplet splitting of metal-atom electron binding energies. *Physical Review A*, 2(4):1109, 1970.

[124] H.W. Nesbitt, D. Legrand, and G. M. Bancroft. Interpretation of Ni2p xps spectra of Ni conductors and Ni insulators. *Physics and Chemistry of Minerals*, 27(5):357–366, 2000.

[125] S. Oswald and W. Brückner. Xps depth profile analysis of non-stoichiometric NiO films. *Surface and Interface Analysis: An International Journal devoted to the development and application of techniques for the analysis of surfaces, interfaces and thin films*, 36(1):17–22, 2004.

[126] H. Xi and R. M. White. Theory of the blocking temperature in polycrystalline exchange biased bilayers based on a thermal fluctuation model. *Journal of Applied Physics*, 94(9):5850–5853, 2003.

[127] R. C. Jaklevic, J. Lambe, A. H. Silver, and J. E. Mercereau. Quantum interference effects in josephson tunneling. *Phys. Rev. Lett.*, 12:159–160, Feb 1964.

[128] H. D. Chopra, D. X. Yang, P. J. Chen, H. J. Brown, L. J. Swartzendruber, and W. F. Egelhoff. Nature of magnetization reversal in exchange-coupled polycrystalline NiO-Co bilayers. *Phys. Rev. B*, 61:15312–15320, Jun 2000.

[129] R. E. Dietz, G. I. Parisot, and A. E. Meixner. Infrared absorption and raman scattering by two-magnon processes in NiO. *Phys. Rev. B*, 4:2302–2310, Oct 1971.

[130] [Raman spectroscopy measurements performed by Ir. C. F. Schippers.].

[131] T. Moriyama, K. Hayashi, K. Yamada, M. Shima, Y. Ohya, and T. Ono. Intrinsic and extrinsic antiferromagnetic damping in NiO. *Phys. Rev. Materials*, 3:051402, May 2019.

[132] M. M. Lacerda, F. Kargar, E. Aytan, R. Samnakay, B. Debnath, J. X. Li, A. Khitun, R. K. Lake, J. Shi, and A. A. Balandin. Variable-temperature inelastic light scattering spectroscopy of nickel oxide: Disentangling phonons and magnons. *Applied Physics Letters*, 110(20):202406, 2017.

[133] B. Warot, E. Snoeck, J. C. Ousset, M. J. Casanove, S. Dubourg, and J. F. Bobo. Surface morphology of NiO layers on MgO(0 0 1), MgO(1 1 0) and MgO(1 1 1). *Applied Surface Science*, 188(1):151 – 155, 2002. E-MRS SYMPOSIUM M; STRESS AND STRAIN IN HETEROEPITAXY.

[134] H. Willmann, M. Beckers, J. Birch, P. H. Mayrhofer, C. Mitterer, and L. Hultman. Epitaxial growth of Al–Cr–N thin films on MgO(111). *Thin Solid Films*, 517(2):598 – 602, 2008.

[135] B. Hu, Y. Chen, Z. Su, S. Bennett, L. Burns, G. Uddin, K. Ziemer, and V. G. Harris. Magnetocrystalline anisotropy and fmr linewidth of Zr and Zn-doped Ba-hexaferrite films grown on MgO (111). *IEEE Transactions on Magnetics*, 49(7):4234–4237, July 2013.

[136] S. Stanescu, C. Boeglin, A. Barbier, and J.-P. Deville. Growth mode of NiO on Cu(111) studied using scanning tunneling microscopy and surface x-ray diffraction. *Phys. Rev. B*, 67:035419, Jan 2003.

[137] M. C. Biesinger, L. W. M. Lau, A. R. Gerson, and R. St. C. Smart. Resolving surface chemical states in xps analysis of first row transition metals, oxides and hydroxides: Sc, Ti, V, Cu and Zn. *Applied Surface Science*, 257(3):887 – 898, 2010.

[138] M. C. Biesinger. Advanced analysis of copper x-ray photoelectron spectra. *Surface and Interface Analysis*, 49(13):1325–1334, 2017.

[139] X. Li, S. Jiang, J. Zhang, G. Han, Q. Liu, Y. Liu, D. Wang, C. Feng, M. Li, and G. Yu. High post-annealing stability for perpendicular [Co/Ni] multilayers by preventing interfacial diffusion. *Journal of Physics D: Applied Physics*, 49(18):185004, apr 2016.

[140] D. B. Gopman, C. L. Dennis, P. J. Chen, Y. L. Iunin, P. Finkel, M. Staruch, and R. D. Shull. Strain-assisted magnetization reversal in Co/Ni multilayers with perpendicular magnetic anisotropy. *Scientific reports*, 6:27774, 2016.

[141] H. G. Tompkins and J. A. Augis. The oxidation of cobalt in air from room temperature to 467°c. *Oxidation of Metals*, 16(5):355–369, Dec 1981.

[142] M. T. Johnson, R. Coehoorn, J. J. de Vries, N. W. E. McGee, J. aan de Stegge, and P. J. H. Bloemen. Orientational dependence of the oscillatory exchange interaction in Co/Cu/Co. *Phys. Rev. Lett.*, 69:969–972, Aug 1992.

[143] B. P. Tonner, Z.-L. Han, and J. Zhang. Structure of Co films grown on Cu(111) studied by photoelectron diffraction. *Phys. Rev. B*, 47:9723–9731, Apr 1993.

[144] X. Z. Chen, R. Zarzuela, J. Zhang, C. Song, X. F. Zhou, G. Y. Shi, F. Li, H. A. Zhou, W. J. Jiang, F. Pan, and Y. Tserkovnyak. Antidamping-torque-induced switching in biaxial antiferromagnetic insulators. *Phys. Rev. Lett.*, 120:207204, May 2018.

[145] M. A. Langell and M. H. Nassir. Stabilization of NiO (111) thin films by surface hydroxyls. *The Journal of Physical Chemistry*, 99(12):4162–4169, 1995.

[146] K. L. Merkle and David J. Smith. Atomic structure of symmetric tilt grain boundaries in NiO. *Phys. Rev. Lett.*, 59:2887–2890, Dec 1987.

[147] F. Dalla Longa. Laser-induced magnetization dynamics: an ultrafast journey among spins and light pulses. 2008.

[148] L. Guidoni, E. Beaurepaire, and J. Bigot. Magneto-optics in the ultrafast regime: Thermalization of spin populations in ferromagnetic films. *Physical review letters*, 89(1):017401, 2002.

[149] R. W. Schoenlein, W. Z. Lin, J. G. Fujimoto, and G. L. Eesley. Femtosecond studies of nonequilibrium electronic processes in metals. *Physical Review Letters*, 58(16):1680, 1987.

[150] J. Xu, C. Zhou, M. Jia, D. Shi, C. Liu, H. Chen, G. Chen, G. Zhang, Y. Liang, J. Li, et al. Imaging antiferromagnetic domains in nickel-oxide thin films by magneto-optical voigt effect. *arXiv preprint arXiv:1906.06844*, 2019.

[151] A. Ross, R. Lebrun, O. Gomonay, D. A. Grave, A. Kay, L. Baldrati, S. Becker, A. Qaiumzadeh, C. Ulloa, G. Jakob, et al. Propagation length of antiferromagnetic magnons governed by domain configurations. *Nano Letters*, 2020.

[152] J. Hohlfeld, J. G. Müller, S.-S. Wellershoff, and E. Matthias. Time-resolved thermoreflectivity of thin gold films and its dependence on film thickness. *Applied Physics B*, 64(3):387–390, Mar 1997.

[153] N. Del Fatti, C. Voisin, M. Achermann, S. Tzortzakis, D. Christofilos, and F. Vallée. Nonequilibrium electron dynamics in noble metals. *Physical Review B*, 61(24):16956, 2000.

[154] J. Stöhr, A. Scholl, T. J. Regan, S. Anders, J. Lüning, M. R. Scheinfein, H. A. Padmore, and R. L. White. Images of the antiferromagnetic structure of a NiO(100) surface by means of x-ray magnetic linear dichroism spectromicroscopy. *Phys. Rev. Lett.*, 83:1862–1865, Aug 1999.

[155] E. Koch. Exchange mechanisms. *Correlated electrons: from models to materials*, 2:1–31, 2012.

[156] F. Keffer and C. Kittel. Theory of antiferromagnetic resonance. *Phys. Rev.*, 85:329–337, Jan 1952.

[157] R. A. Ballinger and C. A. W. Marshall. Electronic structure of cobalt. *Journal of Physics F: Metal Physics*, 3(4):735, 1973.

[158] A. Tari. *The specific heat of matter at low temperatures*. Imperial Coll., 2003.

[159] D. R. Lide. Handbook of chemistry and physics 84-th edition, 2003.

[160] K. Carva, M. Battiato, D. Legut, and P. M. Oppeneer. Ab initio theory of electron-phonon mediated ultrafast spin relaxation of laser-excited hot electrons in transition-metal ferromagnets. *Phys. Rev. B*, 87:184425, May 2013.

[161] D. Gall. Electron mean free path in elemental metals. *Journal of Applied Physics*, 119(8):085101, 2016.

[162] H. Głowiński, F. Lisiecki, P. Kuświk, J. Dubowik, and F. Stobiecki. Influence of adjacent layers on the damping of magnetization precession in Co_xFe_{100-x} films. *Journal of Alloys and Compounds*, 785:891 – 896, 2019.

Appendix A

Hubbard model image of antiferromagnetism

In order to understand the mechanism that leads to antiferromagnetism in transition metal-oxides like NiO, it is important to understand hopping-mediated exchange. In order to sketch a phenomenological image of this hopping mechanism, a simple Hubbard-type Hamiltonian for the H_2 molecule will be considered. A sketch of the H_2 system is shown in figure A.1.

The system consists of two hydrogen atoms separated by some distance $\boldsymbol{r}$. Each atom has one associated orbital each of which is orthogonal to the other. These orbitals are denoted by ϕ_1 and ϕ_2. These orbitals ϕ_1 and ϕ_2 have associated eigenenergies ϵ_1 and ϵ_2 respectively. When we introduce one electron to this model system, we can define the following tight-binding Hamiltonian $\mathcal{H}_1$, which for the case of two orthogonal s-orbitals becomes a 2x2 matrix:

$$\mathcal{H}_1 = \begin{pmatrix} \epsilon_0 & -t \\ -t & \epsilon_0 \end{pmatrix}, \tag{A.1}$$

where $\epsilon_1 = \epsilon_2 = \epsilon_0$ was assumed, and the positive and real matrix element t was introduced, which represents the possibility for the electron to move between orbitals ϕ_1 and ϕ_2. The quantity t is formally defined as:

$$t = \langle \phi_1 | \, h \, | \phi_2 \rangle \,, \tag{A.2}$$

where h is the one-electron Hamiltonian. The eigenstates $\phi_\pm$ can be found by diagonalizing the Hamiltonian in equation (A.1) and are hence given by:

$$\phi_\pm = \frac{1}{\sqrt{2}}(\phi_1 \pm \phi_2), \tag{A.3}$$

with eigenenergies $\epsilon_{\pm,1} = \epsilon_0 \mp t$. As can be seen from equation (A.3) the eigenstate of the electron is a superposition of the two orbital states associated with the two atoms in the molecule. These states can be represented graphically as $\phi_1 = |\uparrow, -\rangle$ and $\phi_2 = |-, \uparrow\rangle$. This type of notation where left and right of the delimiter represent the occupation of the orbitals ϕ_1 and ϕ_2 will be used as a instructive way to represent the different states which the electrons can occupy. For example, the following state $|\uparrow, \downarrow\rangle$ represents orbital 1 being occupied by one electron with spin up, and orbital occupied by one electron with spin down.

With these definitions and notation conventions in place we will now move on to the more physically interesting case of two electrons. Two critical phenomena that need to be

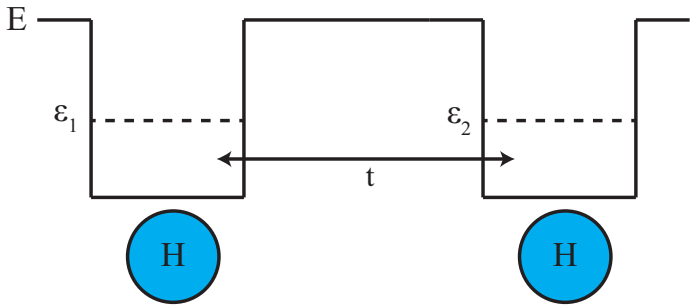

Figure A.1: Simple sketch of the model H_2 system described in this chapter. It shows the energy landscape of the molecule as two square wells associated with the coulomb interaction between the electron and nucleus. Two spatially separated orthogonal orbitals with associated energy levels ϵ_1 and ϵ_2 are considered. There is a finite probability t of the electrons being transferred between the nuclei.

accounted for in the analysis is the Coulomb repulsion between the two like-charged electrons, and the Pauli exclusion principle which imposes that the two electron wavefunction should be antisymmetric with respect to interchange of the two fermions. Taking the latter condition into account we can distinguish between two different states. The first state is an ionic state ϕ_i where the two electrons occupy the same spatial orbital:

$$\phi_\mathrm{i} = |\uparrow\downarrow, 0\rangle\,. \tag{A.4}$$

The second state is a neutral state ϕ_n where the two electrons occupy different spatial orbitals and occupy different spin states:

$$\phi_\mathrm{n} = |\uparrow, \downarrow\rangle\,. \tag{A.5}$$

It can be intuitively understood that ϕ_i is energetically unfavourable due to the increased Coulomb repulsion between the two electrons occupying the same spatial orbital. Based on the two basis states presented in equations (A.4) and (A.5) it is possible to define the two-electron Hamiltonian $\mathcal{H}_2$:

$$\mathcal{H}_2 = \begin{pmatrix} \epsilon_0 + U & 0 & t & -t \\ 0 & \epsilon_0 + U & t & -t \\ t & t & 0 & 0 \\ -t & -t & 0 & 0 \end{pmatrix}, \tag{A.6}$$

where U is the Coulomb repuslion energy penalty that needs to be paid by the system for the two electron system being in the ionic state ϕ_i. The Hamiltonian in equation (A.6) can again be diagonalized to find three eigenvalues in terms of ϵ_0, t and U as

$$\epsilon_\mathrm{i} = 2\epsilon_0 + U, \tag{A.7}$$

and

$$\epsilon_{\pm,2} = 2\epsilon_0 + \frac{1}{2}U \pm \sqrt{4t^2 + \frac{1}{4}U^2}. \tag{A.8}$$

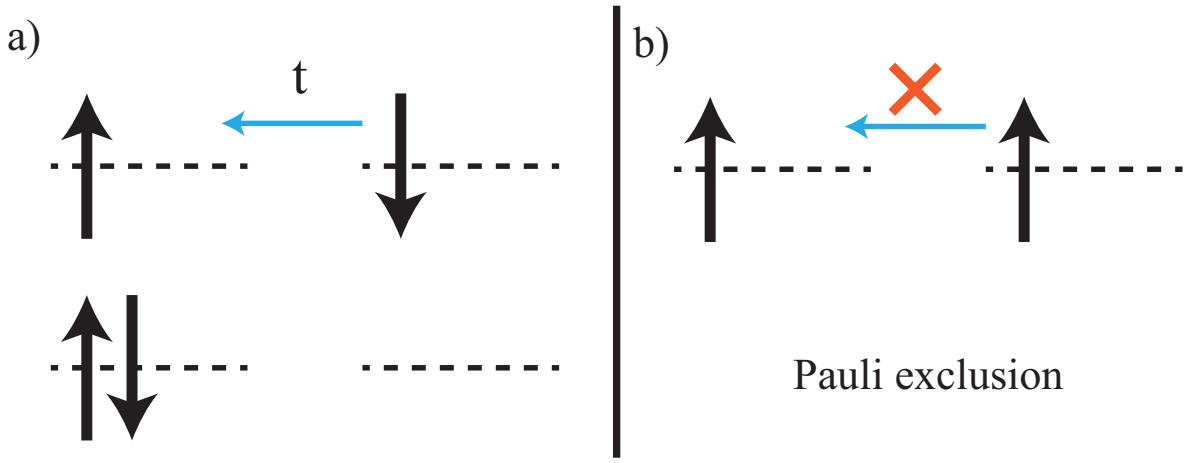

Figure A.2: Simplified illustration of the direct exchange interaction in the H_2 model system. Antiparallel alignment (a) is energetically more favourable than parallel alignment (b), as in the latter case the exclusion principle prohibits hopping of electrons of like spin to the same spatial orbital.

Based on these eigenenergies we can conclude that the ground state has to be the state corresponding to eigenvalue $\epsilon_{-,2}$, $\phi_{-,2}$:

$$\phi_{-,2} = \frac{\left(|\uparrow,\downarrow\rangle - |\downarrow,\uparrow\rangle - \frac{\epsilon_{-,2}}{2t}[|\uparrow\downarrow,0\rangle + |0,\uparrow\downarrow\rangle]\right)}{\sqrt{2 + \epsilon_{-,2}/2t^2}}. \tag{A.9}$$

The result for the ground state of this simple toy box model, as presented in equation (A.9), can be used to obtain phenomenological understanding about hopping between the orbitals in this H_2 molecule, as the qualitative physics allow us to understand the antiferromagnetic coupling observed in transition metal oxides like NiO CoO and MnO. It can be derived that for $U/t << 1$, both electrons move independently through the orbitals leading to metal-like behaviour. For $U/t >> 1$ the system describes the behaviour of well localized electrons, which is more akin to insulating or molecular systems. In these systems band description of the electronic system is no longer appropriate due to the strong correlation between electrons.

It is important to note that as t increases, which depends among other things on the wavefunction overlap between the two orbitals involved in the hopping process (see equation (A.2), the probability of the system occupying a state with both electrons on the same atom becomes increasingly likely. Figure A.2 illustrates graphically why then this tendency for hopping transport opposed to band-like transport favours an antiparallel alignment. In figure A.2a it can be seen that the transfer of an electron from the right orbital to the left is allowed and mediated by the hopping parameter t. On the other hand, in figure A.2b transfer between the two orbitals for the like spins is prohibited by the Pauli exclusion principle.

In a quantum mechanical description this increased possibility for electrons to hop between orbitals can be interpreted as an expansion of the wave function of the electrons towards to other spatial orbital. In this case this orbital is the s-orbital of the other H atom. It should be noted that no quantitative conclusions can be drawn based on the description presented above, however it will serve as a useful framework to understand to origin of superexchange in transition metal oxides like NiO. For a more in-depth treatment of the topic of hopping-

mediated exchange in insulators and semiconductors we refer to more dedicated literature since it is outside the scope of this thesis [155].

Appendix B

AFMR modes NiO

To substantiate why easy-plane antiferromagnets like NiO can sustain a spin current without the application of an electric field, the derivation of the AFMR magnon modes for a generic easy-plane antiferromagnet. The derivation will closely follow earlier work [32, 156], these papers can be considered as a starting point for a more in depth treatment of the derivation presented below.

In this section we will consider an antiferromagnet consisting of two sublattices with magnetizations that are equal in magnitude but antiparallel sublattice magnetizations. The sublattice magnetizations are aligned in the xy-plane with a preferential in-plane alignment along the x-axis. Hence, the z-axis is defined as the hard anisotropy axis. The starting point of the derivation will be the energy density E in the absence of an applied magnetic field:

$$E = \frac{H_{\mathrm{E}}}{M}\boldsymbol{M}_1 \cdot \boldsymbol{M}_2 + \frac{H_{\mathrm{Ax}}}{2M}\left(M_{1\mathrm{z}}^2 + M_{2\mathrm{z}}^2\right) - \frac{H_{\mathrm{Az}}}{2M}\left(M_{1\mathrm{x}}^2 + M_{2\mathrm{x}}^2\right), \tag{B.1}$$

where H_{E} is the exchange field strength, H_{Ax} is the in-plane anisotropy field strength, H_{Az} is the out-of-plane anisotropy field strength and M is the sublattice magnetization. The magnetization dynamics are then given by a Landau-Lifschitz equation [63]. For the AM system this equation, neglecting the often added phenomenological Gilbert damping for now:

$$\frac{\mathrm{d}\boldsymbol{M}_{1,2}}{\mathrm{d}t} = -\gamma \boldsymbol{M}_{1,2} \times \boldsymbol{\nabla}_{\boldsymbol{M}_{1,2}}(E(\boldsymbol{M}_{1,2})), \tag{B.2}$$

where γ is the gyromagnetic ratio. A small perturbation from the ground state (i.e. both sublattices only having their full magnetization along $\hat{\boldsymbol{x}}$ but in opposite directions) is considered:

$$\boldsymbol{M_{1,2}}(t) = \begin{pmatrix} m_{1,2\mathrm{x}} \\ m_{1,2\mathrm{y}} \exp(-i\omega t) \\ m_{1,2\mathrm{z}} \exp(-i\omega t) \end{pmatrix}, \tag{B.3}$$

where ω is the angular precession frequency of the transverse magnetization components. Combining equations (B.1),(B.2) and (B.3), the equations of motion for the transverse magnetization components:

$$i\omega m_{1\mathrm{z}} = -\gamma m_{1\mathrm{y}}(H_{\mathrm{E}} + H_{\mathrm{Ax}}) - \gamma H_{\mathrm{E}} m_{2\mathrm{y}}, \tag{B.4}$$

$$i\omega m_{2\mathrm{z}} = \gamma m_{2\mathrm{y}}(H_{\mathrm{E}} + H_{\mathrm{Ax}}) + \gamma H_{\mathrm{E}} m_{1\mathrm{y}}, \tag{B.5}$$

$$i\omega m_{1\mathrm{y}} = -\gamma m_{1\mathrm{z}}(H_{\mathrm{E}} + H_{\mathrm{Az}} + H_{\mathrm{Ax}}) - \gamma H_{\mathrm{E}} m_{2\mathrm{z}}, \tag{B.6}$$

$$i\omega m_{2\mathrm{y}} = \gamma m_{2\mathrm{z}}(H_{\mathrm{E}} + H_{\mathrm{Az}} + H_{\mathrm{Ax}}) + \gamma H_{\mathrm{E}} m_{1\mathrm{z}}. \tag{B.7}$$

This AFMR frequencies and the eigenvectors of this system of equations can be calculated from the so-called resonance matrix $\mathcal{R}$, which is simply a matrix representation of equations (B.4)-(B.7):

$$\begin{pmatrix} 0 & 0 & -\gamma(H_{\mathrm{Ax}}+H_{\mathrm{E}}) & -\gamma H_{\mathrm{E}} \\ 0 & 0 & \gamma H_{\mathrm{E}} & +\gamma(H_{\mathrm{Ax}}+H_{\mathrm{E}}) \\ -\gamma(H_{\mathrm{Ax}}+H_{\mathrm{Az}}+H_{\mathrm{E}}) & -\gamma H_{\mathrm{E}} & 0 & 0 \\ \gamma H_{\mathrm{E}} & +\gamma(H_{\mathrm{Ax}}+H_{\mathrm{Az}}+H_{\mathrm{E}}) & 0 & 0 \end{pmatrix}, \tag{B.8}$$

The resonance frequencies and eigenvectors can then be calculated and we can distinguish between two branches of solutions. The eigenvalues ω_q with $q = [1..4]$ are then given by:

$$\omega_1 = -\omega_2 = \gamma\sqrt{(H_{\mathrm{Az}}+H_{\mathrm{Ax}})(H_{\mathrm{Az}}+H_{\mathrm{E}})}, \tag{B.9}$$

$$-\omega_3 = \omega_4 = \gamma\sqrt{(H_{\mathrm{Ax}})(H_{\mathrm{Az}}+H_{\mathrm{Ax}}+H_{\mathrm{E}})}. \tag{B.10}$$

We will henceforth consider the positive frequencies to keep the notation concise. These expressions can be simplified by considering that the exchange field H_{E} is much larger than both the anisotropy fields as discussed in the main text (section 2.3):

$$\omega_1 = \gamma\sqrt{H_{\mathrm{E}}(H_{\mathrm{Ax}}+H_{\mathrm{Az}})}, \tag{B.11}$$

$$\omega_4 = \gamma\sqrt{H_{\mathrm{E}}(H_{\mathrm{Ax}})}. \tag{B.12}$$

Here the energetic non-degeneracy of the two modes appears, it can be seen that in the absence of the out-of-plane anisotropy H_{Az}, the two modes will have the same precession frequency. By calculating the eigenvectors of (B.8) the magnetization dynamics belonging to the eigenfrequencies ω_1 and ω_2 can be found as:

$$\begin{pmatrix} m_{1\mathrm{z}} \\ m_{2\mathrm{z}} \\ im_{1\mathrm{y}} \\ im_{2\mathrm{y}} \end{pmatrix}_1 = \begin{pmatrix} -\epsilon_1 \\ \epsilon_1 \\ 1 \\ 1 \end{pmatrix} \tag{B.13}$$

and

$$\begin{pmatrix} m_{1\mathrm{z}} \\ m_{2\mathrm{z}} \\ im_{1\mathrm{y}} \\ im_{2\mathrm{y}} \end{pmatrix}_4 = \begin{pmatrix} -\epsilon_4 \\ -\epsilon_4 \\ -1 \\ 1 \end{pmatrix}, \tag{B.14}$$

respectively, where the trajectory ellipticities $\epsilon_1 = \sqrt{2H_{\mathrm{E}}/H_{\mathrm{Az}}} \approx 55$ and $\epsilon_4 = \sqrt{H_{\mathrm{Ax}}/2H_{\mathrm{E}}} \approx 0.002$ were introduced. Equations (B.13) and (B.14) thus describe two elliptical trajectories. What is important to note is that both modes can carry identical angular momentum independently, but that these two modes have opposite precession directions. However, due to the different energy associated of the modes with the major axes along the in-plane or out-of-plane direction, net spin transport is possible, when the low-energy magnon mode is excited more efficiently than the high-energy mode.

Appendix C

Diffusion model: equations and parameters

C.1 Differential equations

The full dynamic equations for the spin chemical potential $\mu_s = \mu_\uparrow - \mu_\downarrow$ for the Pt, Co/Ni multilayer and Cu layer are given (in order) by:

$$\frac{\partial \mu_s(t,z)}{\partial t} = D_{\mathrm{Pt}} \frac{\partial^2 \mu_s(t,z)}{\partial z^2} - \frac{\mu_s(t,z)}{\tau_{\mathrm{Pt}}}, \tag{C.1}$$

$$\frac{\partial \mu_s(t,z)}{\partial t} = D_{\mathrm{CN}} \frac{\partial^2 \mu_s(t,z)}{\partial z^2} - \frac{\mu_s(t,z)}{\tau_{\mathrm{CN}}} + G_s, \tag{C.2}$$

$$\frac{\partial \mu_s(t,z)}{\partial t} = D_{\mathrm{Cu}} \frac{\partial^2 \mu_s(t,z)}{\partial z^2} - \frac{\mu_s(t,z)}{\tau_{\mathrm{Cu}}}, \tag{C.3}$$

where the generation term G_s is given by:

$$G_s\left[\mathrm{eVps}^{-1}\right] = \frac{1}{4\mu_B N_{\mathrm{CN}}(E_F)}\left[4.6 \cdot 10^4 \exp\left(\frac{-t^2}{0.2}\right) - 1.4 \cdot 10^4 \exp\left(\frac{-(t-0.9)^2}{1}\right)\right], \tag{C.4}$$

where $N_{\mathrm{CN}}(E_F)$ is the density of states of the Co/Ni multilayer, which is estimated by the density of states of the Co layer at the Fermi level. The portion of equation (C.4) between square bracket is a numeric fit to the negative time derivative of the demagnetization measured in a Co/Pt bilayer [70]. The material parameters for the different layers described by this spin diffusion model are presented in table C.1.

As stated in the text, the Co/Ni multilayer is treated as a single layer. The diffusion constant is approximated as $D_{\mathrm{CN}} = \frac{\Lambda_{\mathrm{e,CN}}}{C_{\mathrm{e,CN}}}$, where $\Lambda_{\mathrm{e,CN}}$ is the electronic heat conductivity and $C_{\mathrm{e,CN}}$ is the electronic heat capacity. The spin flip relaxation time can then be estimated as [70]: $\tau_{\mathrm{CN}} = \frac{3D_{\mathrm{CN}}}{v_F^2 a_{\mathrm{sf}}}$, where v_F is the Fermi velocity and a_{sf} is the spin-flip probability. τ_{CN}=0.26 ps is found. The parameters presented for this Co/Ni-layer in table C.1 are weighted averages where appropriate.

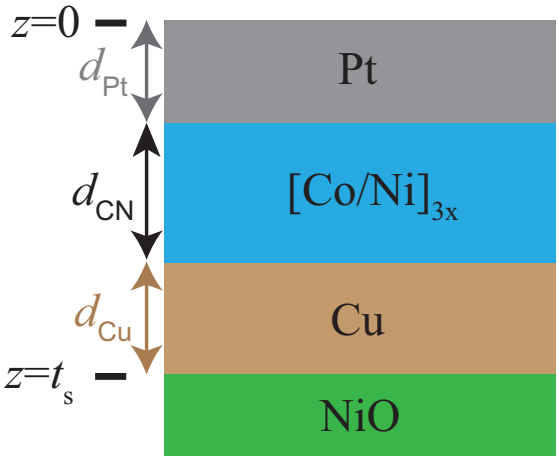

Figure C.1: Layered structure of the modelled system with the relevant thicknesses and z-position of interfaces between different layers.

Table C.1: Spin transport model parameters as used for chapter 3.

Parameter	Unit	Value	Reference
D_{Pt}	$\mathrm{nm^2ps^{-1}}$	500	[70]
τ_{Pt}	ps	0.5	[70]
$\mathrm{d_{Pt}}$	nm	3	N.A.
D_{CN}	$\mathrm{nm^2ps^{-1}}$	500	N.A.
τ_{CN}	ps	0.26	N.A.
$N_{\mathrm{CN}}(E_{\mathrm{F}})$	$\mathrm{eV^{-1}nm^{-3}}$	10	[157]
d_{CN}	nm	2.6	N.A.
$C_{\mathrm{e,CN}}$	$\mathrm{MJm^{-3}K^{-1}}$	0.2	[158]
$\Lambda_{e,CN}$	$\mathrm{Wm^{-1}K^{-1}}$	100	[159]
a_{sf}	nm	0.03	[160]
v_{F}	km/s	255	[161]
D_{Cu}	$\mathrm{nm^2ps^{-1}}$	6500	[70]
τ_{Cu}	ps	25	[70]
$N_{\mathrm{Cu}}(E_{\mathrm{F}})$	$\mathrm{eV^{-1}m^{-3}}$	22.4	[78]

C.2 Boundary conditions

The boundary conditions of the system of equations given above are, given the thicknesses presented in figure C.1:

$$\frac{\partial \mu_s(t,0)}{\partial z} = 0, \tag{C.5}$$

$$\mu_s\left(t, d_{Pt}^-\right) = \mu_s\left(t, d_{Pt}^+\right), \tag{C.6}$$

$$\mu_s\left(t, d_{CN/Cu}^-\right) = \mu_s\left(t, d_{CN/Cu}^+\right), \tag{C.7}$$

$$\mu_s\left(t, d_{Cu/NiO}\right) = -\frac{D}{G_{em}} \frac{\partial \mu_s\left(t, d_{Cu/NiO}\right)}{\partial z}, \tag{C.8}$$

where $d_{CN/Cu} = d_{Pt} + d_{CN}$ is the z-position of the interface of the Co/Ni multilayer and the Cu layer, and $d_{Cu/NiO} = d_{Pt} + d_{CN} + d_{Cu}$ is the z-position of the interface of the Cu and NiO layer.

C.3 Estimation of G_{em}

A back of the envelope estimation of the spin convertance based on experimentally obtained values of the real part of the spin mixing conductance G_r is presented. This quantity defines the efficiency of spin transfer at an arbitrary interface in noncollinear magnetic systems. Referring back to the diffusion model discussed in section 3.1.1, the spin current across the NM/AFMI interface J_s is given by:

$$J_s = eN_{Cu}(E_F)G_{em}\mu_s. \tag{C.9}$$

In terms of the spin mixing conductance, the same spin current can also be defined as:

$$J_s = G_0 V_s G_r, \tag{C.10}$$

where $G_0 = e^2/h$ is the conductance quantum and $V_s = \mu_s/e$ is the spin voltage. Equating equations (C.9) and (C.10) then yields:

$$G_{em} = \frac{G_r}{hN_{Cu}(E_F)}. \tag{C.11}$$

Using table C.1 and $G_r = 48$ nm^{-2} for a NiO/$Co_{25}Fe_{75}$ interface [162], a value of 518 nm/ps is found.

Appendix D

Spin dynamics model: equations and parameters

The full equation of motion for the angle ϕ as described in section 3.1.2 is given by [19]:

$$\ddot{\phi} + \frac{\omega_R^2}{2}\sin(2\phi) + 2\alpha\omega_E\dot{\phi} = 2\omega_E\omega_s(t), \tag{D.1}$$

with

$$\omega_s = \frac{a^3}{d_{NiO}} N_{Cu}(E_F) G_{em} \mu_s \tag{D.2}$$

The values of the parameters ω_a, ω_E, α, a are given in table D.1.

Table D.1: Spin dynamics model parameters as used for the results in chapter 3.

Parameter	Unit	Value	Reference
ω_a	THz	0.001	[19]
ω_E	THz	27.4	[19]
α	N.A.	0.005	[19]
a	nm	0.417	[9]

Appendix E

MgO substrate characterization

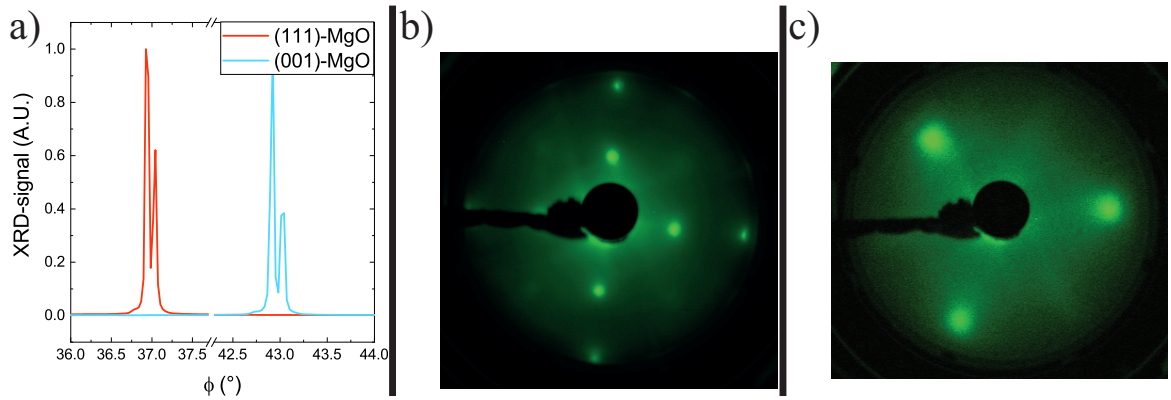

Figure E.1: Summary of the substrate characterisation. a): Principal features observed for the XRD spectrum of (001)(blue) and (111)(orange) MgO substrates. b): LEED diffraction pattern observed for the (001)-substrate [117]. c): LEED diffraction pattern observed for the (111)-substrate [117].

E.1 XRD

The XRD-measurements performed on pristine MgO substrates are shown in figure E.1a. The measured features in the spectrum for (001)-MgO and (111)-MgO are shown in blue and orange respectively. The observed peak splitting is due to the non-monochromatism of the Cu X-ray source.

E.2 LEED

The LEED measurements for MgO substrates after ion beam milling are shown in figures E.1b and c for (001)-substrates and (111)-substrates respectively. The observed symmetry of the diffraction patterns is consistent with literature [116].

Appendix F

Brief introduction to Raman spectroscopy

Raman spectroscopy is an optical non-invasive characterization method to quantify vibrational and rotational and magnon modes of a material. During Raman spectroscopy, a sample material is irradiated with a laser of well defined frequency. The photons which are scattered from the material have either the same (Rayleigh scattering), more (anti-Stokes scattering) or less (Stokes scattering) energy than the incoming photon (Figure F.1). the difference in energy for Stokes- and anti-Stokes scattering is caused by the creation or annihilation of one or more phonons or magnons in the probed material. When a phonon (magnon) is created by the incoming photon, the scattered photon will have an energy equal to $\epsilon_{\text{sc}} = \epsilon_{\text{laser}} \pm \epsilon_{\text{phonon}}$. If a phonon (magnon) is absorbed, the scattered photon will have slightly more energy. When a phonon (magnon) is created the photon will have slightly less energy. Since every material has its own specific set of vibrational and rotational modes, the Raman spectrum can be interpreted as a fingerprint of your material.

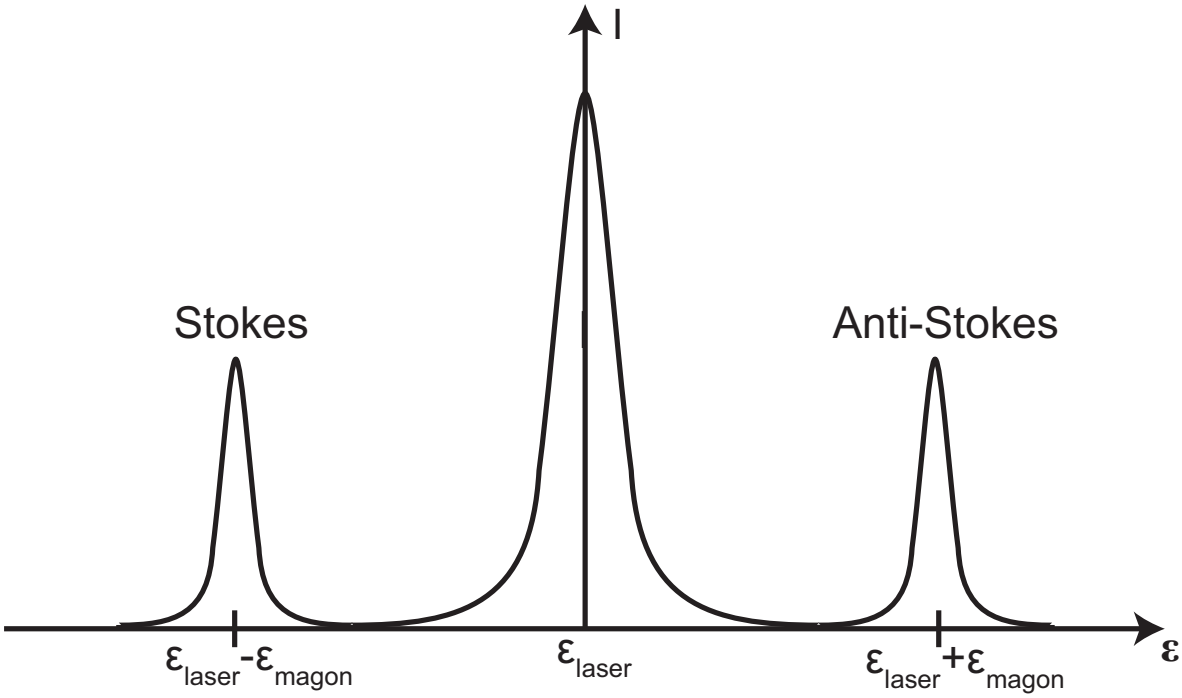

Figure F.1: Schematic of the three basic scattering processes that can be distinguished in a Raman spectroscopy experiment. In a Stokes and Anti-stokes process, one (multiple) magnon(s) or phonon(s) is (are) created or annihilated respectively. For Rayleigh scattering, the scattered photons have the same energy as the incident photons.

Appendix G

Transmission sample holder

Below the technical drawings of the transmission sample holder that was used during this work are presented in figures G.1, G.2, G.3 and G.4. The sample holder was designed in collaboration with ing. Jeroen Francke.

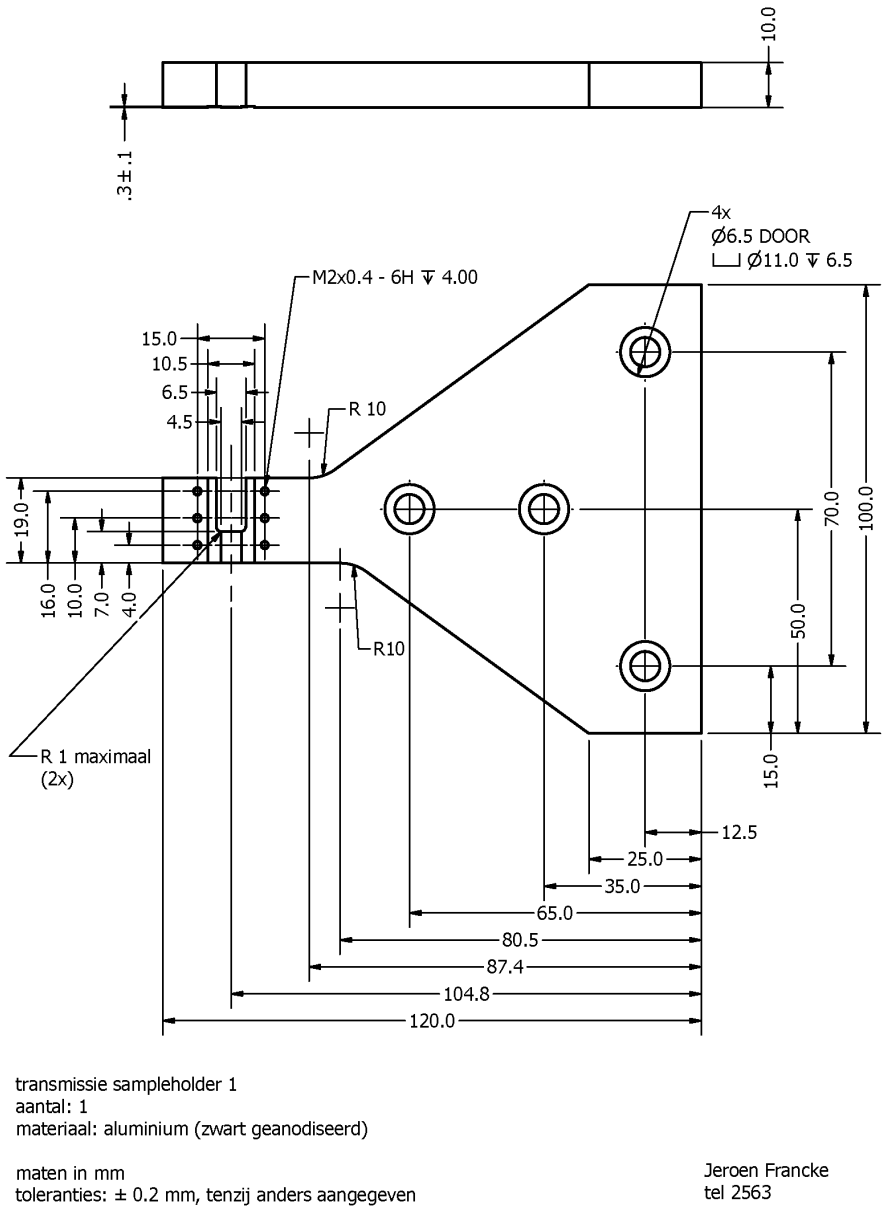

Figure G.1: Front and side view of the transmission sample holder used in the optical measurements presented in this work. Sizes shown are given in mm. Drawing courtesy of ing. Jeroen Francke.

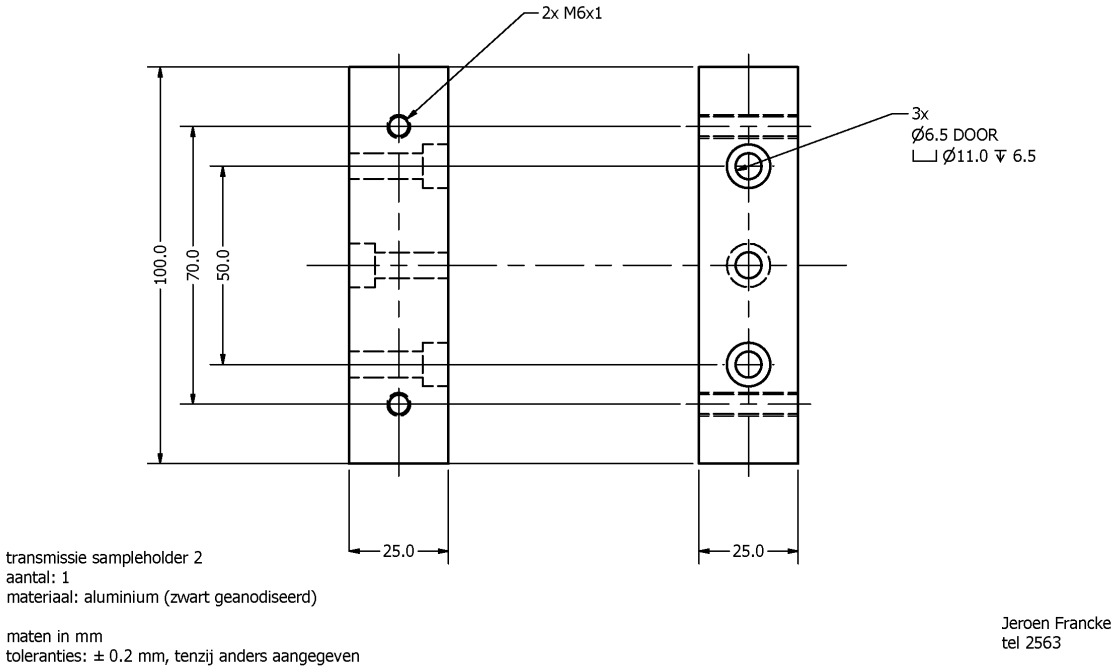

Figure G.2: Side view of the transmission sample holder used in the optical measurements presented in this work. Sizes shown are given in mm. Drawing courtesy of ing. Jeroen Francke

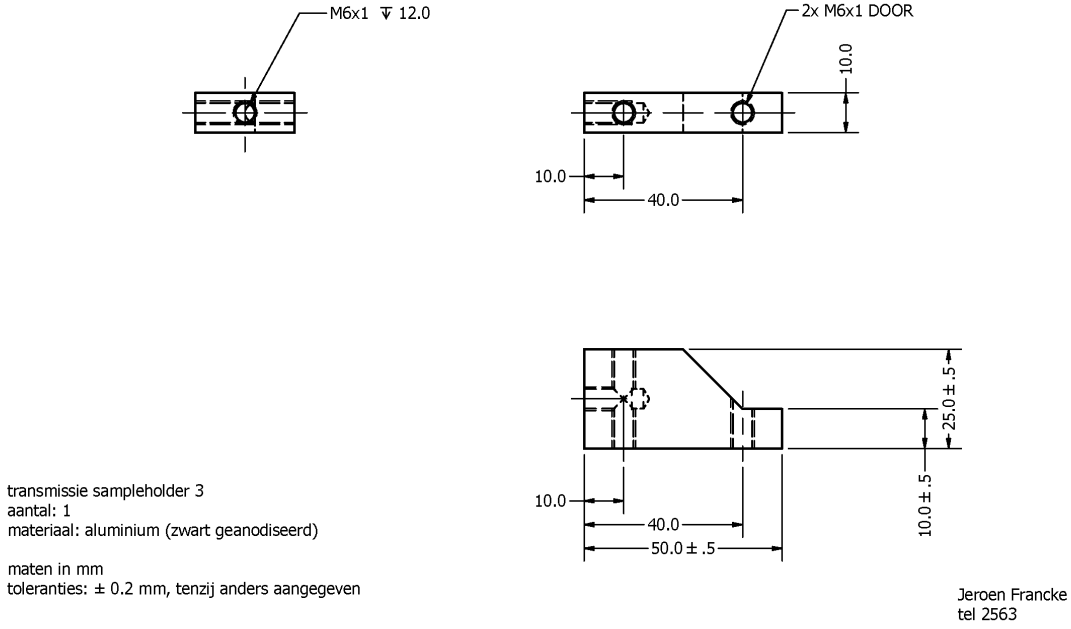

Figure G.3: Side view of the transmission sample holder used in the optical measurements presented in this work. Sizes shown are given in mm. Drawing courtesy of ing. Jeroen Francke

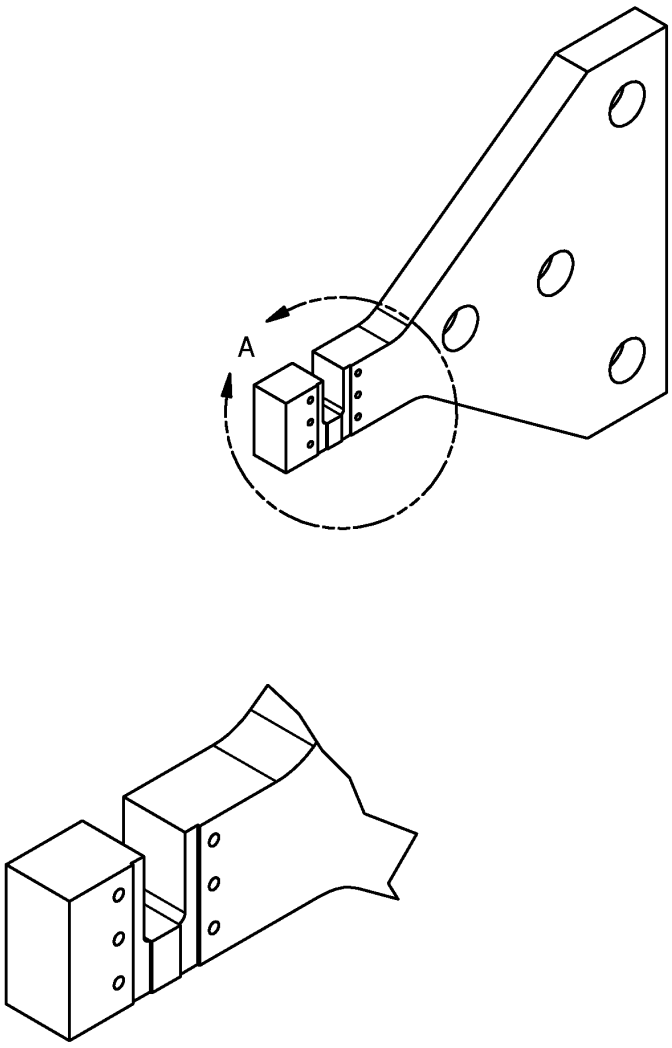

Figure G.4: Detail of the sample mounting location on the sample holder. Drawing courtesy of ing. Jeroen Francke